DIRECT MEASUREMENT OF THE ^{21}Na$(p,\gamma)^{22}$Mg RESONANT REACTION RATE IN NOVA NUCLEOSYNTHESIS

by

Shawn Bishop

B.Sc. Hon., McMaster University, 1995

M.Sc., University of Victoria, 1998

THESIS SUBMITTED IN PARTIAL FULFILLMENT

OF THE REQUIREMENTS FOR THE DEGREE OF

DOCTOR OF PHILOSOPHY

IN THE DEPARTMENT

OF

PHYSICS

© Shawn Bishop 2003

SIMON FRASER UNIVERSITY

August, 2003

APPROVAL

Name: Shawn Bishop

Degree: Doctor of Philosophy

Title of Thesis: Direct Measurement of the ^{21}Na(p,γ)^{22}Mg Resonant Reaction Rate in Nova Nucleosynthesis

Examining Committee: Dr. Jeff Sonier, Department of Physics, Simon Fraser University (Chair)

Dr. John D'Auria, Professor, Department of Chemistry

Dr. Gordon Ball, Research Scientist, TRIUMF

Dr. Lothar Buchmann, Research Scientist, TRIUMF

Dr. Howard Trottier, Professor, Department of Physics

Dr. Colin Jones, Professor, Department of Chemistry, Internal Examiner

Dr. Peter Parker, Professor, Department of Physics, Yale University, External Examiner

Date Approved: August 6, 2003

PARTIAL COPYRIGHT LICENSE

Title of Thesis/Project/Extended Essay

Direct Measurement of the

$^{21}Na(p,\gamma)^{22}Mg$ Reaction Rate in

Nova Nucleosynthesis

Author:_____
(signature)

Shawn Bishop
(name)

August 28, 2003
(date)

Abstract

An oxygen-neon nova is presently understood to be the result of a thermonuclear runaway on the surface of an oxygen-neon white dwarf. During this event production, and subsequent ejection into the interstellar medium, of the radioisotope ^{22}Na can ensue. With a half life of 2.6 years, ^{22}Na β-decays leading to the emission of a characteristic γ-ray of energy 1.28 MeV. This combination of long half life and characteristic gamma signature makes ^{22}Na a possible "viewing port" into the nuclear physics of these cataclysmic events, for, γ-rays of this energy are readily detectable with past and current orbiting satellite observatories. To date, no 1.28 MeV γ-signal has been observed from any nova, and this remains an outstanding problem in astrophysics.

Within these environments, production of ^{22}Na can proceed via isolated, narrow resonances in the reaction path: ^{20}Ne$(p,\gamma)^{21}$Na$(p,\gamma)^{22}$Mg$(\beta^+ \nu_e)^{22}$Na. As many as three resonant states in the ^{22}Mg nucleus can contribute to the total nova ^{21}Na$(p,\gamma)^{22}$Mg reaction rate. The strengths of these resonances and, therefore, the ^{21}Na$(p,\gamma)^{22}$Mg nuclear reaction rate, were hitherto unknown, creating significant uncertainty in the expected yield of ^{22}Na from an oxygen-neon nova event.

Thick target yield measurements, using a high intensity ($> 10^8$ s^{-1}) radioactive beam of ^{21}Na with the DRAGON facility at ISAC, have been performed in inverse kinematics resulting in a direct measurement and limit on two astrophysically important resonance strengths ^{21}Na$(p,\gamma)^{22}$Mg. Uncertainty in this reaction rate has been reduced by more than 10-fold for nominal peak nova temperatures ≥ 0.3 GK. A narrow resonance, thick target yield curve has been mapped out for the first time using a radioactive heavy ion beam. From this curve, a new mass excess for the ^{22}Mg nucleus has been derived of -403.5 ± 2.4 keV, rather than the literature value of -396.8 keV. The implications the results of the present work have on nova ^{22}Na production are consistent with no observed 1.28 MeV γ-signal.

To my family and closest friends, who are the brightest stars in my life. Shine on.

Acknowledgements

This results in this thesis are the culmination of the hard work, dedication, and passion of the many people who contributed to the design, construction, and commissioning of the DRAGON facility.

Two of these people deserve recognition, in particular: Dave Hutcheon and Don Hunter, who were the ones responsible for the entire optics design of the electromagnetic separator. Their efforts and design ingenuity are, bar none, what has made the DRAGON facility the success that it is. I would also like to thank Dave Hutcheon for *always* being an attentive, courteous, and supportive audience to my ideas and work. Dave, you are the consummate professional.

Dave Ottowell, our group's gas target expert, I thank you for your unending work on keeping the gas target leak-free and operational, and for specifically taking the time to teach the rest of us how it works!

Joel Rogers and Ahmed Hussien, in addition to your work putting together the gamma-array and DSSSD, respectively, I would also like to thank each of you for lending me your ears as sounding boards during our lunches. It helped!

And thanks to the rest of the "local" DRAGON'eers: Alan, Sabine, Chris, Mike, Cyble, Alison, Wenjie, Art, Lothar, and Mohan, who were all willing to work shifts during this experiment providing me with these data, and who all provided enjoyable and interesting discussion. Thanks also to Dario for the gamma-array GEANT efficiency calculations!

Thanks also to the members of my thesis committee who provided helpful and constructive advice and suggestions for revisions. Peter Parker, thank you for your advice in this regard and for your diligence in going through the manuscript.

ISAC operations personnel deserve a hearty thanks for their untiring work in providing the excellent quality ^{21}Na beam for this experiment, and for their willingness to share their

popcorn on those graveyard shifts. Accelerator physicists Bob Laxdall and Matteo Pasini, whose skills each saved days of otherwise lost beam time: THANK YOU.

And now, saving the best to last, thanks to my supervisor, Professor John D'Auria, whose tolerance to our differences; patience with my (oft times controversial) personal views and opinions; and boundless ability to defend and support me and my work, in spite of these, gave me the means to see this work to fruition and completion. Even now, as I prepare to pursue physics elsewhere, your support and encouragement continues unabated. You had a vision to steer the science priorities of TRIUMF on a course to a world class experimental nuclear astrophysics research facility, and I am fortunate to have had the opportunity to be on board the ship as she sailed with the winds at our backs and you at the helm. John, thank you.

Contents

List of Tables

List of Figures

Chapter 1

Introduction

The study and observation of our Universe is, ultimately, a study of origins. Human cultures and religions around the world have always been imbued with a desire to understand that most fundamental of all questions about origins: "from whence did we come?" Mythologies and religions of societies from the distant past all share a common theme in answering this question of origins: that the answer is "out there" with the gods in the realm of the stars. It seems only natural, then, that throughout human history we have always looked to the skies above for inspiration and as a source of clues in our efforts to answer this profound question. The results of our sky watching have led to our present understanding of much of the workings of our Universe: from Kepler's laws of planetary motion, Newton's universal law of gravity and the Calculus, Einstein's General Relativity, to the existence of the chemical elements, the afterglow of the Big Bang and, most recently, indirect observations of dark matter and the effects of dark energy. Our understanding of these phenomena has arose from observations of stars and galaxies. Today, we know that in the first seconds of the Big Bang were forged the five lightest stable nuclei: protons, deuterium, alpha particles, ^{3}He and ^{6}Li. From the cataclysmic death throes of stars we have also learned that the Universe has been seeded with the majority of the remaining nuclei in nature that ultimately make life possible and provide us with our rich and diverse terrestrial chemistry. All of this rich knowledge from observation of the stars. In a similar spirit, this thesis is a report on the measurement of a particular nuclear reaction rate, chosen from many others on the basis of modern "sky watching" studies of oxygen-neon nova events.

1.1 Big Bang Nucleosynthesis

In 1929, astronomer Edwin Hubble obtained the first set of conclusive experimental evidence [2] that our Universe is expanding. He discovered that the recessional velocities, $\mathbf{v}$, of galaxies are proportional to their distance, $\mathbf{r}$, from Earth; namely,

$$\mathbf{v} = H_0 \mathbf{r} \,, \tag{1.1}$$

with H_0 the Hubble Constant, typically in units[1] of km s^{-1} Mpc^{-1}, and has dimensions of time^{-1}. Three immediate consequences arise from this fundamental discovery:

1. The Universe is not static (steady state).

2. There is no privileged reference point of observation in the Universe.

3. The Universe is of finite age.

From point 3 a simple estimate[2] for the age of the Universe can be made using a backward extrapolation of Hubble's Law, assuming that the recession velocity in equation 1.1 has been constant. Presently, the value of H_0 is 72 ± 8 km s^{-1} Mpc^{-1} [3]. Thus, from equation 1.1, the time estimate, t_o, of the present epoch is $t_0 = H_0^{-1} \approx 13$ billion years. Today, astronomers are reaching back in time and into the furthest depths of the Universe in an attempt to discern more accurately its age. Observations of distant stellar explosions; type Ia supernovae (SN Ia), have opened a new "looking window" into our evolutionary Universe's past. Calibration of the light curves of these events reveals their peak luminosities to be very homogeneous across a large set of observations [4, 5]. As a result, type Ia supernovae are now used as "standard candles" – cosmological distance beacons – from which the Hubble flow can be directly measured and a value on the age of the Universe determined [6]. The analysis of the SN Ia data have also shown that our Universe is dominated by an all-permeating "dark energy" field, the exact nature of which is still not understood, with the matter energy content of the Universe weighing in at only 30% [3] of the total energy content, with the rest in the form of mysterious dark energy. That the Universe is

---

[1] 1 pc $= 3 \times 10^{18}$ cm.

[2] The estimate will be an overestimate of the age, as expansion velocities were higher in the younger Universe.

dark energy dominated has been shown by the SN Ia data with a probability of more than 99% [7]. The enigma of dark energy doesn't end with these. Ongoing studies with the new Wilkinson Microwave Anisotropy Probe (WMAP) [8, 9], observing the fine structure intensity fluctuations of the cosmic microwave background radiation, have determined that the baryonic matter of the Universe only accounts for $\sim 17\%$ of all matter, with the rest being comprised of a mysterious dark matter [10]. This dark matter is presently being indirectly mapped [11] using weak gravitational lensing techniques coming into fruition at this very moment. Presently, observations of the cataclysmic SN Ia events, combined with the data arriving from WMAP, reveal the age of the Universe to be 13.6 ± 1.5 billion years [3].

As we extrapolate back in time to the first few instants after the creation of the primordial fireball of the Big Bang, we are able to gain insight into the origins of the basic building blocks of visible baryonic matter. In those first instants the temperature was of such an extreme that no nuclei could exist; the temperature of the Big Bang "fireball" being far in excess of nuclear binding energies. As the "fireball" expanded it cooled. With this cooling, the initial quark-gluon plasma condensed into hadrons and mesons. These particles rapidly annihilated with their anti-particle counterparts, contributing to the photon bath already present at the onset of the fireball. At approximately 10^{-2} s into the fireball, with a temperature of $T \approx 10^{11}$ K, protons and neutrons were kept in equilibrium with each other via the following weak interaction reactions:

$$p + e^- \;\rightleftharpoons\; n + \nu_e \,, \tag{1.2}$$

$$n + e^+ \;\rightleftharpoons\; p + \overline{\nu}_e \,, \tag{1.3}$$

$$n \;\rightleftharpoons\; p + e^- + \overline{\nu}_e \,. \tag{1.4}$$
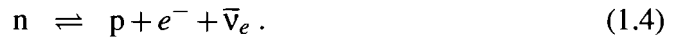
The last reaction is by far the slowest of the three and can almost be neglected, as the neutron half-life is ≈ 10 minutes and the right hand side requires a simultaneous collision of three particles. Continued expansion of the space caused these reactions to fall out of equilibrium as the characteristic time-scale for a reaction became comparable with the dynamical expansion time of the Universe. This occurred at a temperature, $kT \approx 0.8$ MeV [12] $(T \approx 10^{10}$ K), the so-called "freeze out temperature". The abundance ratio of neutrons to protons at this epoch can be determined by the Saha equation as,

$$\frac{[n]}{[p]} \approx \exp(-\Delta m c^2 / kT) \,, \tag{1.5}$$

with $\Delta mc^2 = 1.29$ MeV, the mass difference between the neutron and proton; the result being, $[n]/[p] \approx 1/5$. The neutron abundance, expressed as a fraction of the total amount of nucleonic matter is just,

$$\frac{[n]}{[n] + [p]} \approx \frac{1}{6}. \tag{1.6}$$

Approximately one minute later, at a temperature $T \approx 1 \times 10^9$ K, the photon energy density was low enough to allow combination of protons and neutrons to form deuterons which then fused to primarily produce ^{4}He [13]. Neglecting the decay of the neutrons in this short period of time, equation 1.6 indicates that the combination of neutrons at an abundance ratio of 1/6 with an equal number of protons will produce a helium abundance of $[^4$He$] \approx$ 1/3 which, given these crude approximations, is in decent agreement with the observed abundance of 24% [13].

Big Bang nucleosynthesis (BBN) models employing nuclear reaction networks with well-known nuclear cross sections, and which take into account the energy distributions of the reacting particles, have been performed [14, 15] and clearly indicate that the dominant nuclide (beyond hydrogen) in the early Universe should be ^{4}He, followed by deuterium, ^{3}He and tiny amounts of ^{7}Li. A result of such a network calculation is shown in figure 1.1 [14] and shows that, at the 95% confidence level, the measured abundance of ^{4}He agrees with the Big Bang deduced baryon density; the case of ^{7}Li is only in marginal disagreement and may be explained by stellar mixing processes. Elements heavier than ^{7}Li are precluded from forming in BBN due to mass gaps at atomic mass numbers, $A = 5$ and $A = 8$; no stable nuclides exist for these mass numbers.

Big Bang nucleosynthesis explains the origins of the visible baryonic matter in our Universe exceptionally well. It also makes the very strong case that elements beyond lithium cannot be produced. That there are elements beyond lithium demands that there must be other mechanisms by which the intermediate-mass and heavy elements can be produced. These mechanisms are stellar and explosive nucleosynthesis.

The predictive success of BBN is, in no small part, due to the almost fully complete experimental knowledge of relevant nuclear cross sections [14] at the energies involved in the early hot Universe. On the other hand, for explosive nucleosynthesis – the means by which the interstellar medium is seeded with the life-giving elements – the experimental situation for the relevant nuclear cross sections is, in some cases, one of uncertainties that can range
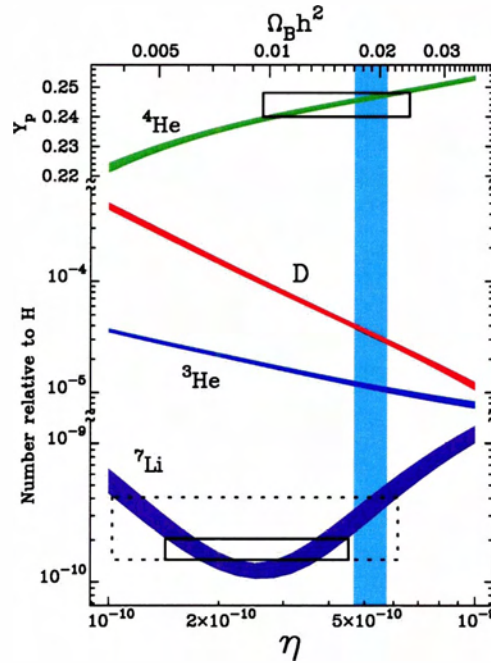
Figure 1.1: Big Bang nucleosynthesis abundance predictions, from the nuclear reaction network of Nollett et al. [14] as a function of the baryon-to-photon number ratio, η. All bands and solid boxes are 95% confidence intervals. The vertical band is the deuterium-inferred baryon density of our Universe.

from factors of 5-1000 [16]. Thus, to understand the origins of the chemical elements beyond those of BBN requires experimental knowledge of the cross sections for those nuclear reactions that occur within astrophysical sites of quiescent and explosive nuclear burning. We turn our attention to these sites in the next two sections.

1.2   Quiescent Hydrogen Burning

As implied by the results of BBN, the stars we observe are composed almost entirely of hydrogen gas. Prior to circa 1900, the power source of stars was still a mystery. Early attempts to calculate the energy rate of the Sun on the basis of gravitational potential energy release quickly demonstrated that the Sun could only be many millions of years old [17], a

result in complete contradiction with the geological data on the age of the Earth at that time: the Sun would have been younger than the Earth! The mystery remained until the advent of quantum mechanics. Then, in 1938, Bethe and Critchfield [18] carried out the first direct quantum mechanical calculation of the fusion reaction rate between two protons to form deuterium and demonstrated that this reaction could produce sufficient energy of *"the right order of magnitude"* [18] to account for the observed energy generation rate of the Sun. The mystery, for the most part, had been solved. The remaining "order of magnitude" of power generation is now known to primarily come about by way of nuclear reactions following on the proton-proton fusion reaction, and form the basis of the proton-proton chains. In total, there are three proton-proton chains. The first of these is the proton-proton I (PPI) chain, comprised of the following reactions:

$$p + p \quad \rightarrow \quad d + \beta^{+} + v_e \tag{1.7}$$

$$d + p \quad \rightarrow \quad {}^{3}\mathrm{He} + \gamma \tag{1.8}$$

$${}^{3}\mathrm{He} + {}^{3}\mathrm{He} \quad \rightarrow \quad {}^{4}\mathrm{He} + 2p\,. \tag{1.9}$$
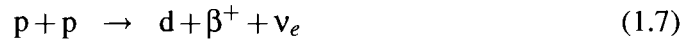
Reaction 1.7, a weak interaction process, is the slowest and can be regarded as the spontaneous weak decay of a proton in the field of a second proton, with the nuclear interaction between them providing the binding energy to make the decay energetically possible. This chain accounts for 86% of the power generation of the Sun [19].

Secondary to the PPI chain, accounting for essentially the remaining 14% of solar power generation, is the PPII chain comprised of reactions 1.7 and 1.8 followed by [19]:

$${}^{3}\mathrm{He} + \alpha \quad \rightarrow \quad {}^{7}\mathrm{Be} + \gamma \tag{1.10}$$

$${}^{7}\mathrm{Be} + \beta^{-} \quad \rightarrow \quad v_e + {}^{7}\mathrm{Li} \tag{1.11}$$

$${}^{7}\mathrm{Li} + p \quad \rightarrow \quad 2\,{}^{4}\mathrm{He}\,. \tag{1.12}$$

Lastly, occurring only 0.02% of the time, we have the PPIII chain, comprised of reactions 1.7, 1.8 and 1.10, followed by:

$${}^{7}\mathrm{Be} + p \quad \rightarrow \quad {}^{8}\mathrm{B} + \gamma \tag{1.13}$$

$${}^{8}\mathrm{B} \rightarrow {}^{8}\mathrm{Be}^{*} + e^{+} + v_e \quad \rightarrow \quad 2\,{}^{4}\mathrm{He} + e^{+} + v_e\,. \tag{1.14}$$
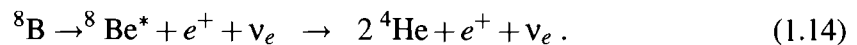
The PPII and PPIII chains only occur at the highest temperatures in the stellar core, owing to their inherently larger Coulomb barriers.

All 3 chains release a total of 26.73 MeV in nuclear binding energy [19]. However, some of this energy is *entirely* lost to the star, carried away by the neutrinos, resulting in a mean energy loss of 2%, 4% and 28% of the binding energy for the PPI, PPII, and PPIII chains, respectively [19]. The net result of all 3 chains is to convert four protons into an alpha particle, two positrons and two electron neutrinos:

$$4\,\mathrm{p} \quad \rightarrow \quad {}^{4}\mathrm{He} + 2\,e^{+} + 2\,\nu_{e}. \tag{1.15}$$

In this way, a star converts its internal supply of hydrogen fuel into helium, generating internal thermal energy sufficiently high enough to create a pressure gradient within the star that balances the local gravitational weight and maintains the star's hydrostatic equilibrium.

As more hydrogen fuel is exhausted and converted into helium, the reaction rate of the PP-chains must decrease as the number density of reacting protons declines. At the same time, the temperature of the core will not be sufficiently high enough for alpha particle burning to take place at a rate fast enough to overcome the mass stability gap at $A = 8$. The emission of photons from the star's interior, having taken as much as 1 million years to reach the stellar surface [17], serves to cool the star as the PP-chain rates slow down. As a result, pressure in the stellar core will slowly decrease resulting in a slow contraction of the core. This contraction results in a heating of the core as gravitational potential energy is converted into thermal energy, as demanded by the virial theorem. As the core collapses the outer layers of the star, still composed of hydrogen, form a relatively then outer shell around the core [19, 20]. This hydrogen shell will undergo hydrogen burning with the resulting helium formed contributing to the mass of the contracting core. Continued contraction of the stellar core results in an increase in its luminosity, but a high opacity in the outer shell prevents efficient transfer of the photons to space and the shell subsequently expands [20]. This expansion can be as large as 50 times the shell's original radius [19]. Subsequent cooling of this shell, due to its expansion, results in a shift of its radiation to longer wavelengths causing its colour to appear red. At this stage, the star has evolved into a Red Giant. Continued contraction of the compact core results in the ignition of helium burning.

1.3 Quiescent Helium Burning

There are no stable nuclei at $A = 5$. This, therefore, precludes proton burning on helium during the build-up of helium in the proton-proton burning stage of a star's life. The only way to burn helium, therefore, is by the fusion of two helium particles to form ^{8}Be. However, ^{8}Be is unbound by 92 keV, promptly decaying back to two alpha particles with a lifetime of just 1×10^{-16} s. Nevertheless, it turns out that this lifetime is sufficiently long to allow an equilibrium abundance of ^{8}Be to form in the stellar core. As an example, for a temperature of $T_6 = 100$ and a density of 10^5 g cm^{-3} an abundance fraction ^{8}Be/^{4}He $= 5.2 \times 10^{-10}$ is able to form: or about one ^{8}Be nucleus for every billion ^{4}He nuclei [19]. This abundance is sufficient to allow subsequent alpha particle capture on ^{8}Be to form ^{12}C by way of an s-wave resonance through a state in ^{12}C located at an excitation energy of 7.68 MeV [19].

As the concentration ^{12}C increases within the stellar core, alpha particle capture on ^{12}C can take place to form ^{16}O. This reaction is probably one of the most important, and also one of the most poorly known, for stellar evolution; it ultimately determines the abundances of ^{12}C and ^{16}O for stars. The reaction is poorly known because it occurs via interfering resonances, some of which are sub-threshold, for which the physical parameters such as widths, are poorly known and difficult to measure, with variations on the reaction rate by factors as large as ~ 10 [20]. Be that is it may, what we do know is that the helium burning process concludes with a stellar core composed of carbon and oxygen. Helium burning on oxygen does not proceed due to a combination of a high Coulomb barrier and a lack of rate-enhancing resonances in ^{20}Ne within the energy range typical of the core temperatures of these stars [19].

As the helium burning phase of the star concludes, core contraction must again ensue as the temperature of the interior decreases from an increasingly lower rate of nuclear reactions. At this stage in the star's life several paths for its ultimate fate are open to it depending on what the mass of the core is at termination of helium burning. One such fate is an Oxygen-Neon white dwarf, to be discussed in the next section.

1.4 Oxygen-Neon Novae & Explosive Nucleosynthesis

Stars that begin their lives with an initial mass in the range of $\approx$ 8-10 $M_\odot$ can retain cores of sufficient mass to proceed into quiescent heavy-ion burning once their helium fuel source has been exhausted. At the conclusion of the helium burning stage of a star's evolution, the core's composition will mainly be carbon and oxygen. With ^{12}C and ^{16}O the primary ingredients for nuclear reactions, and interior temperatures in the range of $T_8 \approx 7$, one expects that carbon-carbon burning will be the first reaction process to proceed due to its lower Coulomb barrier. The primary carbon burning reactions are [20],

$$^{12}\text{C} + ^{12}\text{C} \rightarrow ^{20}\text{Ne} + \alpha, \tag{1.16}$$

$$^{12}\text{C} + ^{12}\text{C} \rightarrow ^{23}\text{Na} + p, \tag{1.17}$$

which occur with almost equal probability [21]. The protons and alpha particles liberated from these two reactions are then able to go on to induce additional reactions on the existing heavy ions in the stellar mix. Reaction network calculations done by Reeves and Salpeter [22] reveal that reactions such as $^{12}\text{C}(\alpha,\gamma)^{16}\text{O}$, $^{16}\text{O}(\alpha,\gamma)^{20}\text{Ne}$, $^{23}\text{Na}(p,\alpha)^{20}\text{Ne}$, $^{23}\text{Na}(p,\gamma)^{24}\text{Mg}$, and $^{20}\text{Na}(\alpha,\gamma)^{24}\text{Mg}$, in conjunction with the ongoing carbon-carbon burning, are additional reaction paths by which the elemental composition of the star is depleted of carbon and converted primarily into oxygen, neon and magnesium. The stellar core, having exhausted its supply of carbon and without a fuel source to create core temperatures high enough to maintain its hydrostatic equilibrium with gravity, will undergo a contraction. Should it happen that the total mass of the stellar core at the conclusion of the carbon burning stage is $\sim$ 1.1-1.4 $M_\odot$, there will be insufficient internal pressure in the core to generate sufficiently high temperatures ($T_9 \approx 1$) to ignite oxygen burning. At this stage the star will have no recourse but to continue with its collapse. As the core volume decreases and internal pressures increase, the particle energies within the core will increase. Subsequently, the number of quantum energy states available to the electrons in the stellar interior will begin to fill up, causing the electron gas to become degenerate. Collapse will continue until such time that the electron gas becomes completely degenerate, or nearly so, at which point hydrostatic equilibrium will once again be achieved. With all nuclear reactions having ceased and supported by a degenerate electron gas, the star will become an oxygen-neon white dwarf (ONe WD); a "cinder" of its nuclear burning era. With nuclear reactions hav-
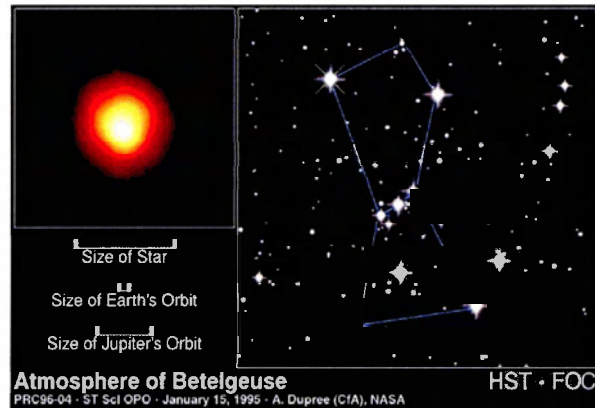
Figure 1.2: Hubble Space Telescope photo [1] of the Red Giant Betelgeuse of the Orion constellation. Note the size of the stellar diameter.

ing ceased in this remnant, one might be inclined to wonder why such objects would be of interest to the nuclear astrophysics community.

No less than half of all observed star systems are multiple systems, wherein two or more stars are in orbit together about a common centre of mass [17]. A star's lifetime, to first order, is $\propto M^{-3}$: the higher its mass, the much shorter its life. With this it can be seen that if two stars of disparate masses, for example 10 $M_\odot$ and 1 $M_\odot$, come to orbit about each other the massive star of the pair will proceed through its life cycle faster than its lighter companion by a factor of ~ 1000. As the massive star dies and becomes a white dwarf, its lighter companion will still be in the midst of its life cycle; being on the main sequence of hydrogen burning. As the light companion exhausts its hydrogen and enters into its helium burning phase, it will enter into the Red Giant stage of its life. A star in this stage of its life swells to immense size, as evidenced in figure 1.2 [1]. The structure of this Giant is one of a dense, compact core with a hydrogen burning shell, surrounded by a distended spherical shell rich in hydrogen and helium. As this shell expands, material from it can "spill over" the inner Lagrangian point of its Roche Lobe (the surface of gravitational equipotential of the two stars) into the gravitational well of the white dwarf (WD), forming an accretion disk around the WD. Viscous dissipation processes within the accretion disk will cause this material to continually lose its kinetic energy in the form of radiation, thus causing the material to gradually spiral down onto the surface of the WD forming a hot envelope of
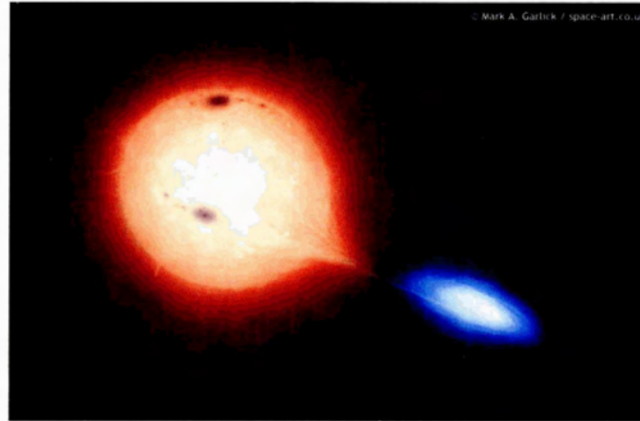
Figure 1.3: Artist's impression [23] of a white dwarf binary star system showing the material flow from the Red Giant companion through the Roche Lobe, and resulting accretion disk around the white dwarf.

hydrogen-rich material around the WD. Figure 1.3 [23] illustrates these concepts.

As the mass of the envelope increases, its lower layers will become electron degenerate as the WD surface gravity compresses those layers to densities on the order of 5×10^3 g cm^{-3}. The degenerate electron gas, with its high thermal conductivity, is able to efficiently conduct heat to all points in the envelope across the white dwarf's surface. As the temperature of the base layers increase, quiescent proton-proton burning takes place with its release of nuclear binding energy, causing the temperature at the base to steadily increase allowing proton capture on the seed neon in the WD surface. The release of nuclear binding energies from these proton capture reactions causes the shell's temperature to rapidly increase; the shell itself, however, does not expand with the increasing temperature as it is in a state of degeneracy. Convective cells at the base of the envelope can dredge up additional quantities of seed neon into the hydrogen layer for further nuclear processing by way of proton capture [24] and this could be a mechanism for enrichment of those elements that result from the subsequent β-decay chain of these reactions [24]. These conditions culminate in a thermonuclear runaway (TNR) across the surface of the WD. The intense prompt gamma flux, caused by the runaway, is able to lift the degeneracy of the material when it exceeds the Eddington radiation pressure limit. An explosive outburst ensues, ejecting a shell

of isotopically enriched material, $\sim 2 \times 10^{-4}$ $M_\odot$ into the interstellar medium (ISM). With an underlying WD comprised of oxygen and neon, it is expected that a significant amount of the radioactive nuclide ^{22}Na will be produced in the TNR. This nuclide has a half-life of 2.6 years, beta decaying to the first excited state of ^{22}Ne which promptly γ-decays to its ground state, emitting a 1.28 MeV γ-ray. In principle, this γ-ray can be detected with orbiting γ-ray observatories and is, therefore, a direct observable for furthering our theoretical understanding of these events and their contributions to galactic nucleosynthesis.

1.4.1 The Ne-Na Burning Cycle

Observational data from novae events reveal that approximately 25% − 33% of novae are of the ONe type [25]. These events are characterized by a high neon abundance enrichment far in excess of the solar abundance value; with enrichment values in the range: [Ne/Ne$_\odot$] = 20–296 [25–27]. Correlated to this is the finding that these novae do not contain significant amounts of carbon dust [25], indicating the WD is carbon deficient. Rich in neon and poor in carbon is just what is to be expected from the carbon-carbon burning cycle as discussed in § 1.4. Taken together, these two observations give strong weight to the hypothesis that the underlying WD is of the ONe type.

At the onset of accretion, radiative proton capture on the seed ^{20}Ne in the WD leads to the production of ^{22}Na by the cold neon-sodium (NeNa) cycle [28] via the reaction sequence:

$$^{20}\text{Ne}(p,\gamma)^{21}\text{Na}(\beta^+\nu_e)^{21}\text{Ne}(p,\gamma)^{22}\text{Na}\,. \qquad (1.18)$$
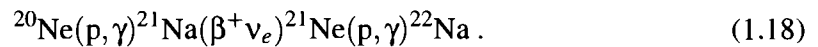
This sequence is shown in figure 1.4 with the blue arrows. With the exception of the ^{20}Ne$(p,\gamma)^{21}$Na reaction, all reactions discussed within the NeNa cycles are dominated by radiative proton capture through narrow, isolated, resonances. As the temperature of the envelope burning zone increases into the range $0.7 \leq T_8 \leq 1$, a quasi-equilibrium of ^{22}Na abundance is established as its destruction rate from proton capture to ^{23}Mg becomes competitive with its production rate from proton capture on ^{21}Ne and due to its convective transport to the cooler outer layers of the envelope [29].

At a temperature somewhere between $1 \leq T_8 \leq 2$, models predict that ^{22}Na destruction from proton capture will dominate its production from ^{21}Ne(p,γ), driving the ^{22}Na abundance downwards. However, in this high temperature regime, the production rate of ^{21}Na
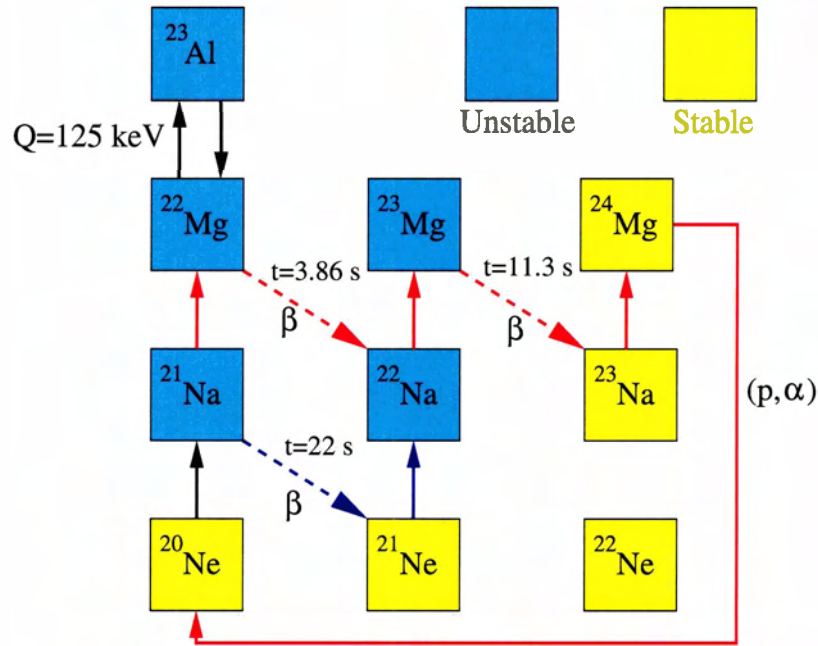
Figure 1.4: The NeNa burning cycles. For low temperatures, where proton capture on ^{21}Na is slow, the cold NeNa cycle, denoted by blue arrows, dominates production of ^{22}Na. As the temperature approaches the peak of the TNR the proton capture rate on ^{21}Na becomes faster than the ^{21}Na decay rate, thus opening up the hot NeNa cycle, denoted by red arrows.

increases from enhanced proton capture on the seed ^{20}Ne leading to increased abundance of ^{22}Mg; thus opening up the "hot" NeNa cycle, which is shown in figure 1.4 by the red arrows. Once ^{22}Mg is produced, two reaction paths are available to it: proton capture to ^{23}Al or β-decay to ^{22}Na. The Q value for photodisintegration of ^{23}Al is just 125 keV. The nova environment is a bath of high energy photons from nuclear transitions and a plethora of 511 keV photons from the annihilation of positrons arising from β-decays of those proton-rich nuclides that decay on a time scale faster than their respective proton capture rates. The survivability of ^{23}Al to photodisintegration under these conditions, beyond a tiny equilibrium abundance, is very small. Moreover, it has been found that the combined non-resonant and resonant reaction rate of proton capture on ^{22}Mg under nova conditions is slower than its corresponding β-decay rate [30]. We can conclude, therefore, that ^{22}Mg beta decays to ^{22}Na with unit efficiency, keeping nuclide material within the cycle and enhancing the ^{22}Na

abundance at this stage of the runaway.

How much ^{22}Na is produced in a nova event is a complicated question. The time scale for the TNR is ~ 200 s [29, 31], and convection time scales are comparable to this. As a result, nuclides produced early on in the burning that are convectively carried to the cooler surface layers can survive against destruction from proton capture. From this we can expect that any ^{22}Na carried to the surface in this way will survive the outburst. On the other hand, if the proton capture rates on a particular nuclide in the burning layers are fast compared to the convective time scale, then we can expect that not much of that particular nuclide will reach the cooler layers before a significant fraction of it is destroyed by proton capture.

Production of ^{22}Mg comes in the latter stages of the TNR. However, its half-life is only 3.86 s. Thus, if the rate for ^{21}Na$(p,\gamma)^{22}$Mg is high, ^{22}Mg will be produced sooner during the onset of the peak of the TNR. This in turn will give the ^{22}Mg a chance to beta decay to ^{22}Na right in the midst of the peak temperatures of the TNR, leading to significant destruction of ^{22}Na by way of proton capture.

Clearly, the stages in the TNR where the rate of the ^{21}Na$(p,\gamma)^{22}$Mg reaction surpasses the ^{21}Na β-decay rate, and how fast the ^{21}Na$(p,\gamma)^{22}$Mg rate becomes at the peak temperatures of the TNR, will play a critical role in how much ^{22}Na will be produced in a ONe nova. Studies of the impact this rate has on ^{22}Na production in nova models show that reducing the presently adopted rate by a factor of 100 results in a factor of ~ 3 increase in ^{22}Na abundance in the model nova ejecta [29]. Additionally, comparative nucleosynthesis studies [32] in nova models using only temperature-density profile information in the envelope burning zone, i.e., not including full hydrodynamics, reveal that changes of 100 in the ^{21}Na$(p,\gamma)^{22}$Mg rate indicate relative ^{22}Na abundance changes by as little as zero to as much as six, depending on the mass and composition of the underlying ONe white dwarf and accretion layer, and the burning temperatures involved. In particular, it was found that the highest temperature models yielded the six-fold relative change in ^{22}Na abundance [32]. Presently, five ONe candidates (Nova Her 1991, Nova Sgr 1991, Nova Sct 1991, Nova Pup 1991, Nova Cyg 1992) have been studied using the COMPTEL γ-ray observatory in an effort to detect the 1.28 MeV γ-line. The most recent nova studied was Nova Cygni 1992, shown in figure 1.5 [1]. In *all* cases there was no detection of this line [33] and only upper limits on the 1.28 MeV photon flux could be made. Improving our knowledge of the rate of the ^{21}Na$(p,\gamma)^{22}$Mg reaction and, hence, its effect on ^{22}Na production, could help the

Figure 1.5: Hubble Space Telescope photo [1] of Nova Cygni 1992. The expanding shell of isotopically enriched material is $\approx$ 400 times the diameter of the Solar System. No 1.28 MeV γ-line was observed.

astrophysics community understand why this line has not yet been observed and glean new knowledge on the physics of novae outbursts so as to indicate under what circumstances it can be expected to be observed.

Other evidence we have that indicates ONe novae should produce ^{22}Na is in the form of isotopic abundance anomalies discovered in meteorites. In particular, low isotopic ratios of ^{20}Ne/^{22}Ne have been found in some meteoritic SiC grains [19] with values ≤ 0.15, as compared to the terrestrial value of ≈ 10. One possibility for explaining these ^{22}Ne enrichments is to consider that the grains formed from the dust of an ONe nova ejecta containing ^{22}Na. Once trapped in the matrix of the SiC, the ^{22}Na decays *in situ* to ^{22}Ne, thereby enriching the ^{22}Ne content of the grain. Such a scenario, if correct, must place constraints on the amount of ^{22}Na produced in an ONe nova and the physical evolution of its ejecta post-outburst, thus providing valuable information for constraining nova models. Recently, five SiC grains have been found that possess abundance ratios of ^{12}C/^{13}C, ^{14}N/^{15}N, ^{30}Si/^{28}Si, and ^{26}Al/^{27}Al in good agreement with some of the current ONe nova models [34] and suggest an unambiguous origin from an ONe nova outburst. Improving our present state of knowledge of the resonant ^{21}Na$(p,\gamma)^{22}$Mg reaction rate for ONe nova could help the astrophysics community better understand the anomalous neon isotopic ratio in these grains of

stardust and the environment that created them. To these ends, this thesis reports on the first ever direct measurement of the ^{21}Na(p,γ)^{22}Mg resonant reaction rate at energies typical of ONe novae.

1.5   Thesis Outline

Chapter 2 will present the thermonuclear reaction formalism necessary for calculating proton fusion reaction rates in these events. Critical to the reaction rate is the quantity called the resonance strength, denoted by $\omega\gamma$. It is this quantity that we measure directly in the lab and the theory relating how experiment obtains this quantity for application to the thermonuclear reaction rate is presented.

Of course, no nuclear physics experiment can be done without a facility and an apparatus. Chapter 3 will introduce the reader to the ISAC radioactive ion beam facility at TRIUMF along with the DRAGON (Detector of Recoils And Gammas Of Nuclear reactions) recoil mass separator and its associated detector and data acquisition systems, without which, these measurements would not have been possible.

Chapter 4 presents the reader with the details of the data collection and analysis, from which the astrophysical results will be derived. The first ever thick target yield curve, mapped with a radioactive beam is presented from which the new resonant ^{21}Na(p,γ)^{22}Mg reaction rate is derived. A comparative discussion of the new result with previously estimated rates is given. Additionally, the surprisingly unexpected result of a new ^{22}Mg mass excess is obtained as a result of having mapped the thick target yield curve.

Finally, Chapter 5 has a discussion of the implications of the results of this work, along with recent experimental attempts to corroborate them by other groups.

Chapter 2

Theory

The power source for novae explosions is the thermonuclear engine. How much energy is liberated, what elements are synthesized and what abundances will they have are all issues sensitive to nuclear physics considerations. The proton capture reactions at temperatures found in novae are all sub-Coulomb barrier reactions. This chapter presents the stellar nuclear reaction rate theory and describes how we determine stellar nuclear reaction rates from the yields of nuclear reaction measurements carried out in the laboratory.

2.1 Kinematics

For two non-relativistic particles of masses m_1 and m_2, with respective velocities $\mathbf{v}_1$ and $\mathbf{v}_2$, the centre of mass (cm) velocity, $\mathbf{V}$, is defined as,

$$\mathbf{V} = \frac{m_1\mathbf{v}_1 + m_2\mathbf{v}_2}{m_1 + m_2} . \tag{2.1}$$

The velocity of particle 1 with respect to the cm velocity is just,

$$\mathbf{v}_1 - \mathbf{V} = \frac{m_2}{m_1 + m_2}(\mathbf{v}_1 - \mathbf{v}_2) = \frac{m_2}{m_1 + m_2}\mathbf{v} , \tag{2.2}$$

where $\mathbf{v} \equiv \mathbf{v}_1 - \mathbf{v}_2$ is the relative velocity of particle 1 with respect to particle 2. Similarly, for the relative velocity of particle 2 with respect to the cm, we have,

$$\mathbf{v}_2 - \mathbf{V} = -\frac{m_1}{m_1 + m_2}\mathbf{v} . \tag{2.3}$$

The total initial kinetic energy, T_i, before the collision is,

$$T_i = \frac{1}{2}m_1 v_1^2 + \frac{1}{2}v_2^2 ,$$ (2.4)

which, upon use of equations 2.2 and 2.3, becomes,

$$T_i = \frac{1}{2}MV^2 + \frac{1}{2}\mu v^2 ,$$ (2.5)

where $M = m_1 + m_2$ and $\mu = m_1 m_2/M$ is the reduced mass. The first expression on the right side of equation 2.5 can be thought of as the kinetic energy of a mass M moving with the velocity of the centre of mass, and is the kinetic energy of the centre of mass; the second term is the kinetic energy of a mass μ moving with the relative velocity, v, and is the kinetic energy of the two particles in the cm system.

In the case where the target particles (labeled as 2) are at rest in the lab frame, the kinetic energy, E_{cm}, of the reduced mass of the particles in the cm can be related to the lab kinetic energy, E_{lab}, of the beam particles (labeled as 1) by way of,

$$E_{cm} = \frac{m_2}{m_1 + m_2} E_{lab} .$$ (2.6)

These results will be required for determination of the stellar thermonuclear reaction rate in § 2.2.

2.2 Stellar Thermonuclear Reaction Rate

For a beam of mono-energetic particles, with particle number density, N_1, impinging on a target with particle number density, N_2, the reaction rate is given by the product of the effective area the target particles present to the beam, $N_2\sigma$, times the flux of incoming beam particles, N_1v. Here, σ is the effective cross sectional area that each target particle presents to the beam particles, and is, in general, a function of the relative velocity, v, between the reacting particles. The reaction rate, r_{12}, in this case is given by,

$$r_{12} = N_1 N_2 \, v\sigma(v) .$$ (2.7)

Inside a star both reacting particle species will be in motion, each having a velocity distribution spectrum, $\phi_i(v_i)$, defined such that $\int \phi_i(v_i)d^3 v_i = 1$. For a gas of non-degenerate
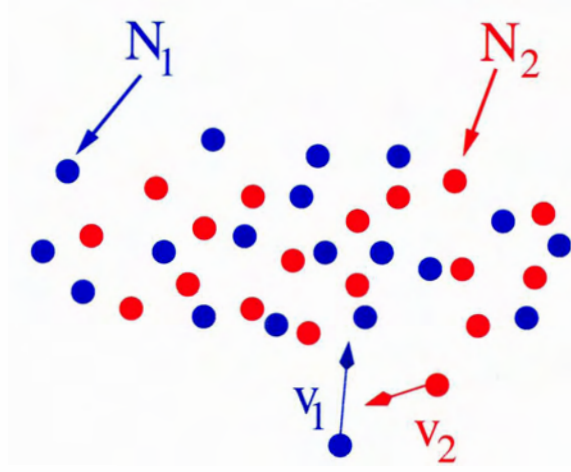
Figure 2.1: A gaseous body containing number densities of species 1 and 2 of N_1 and N_2, respectively, with velocity distributions ϕ_1 and ϕ_2.

nuclei, as shown in figure 2.1, ϕ is given by the Maxwell-Boltzmann distribution,

$$\phi_i(v_i)dv_{i_x}dv_{i_y}dv_{i_z} = \left(\frac{m_i}{2\pi kT}\right)^{3/2} \exp\left(-\frac{m_i v_i^2}{2kT}\right) dv_{i_x}dv_{i_y}dv_{i_z} , \qquad (2.8)$$

where T is the temperature and k is Boltzmann's constant. The probability that a particle from species i has a particular velocity, v_i is just the product $N_i\phi_i(v_i)$. With these, we can generalize equation 2.7 to become,

$$r_{12} = N_1 N_2 \int_{v_1} \int_{v_1} v\,\sigma(v)\,\phi_1(v_1)\phi_2(v_2)\,d^3v_1 d^3v_2 . \qquad (2.9)$$

It is convenient to write this expression in terms of centre of mass variables. The product of $\phi_1\phi_2$ can be written as,

$$\phi_1(v_1)\phi_2(v_2) = \frac{(m_1 m_2)^{3/2}}{(2\pi kT)^3} \exp\left(-\frac{m_1 v_1^2 + m_2 v_2^2}{2kT}\right) . \qquad (2.10)$$

This result allows equation 2.9 to be written as a product of three component integrals of the form,

$$\int_{v_{1_x}} \int_{v_{2_x}} \exp\left(-\frac{m_1 v_{1_x}^2 + m_2 v_{2_x}^2}{2kT}\right) dv_{1_x}dv_{2_x} ; \qquad (2.11)$$

and similarly for the y and z components. Equations 2.2 and 2.3 can each be used to isolate $\mathbf{v_1}$ and $\mathbf{v_2}$ in terms of the cm variables $\mathbf{V}$ and $\mathbf{v}$. On doing this and substituting the results into equation 2.10 we have,

$$\phi_1\phi_2 = \frac{(m_1 m_2)^{3/2}}{(2\pi kT)^3} \exp\left(-\frac{(m_1+m_2)}{2kT}V^2 - \frac{\mu}{2kT}v^2\right).$$ (2.12)

The x component of this expression can be separated out and substituted into the expression of 2.11. The Jacobian of the differentials of 2.11 is,

$$\begin{vmatrix} \frac{\partial v_{1x}}{\partial V_x} & \frac{\partial v_{1x}}{\partial v_x} \\[2mm] \frac{\partial v_{2x}}{\partial V_x} & \frac{\partial v_{2x}}{\partial v_x} \end{vmatrix} = \begin{vmatrix} 1 & m_2/M \\[2mm] 1 & -m_1/M \end{vmatrix} = 1,$$ (2.13)

leading to,

$$\int_{v_x}\int_{V_x} \exp\left(-\frac{(m_1+m_2)}{2kT}V_x^2 - \frac{\mu}{2kT}v_x^2\right) dv_x dV_x,$$ (2.14)

and similarly for the y and z components. Combining these components with equation 2.9 gives,

$$r_{12} = N_1 N_2 \left(\frac{m_1+m_2}{2\pi kT}\right)^{3/2} \int_V \exp\left(-\frac{(m_1+m_2)}{2kT}V^2\right) d^3V \quad \times$$
$$\left(\frac{\mu}{2\pi kT}\right)^{3/2} \int_v v\sigma(v) \exp\left(-\frac{\mu}{2kT}v^2\right) d^3v.$$ (2.15)

The first integral is just a Maxwell-Boltzmann distribution of the velocity of the centre of mass and is, therefore, unity. Thus, the thermonuclear reaction rate per particle pair, $\langle\sigma v\rangle$, between particle species 1 and 2 is:

$$\frac{r_{12}}{N_1 N_2} \equiv \langle\sigma v\rangle = 4\pi \left(\frac{\mu}{2\pi kT}\right)^{3/2} \int_0^\infty v^3 \sigma(v) \exp\left(-\frac{\mu}{2kT}v^2\right) dv,$$ (2.16)

where $d^3v = 4\pi v^2$ has been used. The argument of the exponent, by the result of equation 2.5, can be expressed in terms of the centre of mass kinetic energy of the two colliding particles, $E = \mu v^2/2$, to give,

$$\langle\sigma v\rangle = \left(\frac{8}{\pi\mu}\right)^{1/2} (kT)^{-3/2} \int_0^\infty E\sigma(E) \exp\left(-\frac{E}{kT}\right) dE.$$ (2.17)

Evidently, for complete evaluation, the thermonuclear reaction rate requires the mathematical form of the nuclear cross section.

2.2.1 Non-Resonant Reaction Rate

The two-body Schrödinger wave equation (SWE),

$$-\frac{\hbar^2}{2\mu}\nabla^2\Psi + V(r)\Psi = E\Psi \,, \tag{2.18}$$

where $V(r)$ is a function of spatial separation only, has separable solutions in terms of the spherical coordinates, (r,θ,ϕ), given by: $\Psi(r,\theta,\phi) = f(r)Y_l^m(\theta,\phi)$, with Y_l^m the well-known spherical harmonics. Transforming equation 2.18 to spherical coordinates gives the radial equation [21],

$$-\frac{\hbar^2}{2\mu}\frac{d^2\chi(r)}{dr^2} + \left[\frac{\ell(\ell+1)\hbar^2}{2\mu r^2} + V(r) - E\right]\chi(r) = 0 \,, \tag{2.19}$$

with $f(r) = \chi(r)/r$ and ℓ the quantum number of relative angular momentum between the two particles. The strong nuclear force is extremely short range and is effectively zero outside the volume defined by the nucleus. Therefore, for a system of two approaching charged particles, equations 2.18 and 2.19 hold in the spatial domain outside overlap of the nuclear surfaces of the two particles. In this system $V(r)$ is the Coulomb potential and, by equation 2.19, the effective potential barrier is given by,

$$V_\ell(r) = \frac{\ell(\ell+1)\hbar^2}{2\mu r^2} + \frac{Z_1 Z_2 e^2}{r} \,, \tag{2.20}$$

where Z_i is the elementary nuclear charge of each nucleus in integer units.

The fusion of two charged particles requires their tunneling through the repulsive potential barrier, $V_\ell(r)$, so that their nuclear surfaces overlap, at which point the strong, short-range, nuclear force can bind the two together. This contact distance between the nuclear surfaces is $R_0 = 1.35\,(A_1^{1/3} + A_2^{1/3})$ fm, with A_i the respective atomic mass number of each nucleus. The quantum tunneling probability, $P_\ell(E)$, is given by the WKB approximation as [21, 35],

$$P_\ell(E) \propto \exp\left(-\frac{2\sqrt{2\mu}}{\hbar}\int_{R_0}^{R_c}\sqrt{V_\ell(r) - E}\,dr\right) \,, \tag{2.21}$$

with R_c the classical turning point, where $E = V$. Clearly, the tunneling probability is highest for $\ell = 0$, and with this simplification the argument of the exponential of expression 2.21 can be expressed as,

$$\frac{4Z_1 Z_2 e^2}{\hbar v}\left[\frac{\pi}{2} - \left(\frac{E}{E_c}\right)^{1/2}\left(1 - \frac{E}{E_c}\right)^{1/2} - \arcsin\left(\frac{E}{E_c}\right)\right] \,. \tag{2.22}$$

Additionally, the cross section for any reaction is also proportional to the square of the de Broglie wavelength of the reduced mass system; this introduces a factor of $1/E$ into the expression for cross section. Thus, we can write the non-resonant cross section as,

$$\sigma(E) = \frac{S(E)}{E} \exp\left(-\frac{2\pi Z_1 Z_2 e^2}{\hbar v}\right), \qquad (2.23)$$

where the function $S(E)$, called the "astrophysical S-factor", has been introduced as a means to parametrically account for these approximations and any additional contributions to the cross section by way of nuclear structure effects.

Empirically it is often found that the astrophysical S-factor is nearly constant over a broad range of energies at stellar temperatures [19]. Substituting the result of equation 2.23 into 2.17, treating $S(E) = S(E_0)$ as a constant, results in,

$$\langle \sigma v \rangle = \left(\frac{8}{\pi\mu}\right)^{1/2} (kT)^{-3/2} S(E_0) \int_0^\infty \exp\left(-\frac{E}{kT} - \frac{b}{\sqrt{E}}\right) dE, \qquad (2.24)$$

where

$$b = 2\pi \frac{Z_1 Z_2 e^2}{\hbar} \left(\frac{\mu}{2}\right)^{1/2} = 31.27 \, Z_1 Z_2 \, \mu^{1/2} \, (\text{keV})^{1/2}.$$

The integrand is a product of the exponential tail of the Maxwell-Boltzmann distribution, which vanishes at high energies, with the exponential of the penetrability factor, which rapidly vanishes at low energies. The product of these overlapping tails results in a peaked distribution function known as the Gamow window, and is depicted in figure 2.2. Clearly, only those particles with energies in the the extreme high energy portion of the Maxwell-Boltzmann distribution will contribute to the non-resonant reaction rate.

By taking the first derivative of the integrand of equation 2.24 and equating it to zero, the effective burning energy for thermonuclear reactions, E_{eff}, can be determined for the Gamow window. The result is [19, 21],

$$E_{\text{eff}} = \left(\frac{bkT}{2}\right)^{2/3} = 1.22(Z_1^2 Z_2^2 \, \mu T_6^2)^{1/3} \, \text{keV}. \qquad (2.25)$$

Substitution of this result into the expression of the integrand in equation 2.24 results in a maximum value for the integrand, I_{max}, of

$$I_{\text{max}} = \exp\left(-\frac{3E_{\text{eff}}}{kT}\right).$$
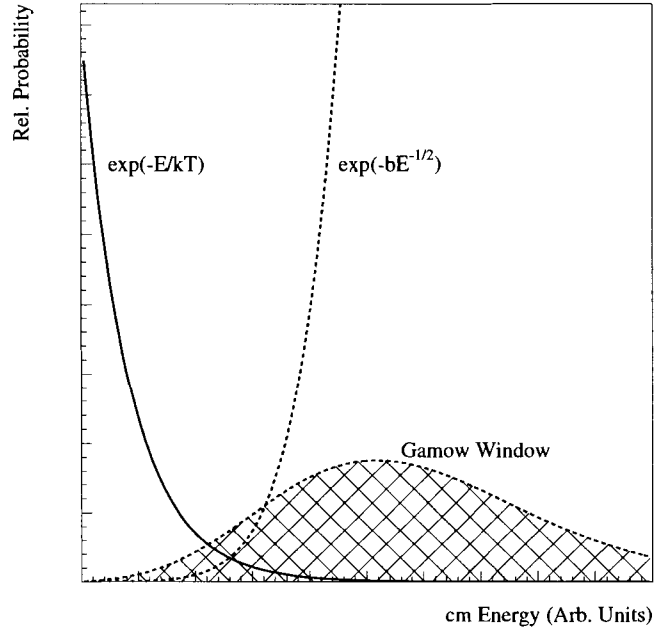
Figure 2.2: The Gamow window distribution function (hatched) results from the product of the sharply falling tails of the Maxwell-Boltzmann distribution with the penetrability factor. The relative scaling between the curves has been exaggerated.

The distribution for the Gamow window is often approximated with a Gaussian function, viz,

$$\exp\left(-\frac{E}{kT} - \frac{b}{\sqrt{E}}\right) \approx I_{\max} \exp\left[-\left(\frac{E - E_{\text{eff}}}{\Delta/2}\right)^2\right] , \qquad (2.26)$$

with Δ the effective width of the Gamow window. This width is determined by matching the second derivatives on both sides of equation 2.26 at $E = E_{\text{eff}}$; the result being [19, 21],

$$\Delta = \frac{4}{\sqrt{3}} \left(E_{\text{eff}} \, kT\right)^{1/2} = 0.75 \, (Z_1^2 Z_2^2 \, \mu T_6^5)^{1/6} . \qquad (2.27)$$

Non-resonant nuclear reactions take place predominantly within the energy window: $E = E_{\text{eff}} \pm \Delta/2$. Thus, information regarding the nuclear structure of the compound nucleus formed through nuclear reactions at Gamow window energies is important for determining

the stellar reaction rate. For example, significant enhancement of the reaction rate can occur if the compound nucleus possesses quasi-stationary states in the Gamow window, by way of resonant reactions. For the purposes of resonant reactions, the width of the Gamow window tells us the relevant energy range in the compound nucleus, above the proton threshold, where quasi-stationary states can contribute to the stellar reaction rate. We return to this important feature in § 2.4, where we discuss ^{21}Na burning at nova temperatures.

2.2.2   Resonant Reaction Rate

When the energy of the reduced mass system is such that it is equal, or close, to the energy of a resonance state in the compound system, the reaction cross section can be greatly enhanced. Qualitatively, this enhancement arises due to an optimal matching of the amplitudes of the reduced mass system wave function with the wave function of the quasi-stationary state. Reactions occurring under such conditions are called resonant reactions and the cross section is given by the Breit-Wigner formula [36],

$$\sigma(E) = \frac{\lambda^2}{4\pi} \frac{2J_r + 1}{(2J_p + 1)(2J_t + 1)} \frac{\Gamma_p \Gamma_\gamma}{(E - E_r)^2 + (\Gamma/2)^2} , \qquad (2.28)$$

where $\Gamma = \Gamma_p + \Gamma_\gamma$ is the total resonance width; Γ_p and Γ_γ the partial widths of the entrance and exit channels of the reaction, respectively; $\lambda = h/\sqrt{2\mu E}$ is the centre of mass de Broglie wavelength, and J_r, J_p and J_t the spins of the resonance state and the two reacting particles, respectively. The partial width for a charged particle, Γ_p, is proportional to the tunneling penetrability [36], highlighting the importance of the Gamow window in determining what resonant states can contribute to thermonuclear reactions.

Substitution of equation 2.28 into the reaction rate formula of equation 2.17 will produce an integral of the form,

$$\int_0^\infty \lambda^2 \frac{\Gamma_p \Gamma_\gamma}{(E - E_r)^2 + \alpha^2} E \exp\left(-\frac{E}{kT}\right) dE = \frac{h^2}{2\mu} \int_0^\infty \frac{\Gamma_p \Gamma_\gamma}{(E - E_r)^2 + \alpha^2} \exp\left(-\frac{E}{kT}\right) dE , \qquad (2.29)$$

where $\alpha \equiv \Gamma/2$, and where all terms in the integrand have energy dependence. For a very narrow resonance, $\Gamma \ll E_r$, the range of integration in expression 2.29 is effectively restricted to values of E sufficiently close to E_r that the exponential and Γ's can be replaced by their values at E_r, and taken out of the integral. The remaining integral over the Lorentzian

leads to the result,

$$\frac{\pi\hbar^2}{\mu}\frac{\Gamma_p\Gamma_\gamma}{\Gamma}\exp\left(-\frac{E_r}{kT}\right).$$ (2.30)

Substitution of this into equation 2.17, accounting for all of the constants, results in the narrow resonance reaction rate per particle pair:

$$\langle\sigma v\rangle = \left(\frac{2\pi}{\mu kT}\right)^{3/2}\hbar^2\omega\gamma\exp\left(-\frac{E_r}{kT}\right),$$ (2.31)

where,

$$\omega = \frac{2J_r+1}{(2J_p+1)(2J_t+1)}$$ (2.32)

and,

$$\gamma = \frac{\Gamma_p\Gamma_\gamma}{\Gamma},$$ (2.33)

and the product $\omega\gamma$ is called the resonance strength; it is the nuclear physics dependent term in the reaction rate. Of note here is that the resonant stellar reaction rate is *exponentially* dependent on the resonance energy, emphasizing the importance of knowing the energies of those resonance states which lie in the Gamow window.

When several narrow, isolated, resonances are present within the Gamow window, then the resonant reaction rate per particle pair becomes a sum over all contributing resonances within the window; namely,

$$\langle\sigma v\rangle = \left(\frac{2\pi}{\mu kT}\right)^{3/2}\hbar^2\sum_i(\omega\gamma)_i\exp\left(-\frac{E_{r_i}}{kT}\right).$$ (2.34)

This work reports on the first ever direct measurements of the resonance strengths of two states in the ^{22}Mg nucleus of astrophysical interest for ONe novae nucleosynthesis.

The next section details how measurements of $\omega\gamma$ are determined from nuclear reaction yields.

2.3 Thick Target Yield

Consider a thin target, of thickness Δx, containing number density, N_t, of target nuclei per unit volume. The quantity, $N_t\Delta x$, can be regarded as the effective number of nuclei present in a monolayer of atoms within the target, or the areal density of target nuclei. The

product of this with the cross section, σ, for the reaction will be the yield for a single beam particle traversing the target. These concepts are illustrated in figure 2.3. When the target is thin enough, such that the energy dependence of the beam particles and σ does not vary appreciably, the thin target yield, Y, per incident beam particle is just,

$$Y = N_t \sigma \Delta x .$$
(2.35)
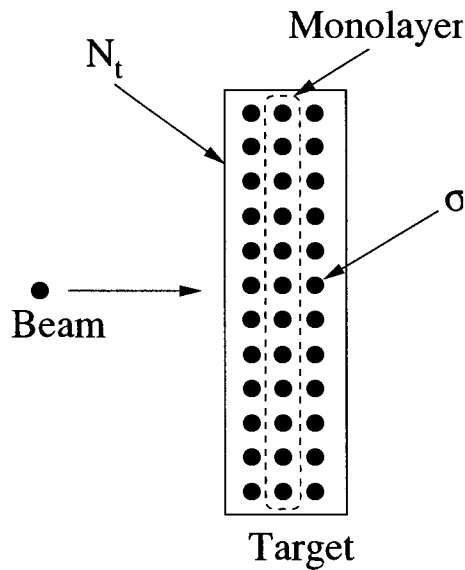
Figure 2.3: Schematic diagram relating the nuclear cross section to reaction yield.

For the case where the target is sufficiently thick that the beam energy and σ change appreciably, equation 2.35 must be integrated over the entire target thickness to obtain the yield. Let the target have a thickness, in energy units, of Δ, and the beam have incident energy E. The beam particles, on transiting the target, will lose kinetic energy in the form of ionization energy loss. This ionization energy loss is known as the stopping power [37], $S(\mathcal{E}) = -dE/dx$, and is the energy change per unit distance traversed through the target material by the beam particle. Clearly, $\Delta = \int S(\mathcal{E}) \, dx$, integrated over the target thickness. The stopping power is usually expressed instead by the stopping cross section, ε, defined

by,

$$\varepsilon = \frac{1}{N_t} \frac{dE}{dx} , \qquad (2.36)$$

where N_t is the number density (atoms cm^{-3}) of the target material. Expressed in this way, ε corresponds to the energy loss for a monolayer of atoms [19], in analogy with the previous discussion leading to equation 2.35. With these, the yield per incident particle becomes,

$$Y = \int \sigma(E) N_t \, dx = \int_{E-\Delta}^{E} \frac{\sigma(E)}{\varepsilon(E)} \, dE . \qquad (2.37)$$

When the cross section is described by the Breit-Wigner formula 2.28 and the resonance width is very narrow so that $\Delta \gg \Gamma$ (thick target), the energy variation of λ, Γ_p, Γ_γ, Δ and ε is negligibly small over the region of the resonance, and these can therefore be regarded as constants for the purposes of integrating. With these caveats, we are left with integrating over the Lorentzian form of the cross section formula 2.28. The result is,

$$Y = \frac{\lambda^2}{2\pi} \frac{m_1 + m_2}{m_2} \varepsilon^{-1} \omega\gamma \left[\arctan\left(\frac{E - E_r}{\Gamma/2} \right) - \arctan\left(\frac{E - E_r - \Delta}{\Gamma/2} \right) \right] . \qquad (2.38)$$

This expression defines the thick target yield curve. It is important to note that, as a result of the above caveats, all values in 2.38 are to be evaluated at the resonance energy, particularly λ. The ratio of masses in equation 2.38 arises from conversion of the lab value of ε into its centre of mass value by way of expression 2.6. Formula 2.38, for a given Δ, has a maximum value at $E = E_r + \Delta/2$ [38], so that the maximum yield, $Y_{\max}$, is,

$$Y_{\max} = \frac{\lambda^2}{\pi} \frac{m_1 + m_2}{m_2} \varepsilon^{-1} \omega\gamma \arctan\left(\frac{\Delta}{\Gamma} \right) . \qquad (2.39)$$

For the thick target condition $\Delta \gg \Gamma$, this reduces to,

$$Y_{\max}(\infty) = \frac{\lambda^2}{2} \frac{m_1 + m_2}{m_2} \varepsilon^{-1} \omega\gamma . \qquad (2.40)$$

Figure 2.4 shows a plot of the thick target yield curve, normalized to $Y_{\max}(\infty)$, where it is seen that the inflection point of the low energy shoulder occurs at E_r and the 25% and 75% yield points correspond to $E_r - \Gamma/2$ and $E_r + \Gamma/2$, respectively. It is also evident from equation 2.40 that the thick target yield is independent of the density of the target material, as ε is density independent. This means that the depth within the target where the resonance reaction takes place will be at a fixed location for a fixed beam energy.
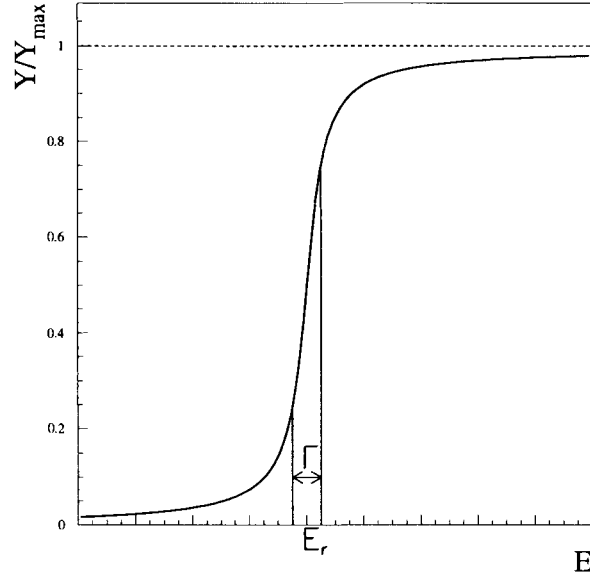
Figure 2.4: The thick target yield curve. The inflection point of the low energy shoulder occurs at E_r and the 25% and 75% yield points correspond to $E_r - \Gamma/2$ and $E_r + \Gamma/2$, respectively.

In the experimental situation the beam energy is not mono-energetic, but has a small energy spread. Also, during its transit through the target material, the beam incurs energy straggling causing its energy profile to broaden. Under these conditions the yield function is, in general, a double convolution of the Breit-Wigner function with a Gaussian representing the beam energy spread and another Gaussian representing the energy straggle. For ISAC beams, the beam energy spread, Δ_b, is $\approx 0.5\%$ of the beam energy, or ≈ 1.1 keV/u at a beam energy of 220 keV/u. The energy straggling can be calculated from the Bohr straggling model [39]. The rms energy spread caused by energy straggling, ΔS, is given by,

$$\Delta S = (4\pi z e^4 N Z \Delta x)^{1/2} \, , \tag{2.41}$$

where ze and Ze are the projectile and target atomic charges, respectively, N is the number of target atoms per cubic centimeter, and Δx is the thickness of the target. For the DRAGON H_2 gas target at 4.6 Torr pressure, the result is $\Delta S \approx 10.5$ keV. The total energy loss of the

beam through the target for this work, on the other hand, is $\approx$ 300 keV, which is much larger than both the straggle and the intrinsic energy spread. Gove [40] has shown under these conditions ($\Delta \gg \Delta_b \gg \Gamma$) that the thick target yield, $Y_{max}(\infty)$, remains unaffected by straggle and beam energy spread. In effect, the target is thick enough to ensure that all beam particles will be able to contribute to the integral of the cross section for maximum thick target yield for some range of beam energies contained in the central region of the target energy thickness.

From these results, we now see the connection between measurements in the laboratory and the explosive burning in novae: a direct measurement of the thick target yield at maximum, $Y_{max}(\infty)$, for a known resonance energy, leads directly to the resonance strength and, hence, the resonant reaction rate.

2.4 ^{21}Na Burning at Nova Temperatures

Typical ONe nova temperatures are between $T_6 = 100$ at onset of proton burning on heavy ions, up to $T_6 = 400$–500 at peak outburst temperature [16]. Figure 2.5 shows a sequence of Gamow windows for the ^{21}Na(p,γ)^{22}Mg reaction at three temperatures: 170 MK, 240 MK, and 400 MK. The solid lines are the Gamow distribution and the dashed curves are the Gaussian approximation to it, as previously described in § 2.2.1. As is evident in the first two panels of figure 2.5, the peak of the Gamow distribution centres around a cm energy of $\approx$ 200 keV. Moreover, all panels show that, throughout the temperature range of the nova, the width of the Gamow distribution will cover cm energies up to $\approx$ 460 keV.

The present ^{22}Mg level scheme [41–43] is shown in figure 2.6, with excitation energies (in units of MeV), spin and parities labeled. Shown on the far left side are the cm energies, in keV. On the right side, characterized by red vertical bars, are the associated widths of the Gamow distributions displayed in figure 2.5, labeled by temperature in units of T_6. The span in energy of the widths of the Gamow distributions indicate that there are two states in ^{22}Mg above the proton threshold energy of 5.502 MeV [44], at cm energies of 212 and 335 keV, that are candidates for resonant reaction burning at ONe nova temperatures. The contribution to the reaction rate of the state at 460 keV is marginal except for in the case of the more massive ONe novae, with temperatures exceeding 400 MK. The state at cm energy 212 keV, as indicated by all panels of figure 2.5, is bracketed by the peak of the Gamow
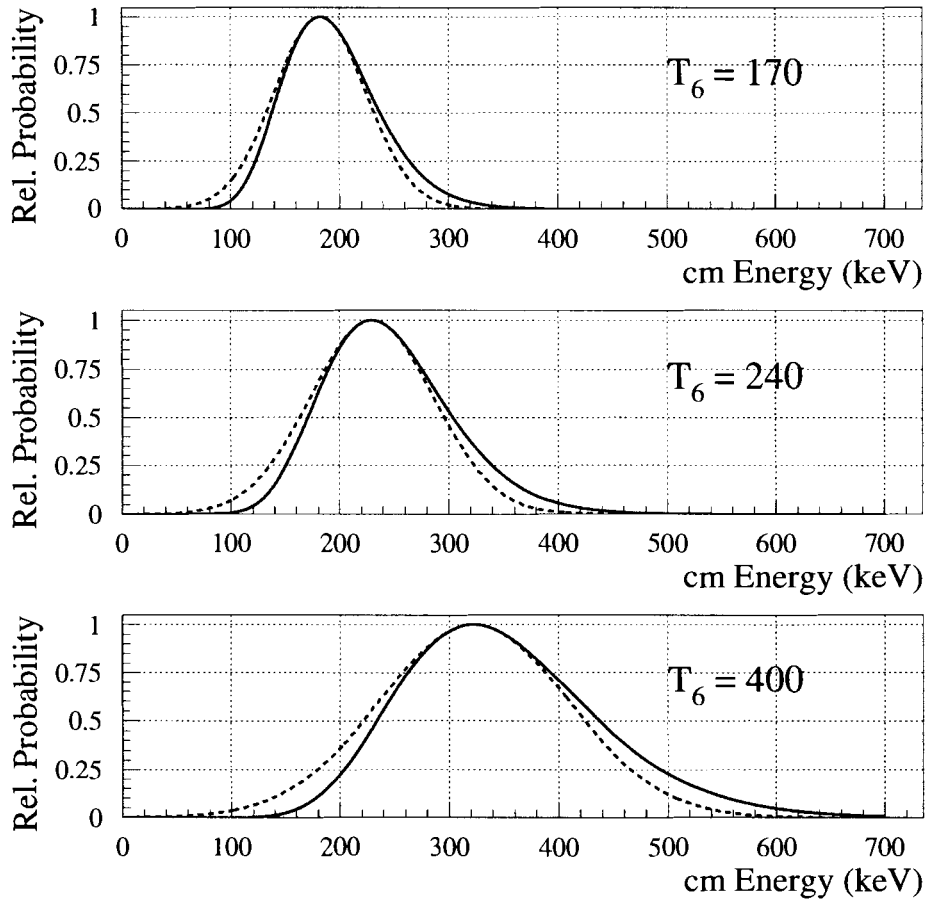
Figure 2.5: The Gamow window for proton capture on ^{21}Na at nominal ONe nova temperatures. The upper panel shows the Gamow window for an intermediate shell temperature of $T_6 = 170$; the lower panel the Gamow window for a peak temperature of $T_6 = 240$. Note that the the peak of the window centres around $E_{cm} = 200$ keV. Solid lines are the integrand of equation 2.24, dashed lines are the Gaussian approximation.
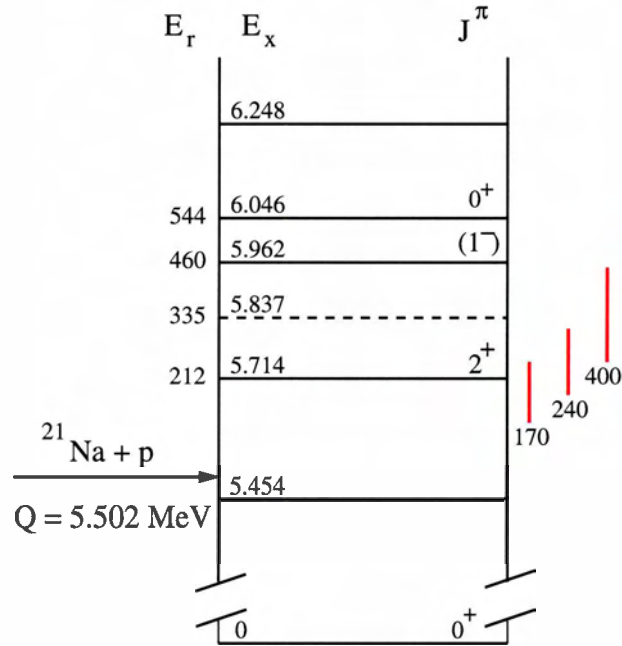
Figure 2.6: The ^{22}Mg level scheme for the states of astrophysical interest for ONe novae, with excitation energies in MeV. The numbers on the left denote the cm energies of the excited states. The red lines at right denote the Gamow window, relative to the excitation, energies at the temperatures (in units of T_6) indicated.

distribution for most of the entire energy range of burning at the onset of proton capture on heavy ions. We therefore expect, from the point of view of the burning temperatures within ONe novae, that the state at $E_r = 212$ keV will be significant for resonant proton capture on ^{21}Na. In addition, this state being a $J^\pi = 2^+$ implies that any resonant reaction that does occur will be by way of the s-wave channel, as the ground state spin of ^{21}Na is $J^\pi = 3/2^+$, providing further enhancement relative to those states requiring higher angular momentum transfer.

The two states at 212, 335 and 460 keV are within the width of the Gamow window for ONe nova temperatures, and the first two of these have been chosen for radiative proton capture studies to directly determine their resonance strengths, $\omega\gamma$, and hence, their contributions to the ^{21}Na(p,γ)^{22}Mg reaction rate in ONe novae.

This study was performed using the DRAGON recoil mass separator at the ISAC radioactive ion beam facility and it is to these that we turn to in the next chapter.

Chapter 3

Experimental Facilities

This reaction study was carried out in "inverse kinematics", employing a radioactive heavy ion beam, impinging on a windowless hydrogen gas target. As such, mass separation of the extremely rare fusion recoils from the unreacted radioactive beam particles is demanded. The first section of this chapter discusses the ISAC radioactive ion beam (RIB) facility at TRIUMF, which provided the ^{21}Na ion beam which made this experiment possible. The second part of this chapter discusses the details of the DRAGON recoil mass separator, wherein the fusion reaction yields were measured; namely: the gas target, gamma array, optics, and final focus heavy ion detector system.

3.1 ISAC RIB Facility

The ISAC (Isotope Separator and ACcelerator) radioactive ion beam facility is located at the TRIUMF national laboratory in Vancouver, Canada, and its experimental hall holds the DRAGON apparatus. The 500 MeV cyclotron of TRIUMF serves as the driver of the ISAC facility, delivering $10 \, \mu A$ of 500 MeV protons through beamline 2C onto a thick target located in a heavily shielded vault. Spallation reactions within the target material, induced by the proton bombardment, produce radioactive isotopes of experimental interest. These isotopes are extracted from the target and collimated into a beam. Selection of a specific isotope of experimental interest is then done by passing this beam through a high resolution mass separator magnet. From here, a beam consisting of a specific isotope is then directed from the shielded basement area of ISAC up to the ground floor of the facility where it is

33

either directed to an experiment in the low energy experimental section of ISAC, or directed into a radio frequency quadrupole (RFQ) accelerator followed by a drift tube linear accelerator (DTL) for use in the high energy experimental section of ISAC. Figure 3.1 shows a three dimensional cut-away of the ISAC facility showing all the key features heretofore described. Success of this experiment relied critically on the ISAC target and accelerators which are described in more detail next.
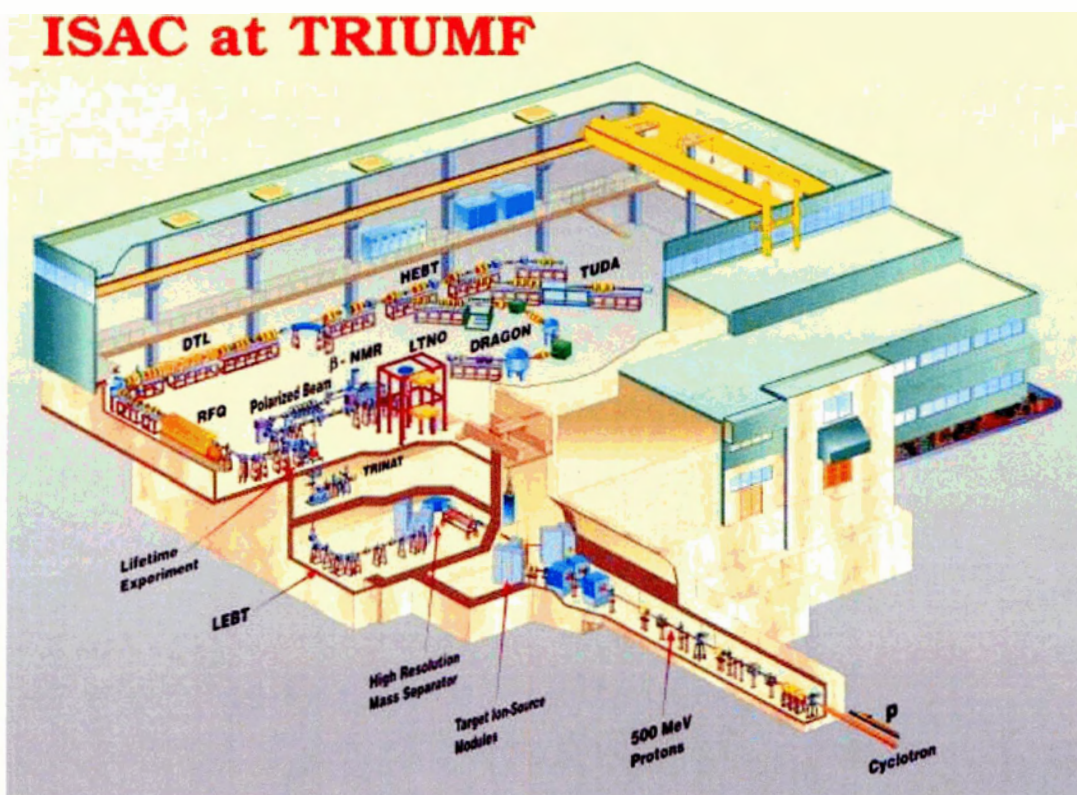
Figure 3.1: Three dimensional cut-away view of the ISAC facility showing the location of the target cell, accelerators and the DRAGON facility. Isotopes produced in the target ion source are first mass separated, for a specific isotope of interest, and brought to the ground-floor experimental hall for post acceleration, through the RFQ and DTL, into DRAGON.

3.1.1 ISAC Target

The ISAC target and ionization source design is that of a surface ionization source primarily based on design concepts developed through empirical studies done with the former TISOL [45] facility, now decommissioned. A surface ionization source consists of a target oven comprised of a hollow cylindrical tube in which the target material is contained and heated to temperatures $\sim 2000\ ^\circ C$. Attached at right angles to the target oven, and open to the oven's volume, is the ionizer tube: a shorter, smaller diameter hollow tube of the same material as the target oven. At the opposite end of the ionizer tube is a small exit aperture. As radioisotopes are produced by spallation reactions in the target material and diffuse out of the target material lattice, they will eventually make contact with the inner walls of the oven and the ionizer tube. If the work function of the oven and ionizer tube is higher than the ionization potential of the chosen isotope of interest, electron transfer from the isotope atom to the ionizer tube will take place, creating singly charged atomic ions. These ions will effuse down the ionizer tube and exit through the ionizer tube exit aperture which is kept small in order to keep the emittance of the exiting ions as small as reasonably possible, while still allowing enough to exit per unit time to form an appreciably intense beam. The high temperature of the target oven is chosen to enhance the diffusion rate of ions out of the target material as well as enhancing the ionization efficiency of the ionizer. Figure 3.2 shows a photograph [46] of an ISAC tantalum target oven: the 3-pronged electrode provided the DC current for heating this oven, and the half-twist Ta strips at each end of the oven provided for electrical return as well as rigid mounting in the final assembly. Attached at the centre of the length of the target oven can be seen the ionizer tube.

Initial acceleration of the ions is provided by the electrostatic potential applied to the oven/ionizer. Upon exiting the ionizer tube, the positive ions enter a region of high electric potential (HV): approximately 2 mm downstream of the ionizer exit aperture is an extraction electrode nominally set at a potential 10% lower in value than the total bias put on the target oven and ionizer. This electrode contains an aperture opening of similar size to that of the ionizer exit aperture. This geometry provides the initial extraction acceleration from the ion source and collimates the ions into a focused "pencil beam". Downstream of the extraction electrode is a ground electrode of similar shape, but larger acceptance aperture. The total kinetic energy imparted to the ions is therefore the potential difference between the ionizer
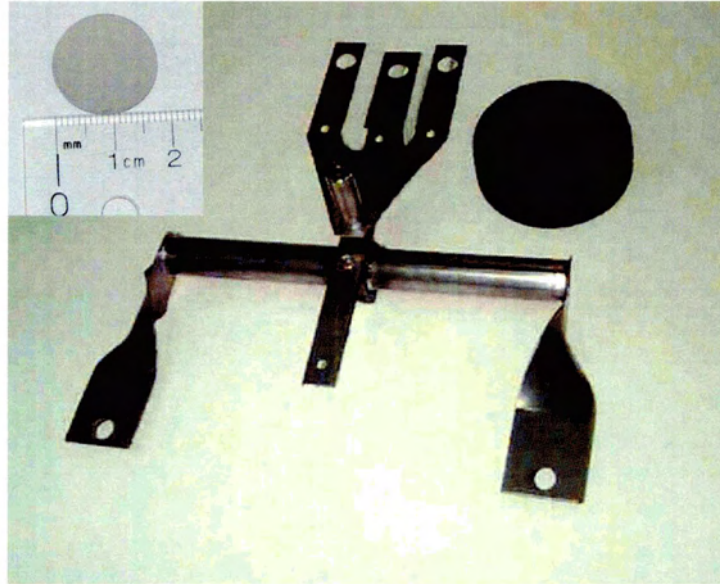
Figure 3.2: The Ta target oven, showing ionizer tube and electrodes. Puck shown for scale. Top left inset: SiC target disk.

and the ground electrode. The schematic diagram [46] of figure 3.3 shows an elevation view of the ISAC target design, detailing the geometry of the electrodes and the oven/ionizer. Finally, electrostatic steering plates downstream of the ground electrode provide for beam transmission optimization prior to its entrance to the ISAC low energy electrostatic beam transport system.

Specifically, for this experiment the target material consisted of compressed discs of silicon carbide granules, ≈ 0.5 mm thick and 17 mm in diameter, with the top one-quarter of the disc cleaved off. The top left inset of figure 3.2 shows a SiC disc prior to cleaving. The target oven was a tantalum tube (190 mm long $\times$ 17 mm diameter) within which were stacked the SiC discs. The length of the stack was $\approx 1/4$ the length of the target oven, with the cleaved portion of the discs co-aligned, leaving a vacuum gap along the top of the discs within the target oven; thus providing an effusion volume for the ions to make their way into the ionizer tube. The midpoint along the length of the stack coincided with the geometric centre along the target oven's length. The ends of the SiC stack were sealed using Ta end-caps.
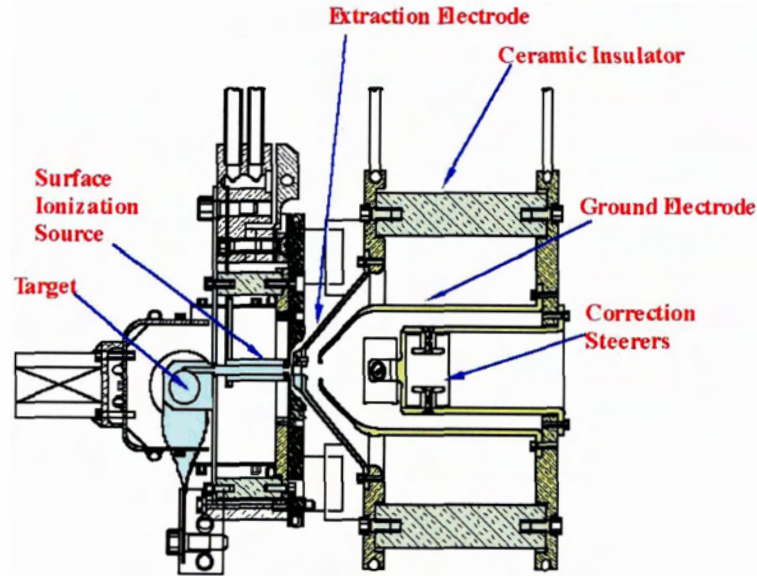
Figure 3.3: Elevation view schematic diagram of the ISAC target assembly. Target oven/ionizer is shown in light blue and the TRIUMF cyclotron proton beam enters the oven perpendicular to the page at the location marked by the arrow labeled "Target".

3.1.2 ISAC Accelerators and Beam Transport

Once extracted from the ion source, the ions are transported through the ISAC high resolution ($M/\Delta M = 5000$) mass separator (figure 3.1) for mass selection of the species of experimental interest. From here, the beam is brought to the experimental hall where it is injected into a radio frequency quadrupole (RFQ) accelerator [47] at an energy of 2 keV/u. The RFQ, operating at 35 MHz, bunches and transversely focuses the input DC beam into a pulsed beam consisting of discrete timing packets, separated in time by 85 ns – three RF periods. Figure 3.4 shows accelerator commissioning data [48] of a 230 keV/u beam of $^{14}N^{4+}$ ions, clearly showing the 85 ns time structure of beam pulses. Beam exits the RFQ having been accelerated to a fixed energy of 150 keV/u and enters the medium energy beam transport (MEBT) section of the beam line.

Immediately downstream of the RFQ, a buncher provides energy focusing of the beam before its passage through a $\approx 10~\mu g~cm^{-2}$ thick carbon foil; this to correct for the beam
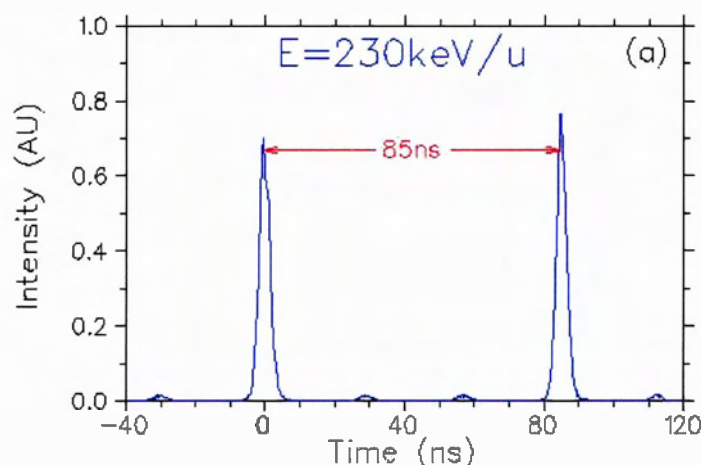
Figure 3.4: ISAC accelerator commissioning data of accelerated 230 keV/u $^{14}N^{4+}$ beam showing the 85 ns pulsed structure of the beam.

energy straggling as it passes through the foil. Passage through the foil strips electrons from the ions and results in ions populating a distribution of charge states. The optics of the beam transport system downstream of the stripper foil are optimized for the charge state of highest probability: 5^+ for the ^{21}Na beam used in this work. From the foil the ions are passed through two 45° magnetic dipole benders, thereby filtering out those ions of charge states different from 5^+. The remaining beam is then time bunched for phase matching with the DTL RF cycle. Passage through the five-tank drift-tube linear accelerator (DTL) ensues, resulting in a time bunched beam of variable energy from 150 to 1500 keV/u in energy, to finally be delivered downstream to DRAGON. Figure 3.5 shows the layout of the ISAC RFQ, MEBT and DTL systems thus described.

3.2   DRAGON Facility

The DRAGON (Detector of Recoils And Gammas Of Nuclear reactions) facility at TRI-UMF consists of four main components: a differentially pumped, recirculating, windowless hydrogen gas target; a BGO γ-detector array; an electromagnetic mass separator (EMS); and a final focus heavy ion detector system. It has been designed to measure heavy ion radiative
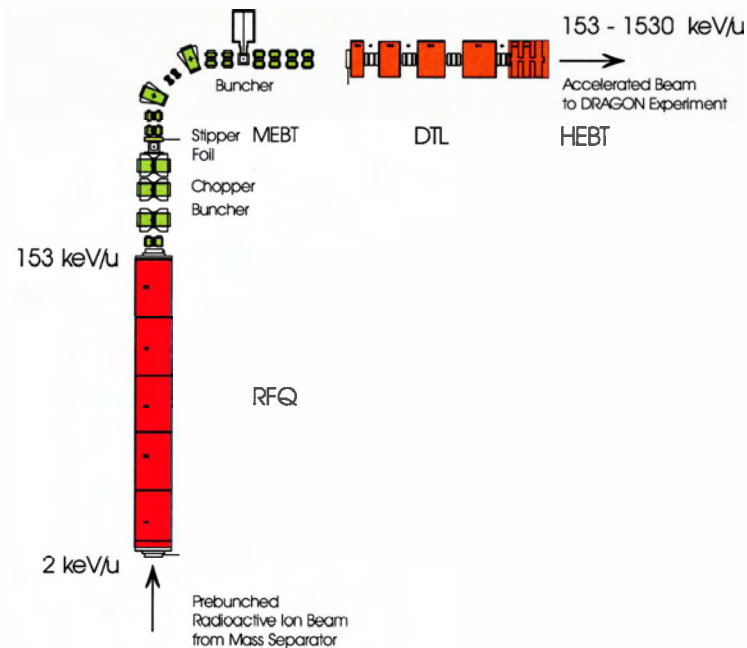
Figure 3.5: Plan view schematic diagram of the ISAC RFQ and DTL accelerators.

proton capture reactions at sub-Coulomb barrier energies[1] in inverse kinematics. Radiative proton capture into an excited state of the fusion product nucleus takes place within the gas target and this excited state promptly decays by γ-ray emission(s). Because the reaction proceeds via inverse kinematics, both fusion recoils and the much higher intensity beam particles exit the gas target in the downstream direction. Momentum conservation demands that the fusion recoils have a momentum distribution essentially the same as that of the beam; differing only by a small momentum spread caused by the γ-ray emission. Thus, these reaction kinematics, combined with the small reaction cross section, require a mass separator with high beam suppression ($\sim 10^{12}$) capability to suppress the high intensity beam particles from the rare fusion recoils of interest.

Figure 3.6 schematically shows a three dimensional cut-away view of the DRAGON facility, showing the main components. The heavy ion beam is incident on the gas target from the left. A γ-array, surrounding the gas target, detects the γ-ray(s) from the nuclear

---

[1]The Coulomb barrier for ^{21}Na(p,γ)^{22}Mg is $\approx$ 3.5 MeV. In contrast, from § 2.2.1, the centre-of-mass energy for this reaction in novae is $\approx$ 10 times lower.

reaction. Exiting the downstream side of the gas target, fusion recoils and beam particles enter the EMS; which employs a combination of magnetic and electrostatic benders to mass separate the fusion recoils from the beam ions. Finally, a recoil detector at the end of the DRAGON EMS, comprised of a double sided silicon strip detector (DSSSD), measures the total energy and position of any ions impinging on it. These systems are discussed in detail in what follows.
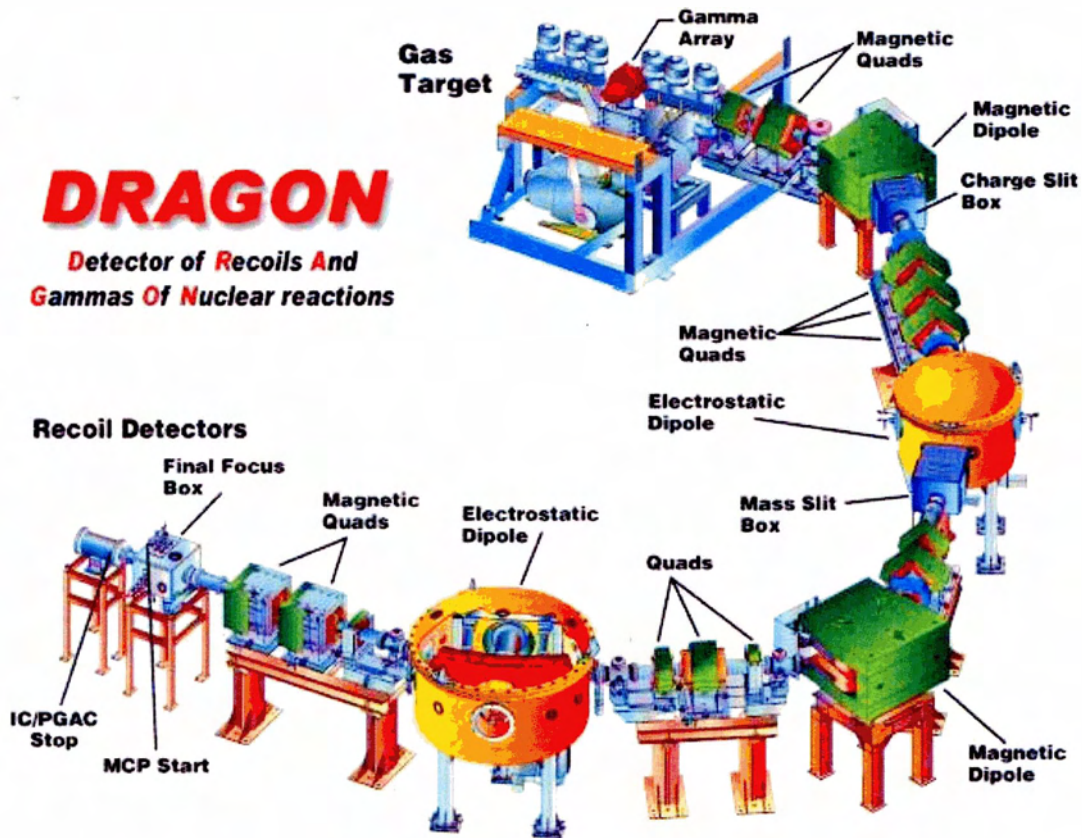
Figure 3.6: Three dimensional cut-away view of the DRAGON facility.

3.2.1   Electromagnetic Separator

Figure 3.7 schematically depicts a single transition γ-decay of an excited-state recoil nucleus, with all angles defined with respect to the beam axis. The initial momentum, p^*, of the excited recoil nucleus, by momentum conservation, is that of the beam; namely, $p^* = \sqrt{2m_b E_b}$, with m_b and E_b the beam particle mass and energy, respectively. Subsequently to
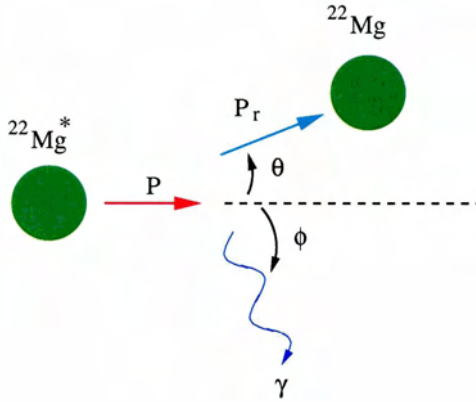
Figure 3.7: The inverse kinematics of heavy ion on light proton demand that the fusion products exit the gas target in the forward direction within a kinematic recoil cone of lab-angle θ.

the γ-decay, in terms of the lab angle, ϕ, of the emitted γ-ray, the associated lab angle of the ground state recoil nucleus is given by,

$$\theta = \arctan\left[\frac{\sin \phi}{\frac{\sqrt{2m_b E_b}}{E_\gamma/c} - \cos \phi}\right], \tag{3.1}$$

with E_γ the γ-ray energy and c the speed of light. When the γ-emission angle is

$$\phi = \arccos\left[\frac{E_\gamma/c}{\sqrt{2m_b E_b}}\right] \approx \pi/2, \tag{3.2}$$

the angular deviation away from the beam axis of the recoil nucleus is maximum. In this instance, equation 3.1 implies that fusion recoils will exit the gas target confined within a "recoil cone" of half-angle, $\theta_{1/2}$, given by,

$$\theta_{1/2} = \arctan\left[\frac{E_\gamma/c}{\sqrt{2m_b E_b}}\right] \tag{3.3}$$

For γ-ray emission collinear with the beam axis ($\phi = 0, \pi$), the ratio in the brackets of equation 3.3 is also the fractional difference in momentum of the de-excited recoil nucleus from that of the beam; namely,

$$p_r = p^* \pm p_\gamma = \sqrt{2m_b E_b} \left(1 \pm \frac{E_\gamma/c}{\sqrt{2m_b E_b}} \right) ,$$ (3.4)

with p_r the momentum of the de-excited recoil nucleus (figure 3.7).

For typical excitation energies of ≈ 6 MeV and beam energies of ≈ 5 MeV, as is the case for this work, equation 3.3 produces a recoil cone angle of ≈ 13 mrad and equation 3.4 shows that the momentum spread of the de-excited recoil nucleus will only be approximately $\pm 1.5\%$. This small fractional difference in momentum of the recoil nucleus from the beam momentum precludes mass separation of fusion recoils from beam ions using a magnetic bending separator only. Furthermore, with the recoil products spatially diverging, as a result of the kinematic recoil cone, optical focusing elements immediately downstream of the gas target are required for successful mass separation. Thus, the design of the separator must take these considerations into full account for successful study of these reactions of extremely small cross section.

Consisting of a series of magnetic dipoles (MD), magnetic quadrupoles (Q), magnetic sextupoles (S) and electrostatic dipoles (ED), the separator design [49] is based on two stages of mass separation. The first stage is comprised of an arrangement of quadrupoles, and dipoles in the order: QQ(MD)SQQQS(ED). The second stage is formed by the arrangement: QQS(MD)QS(ED)QQ. Located downstream of the gas target, a quadrupole doublet acts to bring the diverging recoil particles to a momentum dispersive focus 31 cm downstream of the first dipole magnet (MD1). Charged particles traversing the field region of MD1 will be carried along circular trajectories. By Newton's second law, the centripetal force of the ion must be equal to the Lorentz force acting on the ion as it traverses the dipole's magnetic field, whence,

$$\frac{mv^2}{2\rho} = qvB \Rightarrow p = qB\rho ,$$ (3.5)

with B the magnetic field strength, q the ion charge state, v the velocity of the ion, and ρ the bending radius. For fixed B and ρ, magnetic dipoles deflect particles on the basis of their magnetic rigidity, p/q, with q the ionic charge state of the particle. Because the recoils and
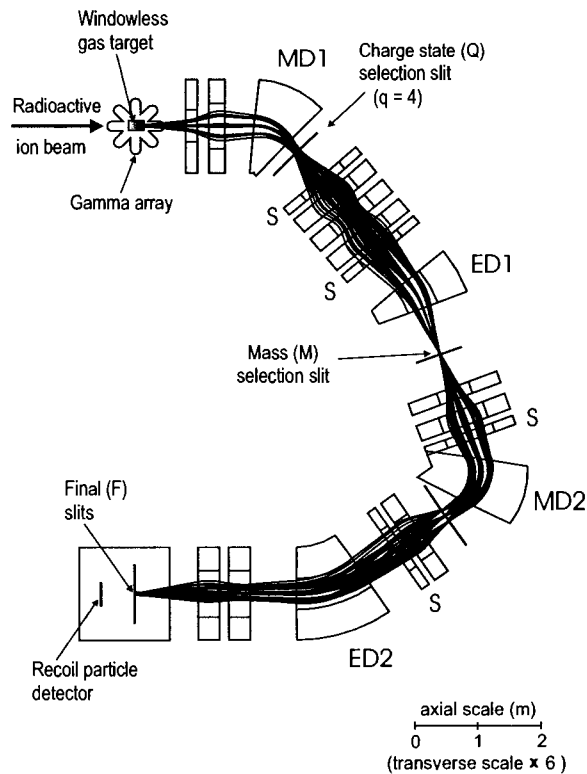
Figure 3.8: Schematic diagram of the DRAGON optics layout highlighting the focusing properties of the mass separator for ^{19}Ne trajectories. The transverse scale has been magnified 6X to display ion trajectories with greater clarity.

beam ions exit the gas target with a distribution of ionic charges, from collisional electron exchange with the H_2 gas, the field of MD1 is chosen to have recoil particles of the charge state of highest probability deflected along the optical axis of the magnet. The slight difference in exiting recoil momentum and beam momentum, as discussed above and implied by equation 3.4, means that beam particles of the selected recoil charge state will also pass through MD1 essentially along the optical axis. Vertical and horizontal slits, located 31 cm downstream of the MD1 pole faces, are adjusted to intercept all other particles; these slits are referred to as the charge slits, and are shown in figure 3.8. Thus, exiting the downstream side of MD1 are recoils and beam ions of a unique and known charge state.

Following the charge slits, a quadrupole triplet with aberration correcting sextupoles

brings the ions to an achromatic focus downstream of the first electrostatic dipole (ED1). It is at this point where mass separation of the fusion recoils from beam takes place, as discussed in what follows. Squaring both sides of equation 3.4 and dividing through on both sides by $2m_r$, with m_r the recoil ion mass, gives,

$$E_r = \frac{m_b}{m_r}E_b \left(1 \pm \frac{2E_\gamma/c}{\sqrt{2m_bE_b}} + \frac{E_\gamma^2/c^2}{2m_bE_b} \right) . \tag{3.6}$$

The first term in the brackets, when multiplied by the expression outside the brackets, is just the central value of the fusion recoil kinetic energy were there no momentum boost from γ-decay. The second term is just twice the momentum spread term of equation 3.4, and is therefore on the order of several percent: this term represents the maximum deviation in the upper and lower limits of the fusion recoil energy from its central value. The last term in the brackets is very small: $O(10^{-4})$, and can be neglected. The first two terms of equation 3.6 show that the fusion recoil kinetic energy will be several percent different from that of the beam. Ions traversing the optical axis of a right cylindrical electrostatic bender will follow a circular trajectory between the electrodes, and thus by Newton's second law:

$$q\mathcal{E} = mv^2/\rho , \tag{3.7}$$

where $\mathcal{E}$ is the electric field along the trajectory, v the ion velocity, and ρ the constant radius of curvature of the trajectory. Therefore, ions with kinetic energies $E = q\mathcal{E}\rho/2$, will traverse the bender along the optical axis. Thus, an electrostatic bender separates particles on the basis of their kinetic energies. For ED1, the voltage on the device is set to allow fusion recoils to pass through along the optical axis. Beam particles, with kinetic energies several percent higher than the fusion recoils, will take trajectories through the bender with larger radii of curvature. Horizontal and vertical slits, located at 105 cm from the end of the ED1 electrodes, on the downstream side of the ED1, unit are adjusted to intercept the beam particles while allowing the recoils to pass through along the optical axis. These slits are referred to as the mass slits, and their location is shown in figure 3.8.

The second stage of DRAGON is essentially a repeat of the first stage, but with an electrostatic dipole with a larger bending radius. As a result beam ions, on reaching ED2, will be deflected on trajectories resulting in displacements from the optical axis such that they impinge on the walls of the beam pipe or can be intercepted by slits at the final focal plane

Table 3.1: Properties of the DRAGON magnetic and electric dipole benders

	MD1	MD2	ED1	ED2
Bending Radius (m)	1.00	0.813	2.00	2.50
Bending Angle	50°	75°	20°	35°
Pole/Electrode Gap (mm)	100	120	100	100
Maximum Field/Voltage	5.9 kG	8.2 kG	± 200 kV	± 160 kV

of the mass separator. Finally, from ED2, the fusion recoils are achromatically focused, by way of a final quadrupole doublet, onto the location of the final slits. In fact, for this work, the final focus was altered to lie at the location of the DSSSD.

Figure 3.8 summarizes the beam transport properties of the DRAGON mass separator. As an example, shown are typical ion trajectories of ^{19}Ne from the ^{15}O$(\alpha,\gamma)^{19}$Ne reaction at $E_{cm} = 504$ keV, originating from a beam spot size of 3 mm diameter: the transverse scale has been scaled by six times to bring out the finer detail of the trajectories. The momentum dispersive focus behind each MD element, and the achromatic focus downstream of each ED element are clearly shown. Finally, figure 3.9 shows a plan view of the interior of a DRAGON electrostatic dipole bender detailing the layout of the titanium electrodes and a typical recoil trajectory through the device; table 3.1 summarizes the physical properties of the dipole benders.

3.2.2 Windowless Gas Target

The DRAGON gas target [49] is comprised of an aluminum cell, quadrangular in shape, with two parallel horizontal sides and two sides equal in length and inclined at 60° to the horizontal; these sides are slanted so that jets of gas exiting the entrance and exit apertures are directed downward, away from the entrances to the tubes of the differential pumping system. The cell has a entrance aperture of 6 mm diameter and an exit aperture of 8 mm diameter; the spatial separation between apertures is 11.0 cm. On the downstream side of the cell are mounted two hollow tubes which extend into the central region of the cell: one tube is mounted at 30° to the beam axis, the other at 57° to the beam axis. These tubes share a common collimator of a composite geometric shape: a 5 × 5 mm^2 square with
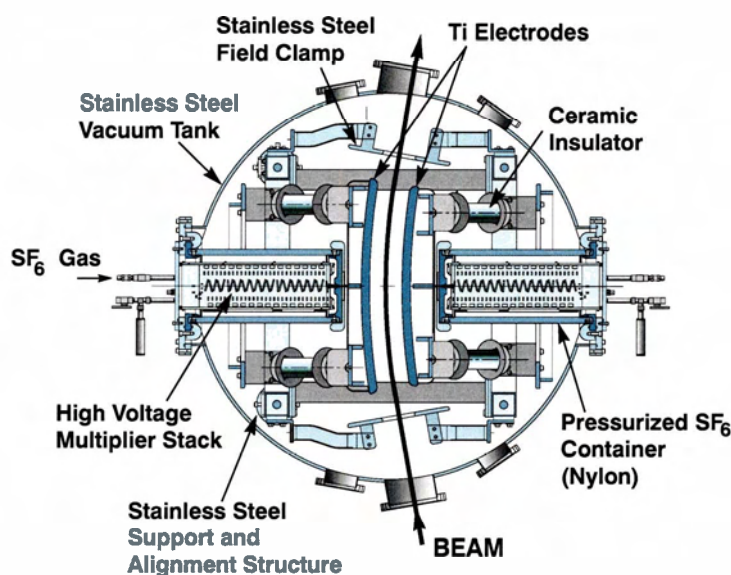
Figure 3.9: Plan view showing the interior construction of the DRAGON electrostatic dipole bender.

semi-circular ends of radii 2.6 mm. This collimator sits 1 cm below the beam axis. At the opposite end of each tube, behind a circular collimator, is mounted an ORTEC Ultra Cam silicon detector of 150 mm^2 area, used for the detection of elastically scattered protons for the determination of total beam on target. The distance from detector face to the common collimator is 7.3 cm for the detector telescope at 57° and 4.7 cm for the detector telescope at 30°. For this work, only the detector at 30° was employed. A capacitance manometer on the opposite slanting face monitored the cell gas pressure. Figure 3.10 shows a detailed elevation view of the target cell thus described.

This cell assembly is mounted as a self-contained unit within a rectangular, aluminum pumping box 17.15 cm wide by 28.3 cm high by 5.0 cm thick, and 3 mm thick walls, schematically shown in figure 3.11. The bottom of the pumping box is connected by a 15 cm diameter pipe to a system of large Roots blowers (two Leybold WSU2001, two WSU501, one WS500), which comprise the first stage of differential pumping. Hydrogen gas exiting the entrance and exit apertures of the cell enters into the pumping box where the first stage of Roots blowers pumps on it, compressing the gas to > 40 Torr at the inlet
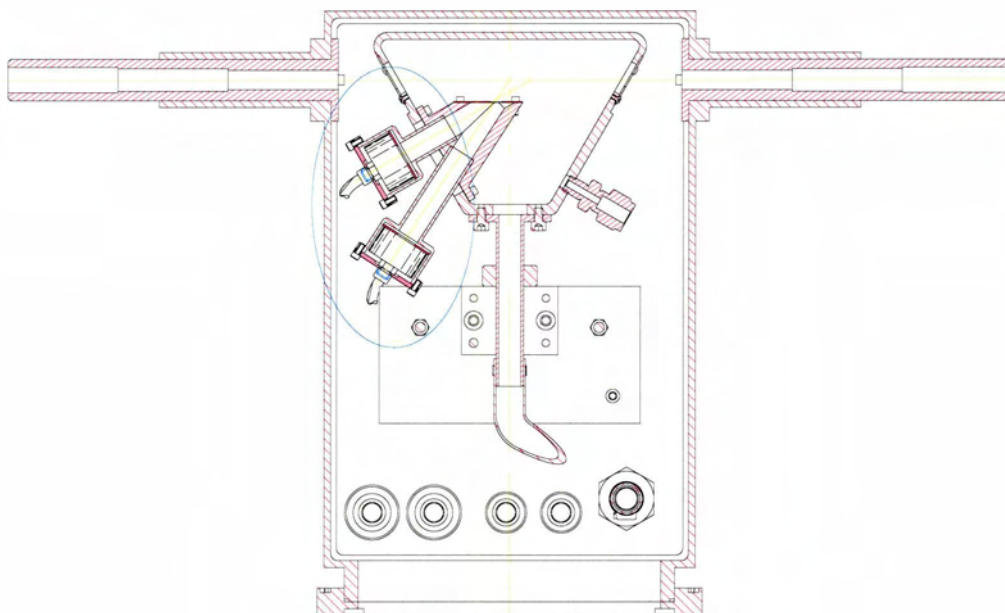
Figure 3.10: Elevation view of the DRAGON gas target cell, showing pumping tubes, elastic monitor telescopes (highlighted by oval) and capacitance manometer opposite to elastics. Shown at bottom are various feedthroughs for electronics connections. Beam enters through the right-hand pumping tube.

to a 20 l cleaning trap containing 2 l of Zeolite molecular sieve held at liquid nitrogen temperature. The sieve adsorbs approximately 50 atm·l of hydrogen when the trap pressure is operating at pressures up to 45 Torr. This reservoir of trapped gas contributes to the operational stability of the pressure within the gas cell, maintaining cell pressures stable at the level of 1% throughout experimental runs with no adjustment of the flow control valve required. An electronically controlled needle valve situated between the gas target cell and the exit of the Zeolite trap was used to adjust the cell gas pressure.

Housed in pumping boxes upstream and downstream of the target box are a series of pumping tubes (figure 3.10), the inner diameters of which are stepped up in size, as one goes further away form the target pumping box, to conform with the expected beam convergence and recoil divergence entering and exiting the target, respectively. Each pumping
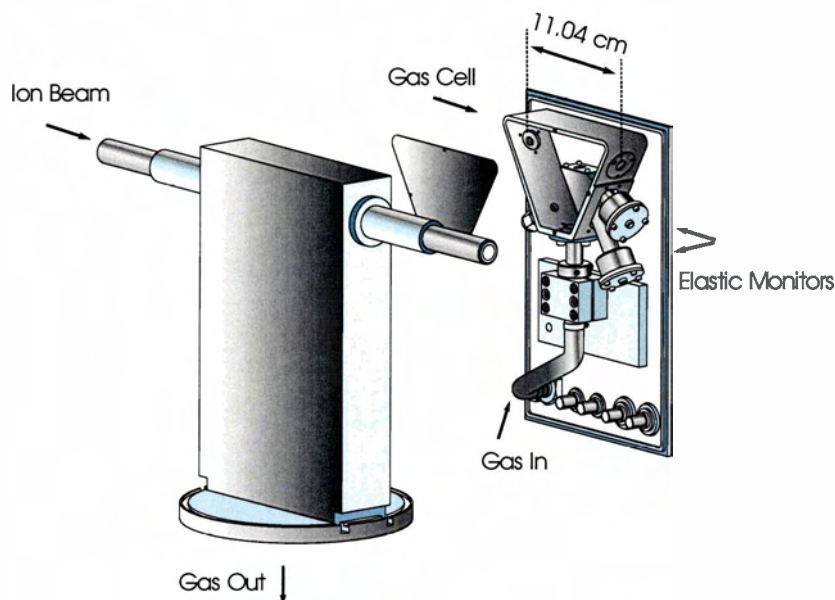
Figure 3.11: Schematic cut-away view of the gas target mounting within the target pumping box.

box has attached to it a $1000\,\mathrm{l\,s^{-1}}$ turbomolecular pump[2] (Varian V1000HT). Hydrogen gas that escapes the gas cell and makes its way down the pumping tubes is removed from the beamline by this series of turbo pumps and delivered to the Roots blower system for recirculation. Operating with a gas cell pressure of 4.5 Torr resulted in nominal pressures of $< 3 \times 10^{-6}$ Torr at the ends of the pumping boxes. The gas temperature in the cell was monitored by a thermocouple and was found to be nominally 300 K. Figure 3.12 schematically shows the gas target pumping and recirculation system and figure 3.13 schematically details the layout of the gas target pumping tubes.

3.2.3 Gamma Detector Array

The DRAGON gas target is surrounded by a γ-detector array [49, 50] comprised of 30 hexagonally shaped crystals of bismuth-germanium oxide (BGO) in a close-packed geom-

---

[2]An exception is the first downstream pumping box which has two of these pumps attached; one above and one below.
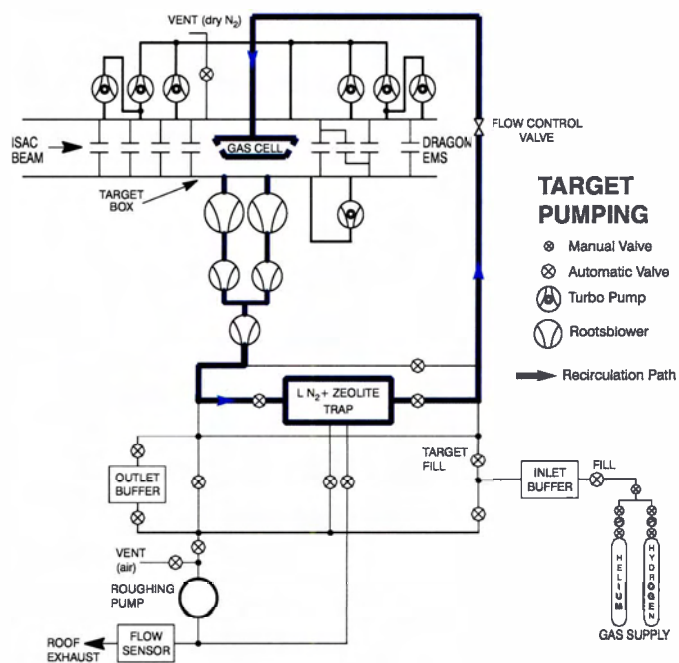
Figure 3.12: Schematic diagram showing the gas target recirculating pumping system.
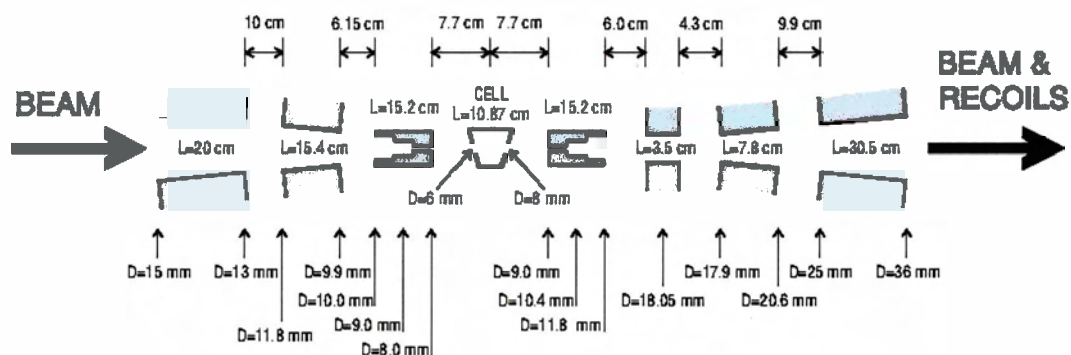
Figure 3.13: Schematic representation detailing the dimensions and relative layout of the DRAGON pumping apertures and tubes.
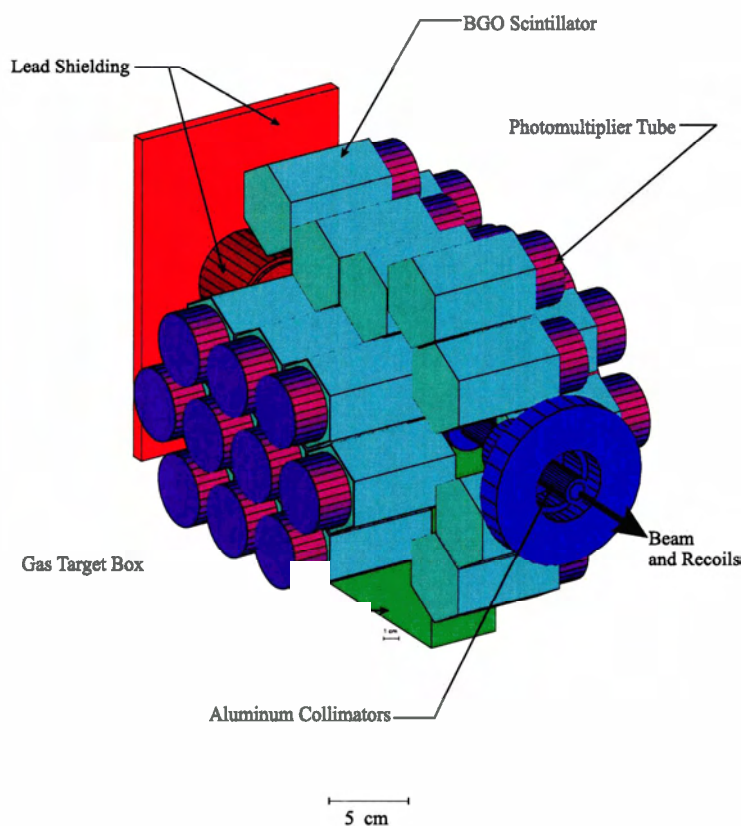
Figure 3.14: Three dimensional view showing the coverage of the γ-array surrounding the gas target pumping box.

etry, as shown in figure 3.14 [50]. BGO is a dense material and, therefore, offers good geometric efficiency for photon detection in a compact volume crystal. Each crystal has a length of 76 mm and the distance between parallel faces on the hexagon is 57.8 mm; these dimensions were chosen to match the photon attenuation length of 50 mm at 5 MeV, which is a typical γ-energy for most DRAGON experiments. Each crystal is coupled to a photo-multiplier tube (PMT) which converts scintillation light in the BGO crystal into a detectable current pulse by way of electron avalanche multiplication. Figure 3.15 schematically shows a typical crystal layout coupled to its corresponding PMT.

Calibration studies of the γ-array using a calibrated 6.13 MeV ^{244}Cm/^{13}C source de-termined the ensemble averaged energy resolution of the array to be 7%, full-width at half-

Gamma Detector Assembly
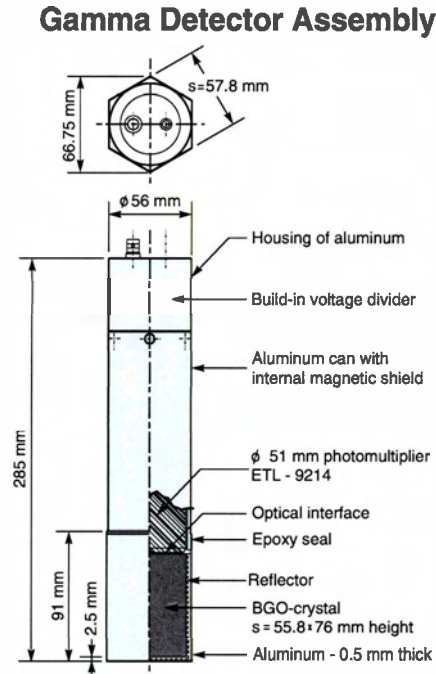
Figure 3.15: Schematic diagram showing one of the γ-array BGO crystals coupled to its photomultiplier tube.

max [49]. Because of a beam induced 511 keV γ-ray background, as a result of positron annihilation, a hardware threshold of 2 MeV was imposed on the signals from each BGO crystal to minimize the dead-time of the array and the data acquisition system. The total solid angle subtended by the array is ≈ 90% of 4π as seen from the centre of the gas cell. The gaps in solid angle coverage occur upstream and downstream of the gas cell by virtue of the pumping tubes, and underneath the target pumping box as a result of the 15 cm diameter pumping tube. For the data in the present work consisting of "coincidence" events, the γ-array served as the start signal for a recoil time of flight clock allowing for detection of fusion recoils in coincidence with the reaction γ-rays.

3.2.4 End Detector

Mounted in the final focal plane of the EMS, perpendicular to the beam axis, was a double sided silicon strip detector (DSSSD), of the $p - n$ junction type, for the detection of the heavy ion recoils. This detector is composed of two segmented layers of detection strips, with the layers' strips oriented orthogonally with respect to each other. Each layer is composed of 16 detection strips of 3 mm pitch and 5 cm length. A gap approximately 110 μm wide of insulator material separates strips in the same layer from each other. A schematic diagram [51] of the detector is shown in figure 3.16.
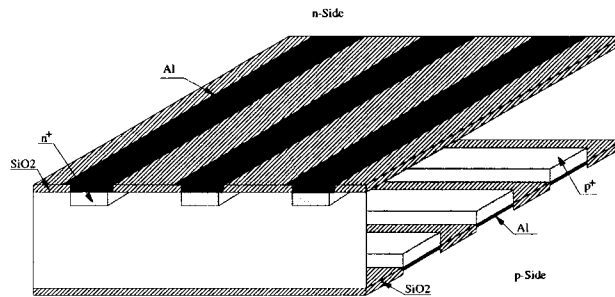
Figure 3.16: An exploded schematic view of the DSSSD showing relative orientation of the detection strips, with gaps shown horizontally hatched. Dimensions not to scale.

The thickness of the strips is large (300 μm) compared to the range of heavy ions (30 μm), leaving the back strips relatively far from the site of charge creation compared to the front strips. This results in a degradation of the energy resolution and a slower timing response of the back strips. Accordingly, energy and timing signals for the coincidence data were taken from the front strips. Because the separator's bending elements (MD's and ED's) are designed to bend the particle trajectories horizontally, the detector was mounted with the front strips vertically oriented, thus providing horizontal position information for optimizing the optics tune of the separator.

3.2.5 Acquisition Hardware and Electronics

Gamma Detector Array Electronics

Each output signal from the 30 γ-array PMTs is carried by 50 Ω coaxial cable to 30 rack-mounted resistive splitters, as schematically shown in figure 3.17 [49] at top left. From the splitter, one output is sent to an ADC through a 128 ns delay-line; the other output is amplified 10×. There are two outputs from the 10× amplifier: one is sent to a leading-edge-discriminator (LED); the other feeds a 8 MHz low-pass filter, which in turn feeds a constant-fraction-discriminator (CFD).
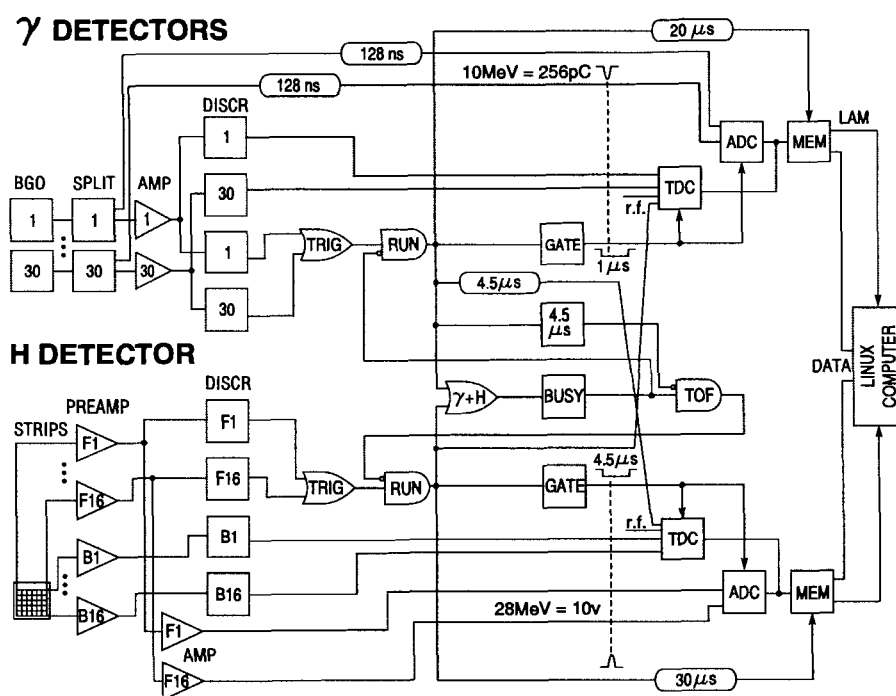
Figure 3.17: Block diagram of the DRAGON data acquisition electronics. Definitions: ADC = Analogue to Digital Converter, AMP = Amplifier, BGO = Bismuth Germinate, DISC = Discriminator, MEM = Memory, TDC = Time to Digital Converter, TRIG = TRIGGER.

The 30 CFD logic signal outputs so produced are combined to create a global logical OR condition to generate a γ master-gate signal. This gate then generates gates, of 1 μs

width, for the γ-array ADCs and the start signals for the γ-array TDCs. Additionally, this master-gate starts a 20 μs busy-gate (BUSY in figure 3.17) which holds off the occurrence of any additional γ or heavy ion events by latching the triggers of both systems. This allows for full signal conversion of the ADCs and TDCs of both systems and transfer of their data into a memory unit.

The trigger (TRIG) of the γ-array electronics marks the start-time of the event and imposes the condition that at least one of the 30 BGO crystals detects a γ-ray with an energy exceeding a hardware energy threshold of ≈ 2 MeV. A delay of 128 ns is imposed on these signals to allow the γ-array master gate (TRIG) to first "gate on" the ADC's, prior to the arrival of the BGO energy signal at the ADC. All 30 ADC channels remain on for the duration of the master-gate to ensure conversion of signals from any other γ-rays in the event, such as those from Compton scattering or decay cascades.

DSSSD Electronics

Signals from the 32 strips of the DSSSD are first processed through RAL108 preamplifiers housed in an aluminum box bolted to the vacuum box containing the DSSSD. The preamplifiers produce shaped pulses with a rise time of a few nanoseconds and a decay time of 50 μs, required for input to shaping amplifiers. These output signals are carried by way of a 22 m long shielded cable bundle to amplifier and discriminator modules housed in a Eurocrate near the gas target.

The 16 discriminator outputs from the front strips are combined to produce a global logical OR condition for the heavy-ion trigger. The OR signal is then passed into a gate generator, producing a logic pulse 4.5 μs in width. This pulse activates the input channel of a peak-sensing ADC for each strip. It also starts a heavy-ion TDC module which eventually receives its stop signal from the γ-array trigger, delayed by 4.5 μs – a time period chosen to be longer than the expected heavy-ion time of flight through the separator. This delay setting guarantees that the heavy-ion TDC module will have a valid conversion for γ coincidence events. In addition, the heavy-ion trigger sends a stop signal to the γ-array TDC module. In this way, time of flight of the recoil particle is measured with respect to the γ-array detecting a reaction photon. Conversion of the heavy-ion TDC marks the event as a "coincidence" event, whereas a non-conversion marks the event as a "singles" event in the data structures. The pattern of heavy-ion TDC data, therefore, provides the information

needed to distinguish coincidence events from singles events in the off-line data analysis.

Elastic Monitor Electronics

The elastic monitor detector is attached to a Canberra 2003B preamplifier, followed by an ORTEC delay line amplifier, and then by a Tennelec TC451 constant fraction timing single channel analyzer (TSCA). The output of the TSCA generates a trigger for the elastic ADC and TDC through a common gate generator with the heavy-ion system. The output of the ORTEC delay line amplifier is converted in a separate ADC channel of the same ADC module used by the heavy-ion system. The ADC address, therefore, distinguishes an elastic event from a heavy-ion event in off-line analysis.

3.2.6   ISAC Energy Calibration

Having MD1 as the first bending element downstream of the gas target provided the means by which to measure the energy of the ^{21}Na beam delivered to DRAGON. Equation 3.5 implies that we can write,

$$\frac{E}{A} = \kappa \left(\frac{qB}{A}\right)^2 , \tag{3.8}$$

where A is the ion mass in atomic mass units, and κ is the MD1 calibration constant to be determined experimentally.

Two measurements of narrow resonance reactions of known resonance energies, using stable beam, were performed to determine the value of κ: ^{21}Ne$(p,\gamma)^{22}$Na at $E_{cm} = 258.6$ keV and ^{20}Ne$(p,\gamma)^{21}$Na at $E_{cm} = 1112.6$ keV [52]. For each reaction the resonance position along the beam axis was made to be centred at $z = 0$ for at least three different target gas pressures and beam energies. Determining that the resonance was occurring at $z = 0$ was done by observing the centroid of the histogram showing the z-coordinate (relative to the gas target centre) of those BGO crystals detecting the reaction γ-ray. With small changes in beam energy, the gas target pressure was adjusted until the centroid of this histogram was $z = 0$, indicating that the resonance was occurring at the gas target centre. For each choice of gas pressure, the magnetic field of MD1 required to centre the beam on the optical axis, as read by an NMR probe, was plotted against the resonance-centring gas target pressure. A linear relationship was observed between these two variables. Applying a

linear fit and extrapolating to zero target gas pressure, where the beam energy would be the known resonance energy, allows for immediate determination of κ. From these two reaction studies it was found that $\kappa = (4.827 \pm 0.003) \times 10^{-4}$ keV/u/(Tesla/u^2). More details of the analysis of this result can be found in the thesis of Sabine Engle [52].

3.2.7 Stable Beam Commissioning

Additional stable beam reaction studies were undertaken to fully commission all systems of the DRAGON facility. Specifically, the stable beam studies were performed in order to determine that measurements done with the facility could accurately, and consistently, reproduce the literature results of resonance strengths and energies of well-known narrow resonance reactions. The reactions chosen spanned a wide range of centre of mass energies and recoil cones to ensure that the limits of recoil transmission through the gas target exit apertures could be fully explored and determined. The results of these studies are summarized in Appendix C, where it can be seen that the agreement with the literature results is excellent in all cases, with the exception of the ^{21}Ne(p,γ)^{22}Na reaction at a centre of mass energy of 258.6 keV; the cause of this is not clear. Having demonstrated that stable beam experiments with the DRAGON facility could accurately and consistently reproduce the literature results gives considerable confidence and validity to the new results of this work. Full details of the stable beam commissioning study and analysis of its results can, again, be found in the thesis of Sabine Engle [52].

From these systems thus described, narrow resonance, thick target yields have been measured for determining the resonance strengths of astrophysical importance in the ^{21}Na(p,γ)^{22}Mg reaction. We turn to the results of these measurements next.

Chapter 4

Analysis & Results

Absolute determination of a resonance strength, $\omega\gamma$, requires measurement of several physical quantities. As shown by equation 2.40, $\omega\gamma$ depends explicitly on the stopping cross section, ε, requiring measurement of this quantity. Obtaining this quantity requires knowing the effective length of gas in the target. Additionally, on transit through the target, fusion recoils (and beam) undergo electronic charge exchanging collisions with the H_2 molecules. The fusion recoils exiting the target are, therefore, not of a single charge state. Instead, recoils exit the target populating a distribution of charge states: only one charge state, for fixed field strength in MD1, can be accepted for transmission through DRAGON. Thus, knowledge of the recoil charge state distribution is necessary for obtaining an absolute measurement of thick target yield and, therefore, $\omega\gamma$. For data taken in coincidence mode, knowledge of the γ-array detection efficiency is also required for an absolute determination of thick target yield.

This chapter first discusses the essential features of tuning the DRAGON mass separator. Following this, the concept of an "effective target length" necessary for determining the stopping cross section will be presented. Recoil charge state fractions; γ-energy dependent γ-array efficiencies; and beam normalization method – all vital for determining $\omega\gamma$ – will also be discussed. Analysis of the thick target yield curve for the 212 keV state follows, with arrival at the measured resonance strength for this state. No yield events were observed for the 335 keV state: a limit on its contribution to the explosive thermonuclear reaction rate is derived. The chapter will conclude with a discussion of the new resonant rate for the $^{21}Na(p,\gamma)^{22}Mg$ reaction and its implications on ^{22}Na production in ONe novae.

4.1 DRAGON Tuning

Delivery and quality of the ^{21}Na beam to the upstream entrance of the DRAGON gas target pumping boxes was the exclusive responsibility of the ISAC operations group. Particle transport post DRAGON gas target was the exclusive responsibility of DRAGON experimenters.

The ISAC beam energy was determined by DRAGON experimenters using MD1 in an iterative procedure now described. With gas removed from the target, the fields of the first two quadrupole magnets Q1 and Q2 and MD1 were scaled to the nominal magnetic rigidity required for particle transport on the basis of the beam energy as reported by ISAC operations. The vertical charge slits immediately downstream of MD1 were closed down to produce a vertical slit opening of 2 mm and the field of MD1 was adjusted until both slits registered equal currents, thereby indicating passage of the particles along the optical axis at the location of the slits. At this point, Q1 and Q2 were then switched off and the deflection of the beam off-axis was measured by scanning the vertical slits left/right, maintaining 2 mm aperture size, until both slits registered equal current readings; similarly for the horizontal slits. If it was found that the location of the beam with Q1 and Q2 turned off was less than 3 mm in the vertical and horizontal directions, both quadrupoles were powered on and the location of the beam with Q1 and Q2 on was determined using the charge slits. If, at this point, the beam position with Q1 and Q2 on was also less than 3 mm in both horizontal and vertical directions, it was accepted as "good beam" and preparations were made to begin a new experimental run. If the beam position deviated outside 3 mm at any stage of this procedure, ISAC operations was contacted to fine tune the x-y steering of the beam prior to its entrance in the gas target, and the above procedure of beam location with Q1 and Q2 on and off was repeated until such time that off-axis deflection of the beam, with Q1, Q2 off, was less than 3 mm in vertical and horizontal directions. This iterative method was straightforward and ensured that the angular steering of the beam through the gas target was less than 1 mrad from on-axis. With beam centred on-axis at the charge slits, the field of MD1, as determined by an NMR probe, was measured and the beam energy was determined by way of the calibration results discussed in § 3.2.6. These operations were facilitated via computer control interface employing the EPICS[1] software architecture

---

[1]See http://www.aps.anl.gov/epics/about.php for more information on EPICS.

customized for TRIUMF controls systems [53].

Having determined the beam energy, hydrogen gas was admitted into the target and the energy of the beam after gas was determined by measuring the MD1 field that put the beam on-axis at the location of the charge slits. At this point, the remaining optics elements downstream of MD1 were scaled for this energy, particle mass, and charge state, using the EPICS interface. From this point, transport of the beam to the final focus typically involved using x-y magnetic steerers and small fine tuning changes to the fields of ED1, ED2 and MD2. These small corrections were facilitated by diagnostic instruments that could be inserted into the path of the beam to determine its position relative to the beam axis; such as the mass slits downstream of ED1 and so-called beam centring monitors located immediately upstream of ED1, and immediately upstream and downstream of MD2 and ED2. Final focus slits, approximately 50 cm upstream of the DSSSD and x-y steerers downstream of ED2, were employed for ensuring that the beam was on-axis at the location of the DSSSD[2]. From this point, setting the separator tune for accepting ^{22}Mg fusion recoils was a simple matter of scaling the electric potentials on ED1 and ED2 by the ratio of recoil mass to beam mass; namely, m_{21}/m_{22}. Being the first ever measurements on DRAGON of heretofore unknown resonance strengths, a conservative approach was taken with regard to the mass and charge slit settings. The vertical and horizontal charge slits were set to 25 mm openings, as were the horizontal mass slits; the vertical mass slits were set to 15 mm and the final focus slits were always set fully open at 45 mm horizontally and vertically. These slit settings were chosen to ensure full recoil transmission through the separator. Stable beam studies [52] using a ^{21}Ne beam at 200 keV/u and a magnetic steerer in place of the gas target, to simulate recoil cone angular deflections, showed that these slit settings would not interfere with ^{22}Mg recoil transmission through the separator.

4.2 Effective Target Length

For a narrow resonance ($\Gamma \ll \Delta$), the positional dependence of where the reaction takes place in the gas target is essentially that of a δ-function. Moreover, ε is reasonably invari-

---

[2]The position sensitive DSSSD could not be used for this purpose as exposure of it to full intensity beam would destroy it. A Faraday cup, located between the final slits and the DSSSD, was inserted during this stage of tuning.

ant with respect to density/pressure changes within the gas target (equation 2.36) and so specific knowledge of how the gas density varies along the target length is not of importance for narrow resonance thick target yields. Lastly, to first order, for low energy ions ε is a constant when the total energy loss is a small fraction of the total energy. These three aspects motivate the concept of an effective target length for the DRAGON gas target.

Owing to the presence of the target entrance and exit apertures, H_2 gas extends outside each end of the cell and, therefore, creates a density gradient along z; with low, falling pressure outside the apertures and a density plateau in the cell. For the reasons stated above, ε will be the same for this extended target as for a target with a gas density distribution comprised of a step-function of height normalized to the internal pressure of the gas cell. The width of this step-function defines the effective target length. Once the effective length of the DRAGON gas cell has been determined, ε can then be determined, for any beam energy, from measurements of the beam energy loss through the target.

The target cell gas density profile (density as a function of z) was measured [52] from γ-ray yields from a non-resonant energy region of the $^{15}N(p,\alpha\gamma)^{12}C$ reaction at a ^{15}N beam energy of 1.45 MeV/u. In the non-resonant region, the reaction γ-yield is proportional to the target density. The measurement revealed that the gas density profile had a full-width at half-pressure of 10.8 ± 0.6 cm; commensurate with the geometrical cell length of 11.0 cm. In addition to the gas thickness in the target cell, there is also a component of thickness created by that gas which leaks out of the cell apertures into the target pumping box and into the target pumping tubes. Attempts to measure the thickness of this component of the gas outside the cell were hampered by beam-induced γ-backgrounds [52], which ultimately prevented a determination of the total gas thickness.

To overcome this difficulty, the gas cell was modified by installing entrance and exit apertures 1.5 mm in diameter each; reducing the total aperture area to just 4.5% of the original set-up. The salient argument of this approach is that, with such small areal openings, the H_2 density profile becomes asymptotically close to that of a step-function of effective length 11.0 cm. A beam of ^{21}Ne at 275 keV/u was passed through the target and its outgoing energy, at different gas pressures, was measured using MD1. This series of measurements was also repeated under the same conditions, but with the original apertures installed. A linear relationship of the form,

$$\Delta E = \xi P,$$

was found for both small and standard aperture configurations; where E is in keV/u, ξ is the slope of the line and P the target pressure, in Torr. The energy loss, ΔE, is proportional to the effective length, L, of the target. Therefore, at a *particular* pressure, we can relate,

$$\frac{\Delta E_l}{\Delta E_s} = \frac{\xi_l}{\xi_s} = \frac{L_l}{L_s},$$

where the subscripts "s" and "l" denote "small" and "large" aperture configurations, respectively. The measured slopes of $\xi_l = -3.12 \pm 0.05$ keV/u and $\xi_s = -2.82 \pm 0.05$ keV/u result in an effective length of $L_l = 12.3 \pm 0.5$ cm [52] of the DRAGON H_2 target.

4.3 Recoil Charge State Distribution

Ions traversing the gas target will experience electronic charge exchanging collisions with the gas molecules. For a gas target of sufficient thickness (density, length, or combination of the two), the ions will exit the target populating an equilibrium charge state distribution. This equilibrium distribution is reached once the gas target thickness is greater than, or equal to, a minimum thickness, x_c, called the "critical thickness". The critical thickness is defined to be when *all* charge states in the distribution are within 5% of their equilibrium charge state values [54, 55]. Knowledge of the critical thickness is required to ensure that the experiment is operated with a target gas pressure sufficient to guarantee recoil charge state equilibrium. Knowing the equilibrium charge state distribution is essential for choosing the recoil charge state of highest probability its transmission and its transport efficiency through MD1. Studies of these distributions for various ion beams, beam energies, and gas target pressures were carried out [54, 55] at DRAGON and at the NABONA Tandem accelerator facility in Naples.

The equilibrium charge state distributions of ^{24}Mg were measured at beam energies of 200, 500 and 800 keV/u for target pressures up to ≈ 5 Torr. The ^{24}Mg beam was passed through the hydrogen gas target, with thickness greater than x_c to ensure equilibrium, and a particular exiting beam charge state was selected on by an appropriate field setting of MD1. Comparison of absolute beam current readings between a Faraday cup (FC) upstream of the target to that of a FC located just aft of the charge slits gave a measurement of that particular charge state fraction. This procedure was then repeated for all other charge states by scanning through the appropriate fields in MD1 and comparing FC readings in the same

Table 4.1: Summary of measured ^{24}Mg equilibrium charge states, charge state fractions, critical thickness and critical pressures.

Incident Energy (keV/u)	q^*	F_{q^*}	x_c (10^{16} atoms cm^{-2})	P_c (Torr)
200	4^+	48.72 ± 0.94	13.2	0.165
500	6^+	30.45 ± 0.76	71.5	0.897
500	7^+	40.81 ± 0.85	71.5	0.897

manner just described. From this study it was found that the charge state, $\bar{q}$, of highest probability is given by an empirical relation of the form [54, 55],

$$\bar{q} = Z_p \times \left[1 - \exp\left(-\frac{A}{Z_p^{\gamma}} \sqrt{\frac{v}{v'}} + B \right) \right] , \tag{4.1}$$

where Z_p is the projectile atomic number, v the projectile velocity, $v' = 3.6 \times 10^6$ m/s, and A, B and γ are free parameters that were fitted to the charge state data, resulting in: $A = 1.421$, $B = 0.4495$ and $\gamma = 0.44515$ for H_2 gas. This formula allows calculation of the charge state of highest probability for recoil ions with energies outside the energy range of previous charge state studies. It was found from the study of Liu [54, 55] that the equilibrium charge state distributions could be fit well by a Gaussian profile parameterized by a mean charge state given by $\bar{q}$ in expression 4.1 and an approximate width, d, characterized by $d = d_1 Z_p^w$ with $d_1 = 0.23675$ and $w = 0.54772$. That the equilibrium charge state distribution can be characterized in this simple manner allows for prediction of the expected equilibrium charge state of highest probability and its charge state fraction. In practice, it is found that the distribution width is better determined by interpolation between previously determined experimental data values of width versus charge state for a given ion species [54, 55].

Table 4.1 summarizes the results of the charge state study experiments showing the optimal charge state, q^*, the charge state fraction, F_{q^*}, of q^*, the critical thickness to achieve equilibrium, and the corresponding target pressure, P_c, that the critical thickness corresponds to.

For this work, all ^{22}Mg recoils exit the gas target with lab energies ≤ 360 keV/u, and target gas pressures were ≥ 4.6 Torr, with the exception of one run taken at 2.5 Torr. From

the ideal gas law, the target thickness can be calculated as,

$$x = 6.28 \times 10^{16} \ L(\text{cm})P(\text{Torr}) \ [\text{atoms/cm}^2] \ .$$ (4.2)

From this expression, the minimum length of hydrogen gas required to achieve equilibrium at 200 and 500 keV/u can be calculated. Substitution of the x_c value for $E_{\text{lab}} = 200$ keV/u, from table 4.1, into the right side of this expression results in: $L_{200} = 0.44$ mm at 4.6 Torr and $L_{200} = 0.8$ cm at 2.5 Torr. From these numbers it can be concluded that charge state equilibrium for ^{22}Mg recoils from the reaction study of the 212 keV state is assured for all beam energies used, as will be seen in § 4.6. The data for the 335 keV state were taken at a nominal gas target pressure of 8 Torr. This beam energy was such that the position of the resonance was close to the target centre, ensuring charge state equilibrium of any exiting recoils.

4.4 Gamma Detector Array Efficiency

The γ-array was essential for the results of the present work. While DRAGON was designed to have high beam suppression, in practice it was found that, at the low beam energies associated with this work, a small fraction of beam ions were able to make their way through the separator to the DSSSD. These events will be referred to as "leaky beam" henceforth. Figure 4.1 shows a plot of the leaky beam energy peak (black histogram) as recorded by the DSSSD for a single run at 220 keV/u beam energy. Given that equation 3.6 indicates that ^{22}Mg recoil energies are, to first order, $21/22 = 5\%$ reduced over that of the beam energy, it is clear from figure 4.1 that recoils (red) will be buried in the low energy tail of the leaky beam peak. It was, therefore, necessary to use the γ-array in coincidence with the DSSSD to suppress the leaky beam events and extract the ^{22}Mg recoils from the data.

The efficiency response of the γ-array was modeled using the GEANT simulation software, and is the subject of another graduate study [56]. The model incorporated the geometrical configuration of the array; gas target pumping box; gas target cell, and all materials comprising the target cell and pumping box, including the physics effects of gamma rays traversing those materials. Within the simulation[3], an isotropic point source of γ-rays was

---

[3]These simulations were kindly performed by Dario Gigliotti.
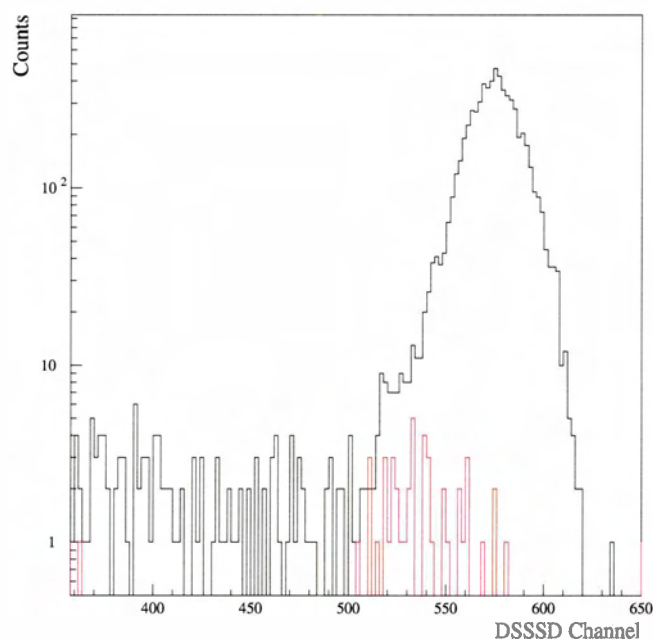
Figure 4.1: Plot showing the large "leaky" ^{21}Na beam peak and its low energy tail (black) for a single run at 220 keV/u. Superimposed are ^{22}Mg recoil candidates (red) for all runs at 220 keV/u.

positioned along the beam axis, starting at $z = -21.0$ cm (upstream of gas target centre) and was stepped along the beam axis in increments of 2 cm. At each of these positions, the simulated source emitted γ-rays with energies characteristic of the *gamma*-decay schemes [57] of the 212 and 335 keV states. A diagram showing the decay schemes of these two states is shown in figure 4.2. In this way, the efficiency response of the γ-array was constructed for each branch of the two cascades of the 212 and 335 keV states. The total efficiency response of the array, for each state's cascade, was determined by taking the branching ratio weighted average of the individual branch response curves, and applying a simultaneous cut on the detected γ-energy of $E_\gamma \geq 3$ MeV. The total efficiency response curves thus constructed are shown in figure 4.3, and it is from these curves that the analysis of these data derives its γ-efficiencies.
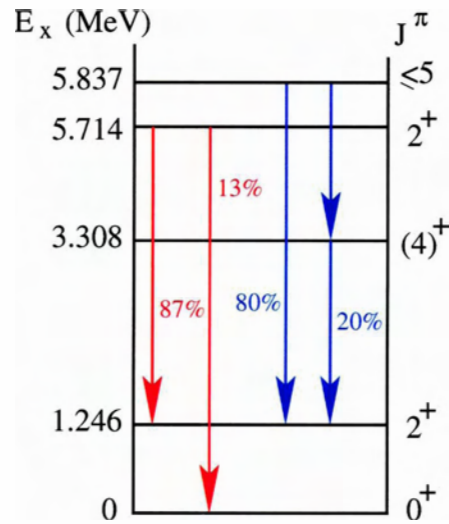
Figure 4.2: Gamma cascade schemes of the $E_{cm} = 212$ keV state ($E_x = 5.714$ MeV) and of the $E_{cm} = 335$ keV state ($E_x = 5.837$ MeV), with branching ratios and adopted spins shown.

4.5 Normalized Integrated Beam on Target

Integrated ^{21}Na beam on target, for each beam energy, was determined from spectra obtained from the elastic monitor, mounted at 30 degrees, in the gas target. The elastic monitor, viewing a path length of H_2 gas through which the beam particles pass, makes a natural beam rate monitor and integrator by way of its detection of elastically scattered protons. Once the total number of Rutherford scattered protons within a run is determined, they must be normalized to the initial rate of beam on the target at the beginning of the run for the total beam on target to be determined. The following sections discuss how these were done.

4.5.1 Integrated Elastic Protons

Figure 4.4 shows a typical elastic monitor pulseheight spectrum; the proton peak is clearly evident, as is an underlying background caused by the passage of positrons through the detector from the β-decay of "spilled" ^{21}Na on the upstream pumping apertures. Determi-
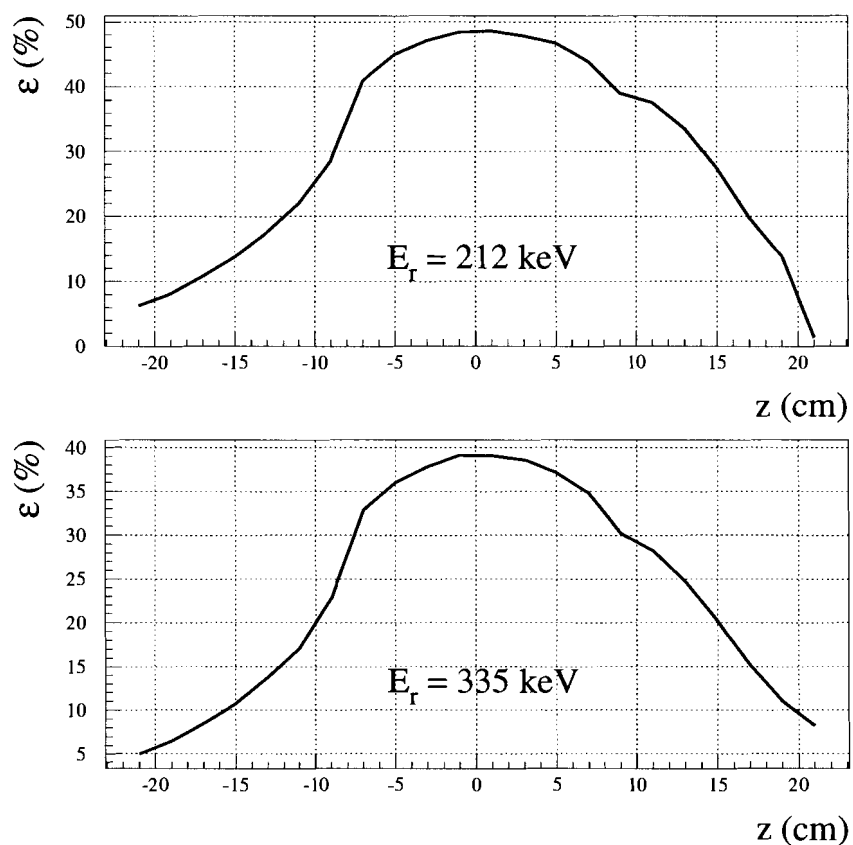
Figure 4.3: The γ-array total efficiency response, ε, at 3 MeV threshold, for an isotropic point source as a function of position along the beam axis as determined by GEANT. Top panel: the response for γ-rays from the cascade of the state at 212 keV. Bottom panel: the response for γ-rays from the cascade of the state at 335 keV.

nation of the total number of Rutherford scattered protons within a given run was a matter of finding a means by which to subtract off the positron background from spectra such as figure 4.4. The pulsed time structure of the beam provided a natural means by which to do this.

Shown in figure 4.5, in the top panel, is a two dimensional histogram of the correlation
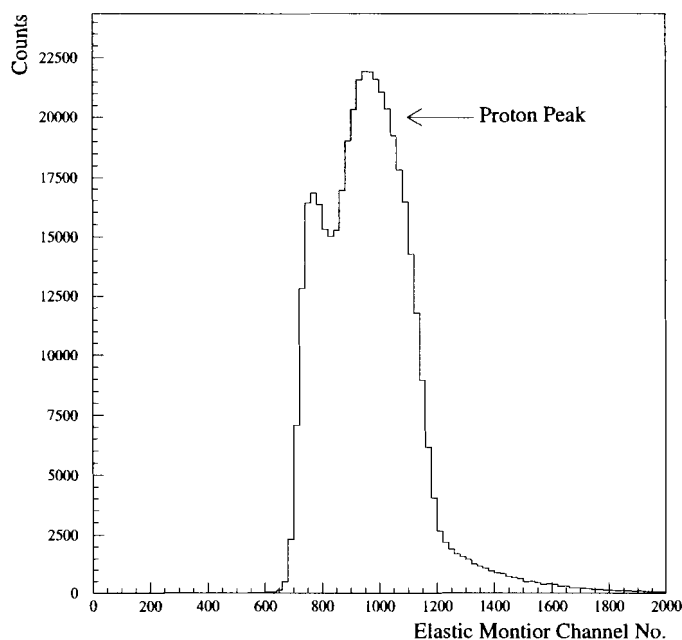
Figure 4.4: Typical elastic monitor pulseheight spectrum for elastically scattered protons at a ^{21}Na beam energy of 220 keV/u. The proton peak shows prominently, superimposed on a background positron events.

between elastic monitor pulseheights within the 85 ns timing window of the ISAC accelerators. Prominent in the top panel of the figure are the high density events centred around channel 1000 in elastic monitor channel, and at channels 340 up through 360 and 200 up through 220 in RF time. These events are the elastically scattered proton events correlated in time, as they should be, with the beam pulse. The lower panel of figure 4.5 shows a projection of events in the top panel onto the RF time axis. Clearly seen, at each end of the RF window, is the elastic proton peak[4]. Also observable is the positron background, which is uniformly distributed in time with respect to beam pulses. Because these positron events are not correlated with the beam pulses, a slice in RF time can be made in the location of

---

[4]The fact these events "wrap around" the RF time window is simply an artifact of an arbitrary timing offset, relative to the accelerator RF signal, caused by signal cables.
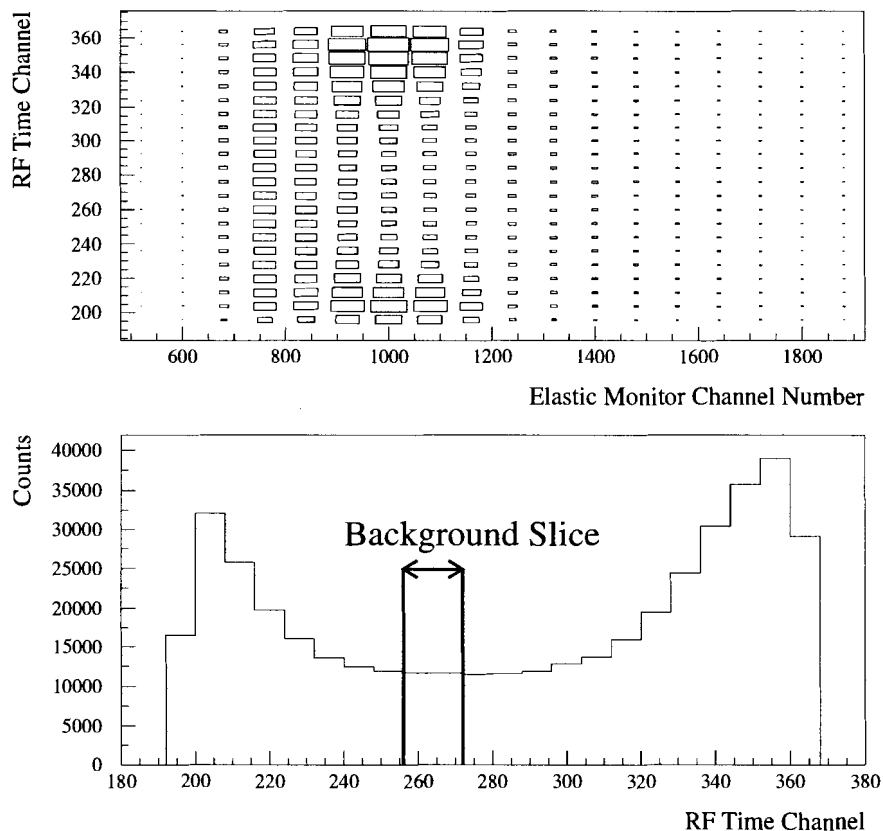
Figure 4.5: Correlation of elastic monitor events with ISAC accelerator RF time. Top panel: two dimensional plot of elastic pulseheights versus the RF time of ISAC accelerators. Bottom panel: projection onto RF time axis of top panel showing the uniformly distributed β-background. Larger rectangles denote higher density of events.

the minimum of the lower panel plot to determine the total number of background events; the so-called "background slice", as shown.

The procedure for obtaining the total positron background was relatively straightforward. The region within the background slice of figure 4.5 was chosen to contain 16 channels. The total number of counts within these channels was determined using the PAW [58]

analysis software. The total RF time window contains 170 channels of 0.5 ns width. Thus, the total positron background is obtained by scaling the counts within the background slice by 175/16. The total number of elastically scattered protons is just the total number of counts in the spectrum minus the scaled counts in the background slice. To ensure that the counts within this slice were purely positrons, the counts within 8 RF time channels to the left and to the right of the slice window were summed and this sum was checked for its agreement, within $\sqrt{N}$, of that of the slice window. This method will be referred to as the "RF background subtraction method" henceforth.

Unfortunately, it was not possible to use this method for all runs within the $E_{cm} = 212$ keV reaction study. Between the experimental runs of Nov. 2001 and Jan. 2002, the original elastic monitor detector was replaced with a new one. The new detector had very poor timing characteristics, and it was found that no time slices within the RF timing window could be found without proton events within them. An alternative method of determining the total number of scattered protons had to be found. Figure 4.6 shows the same elastic proton spectrum as that of figure 4.5 plotted with a logarithmic scale along the vertical axis. Evident in the structure of the spectrum is that the positron background under the proton peak has an exponential shape. The tail of the background, beyond the proton peak, can be fit with a simple exponential function, as shown by the black points. The sloping red line is an extrapolation of the fit back to the low energy edge of the proton peak. Extracting the total number of protons in the run was a matter of subtracting off the integral of the fit function, within the limits of the red vertical lines, from that of the total number of counts contained within the spectrum between the red lines. This method will be referred to as the "exponential fit method" henceforth.

The results of both of these methods, for the two reaction studies at $E_{cm} = 212,\ 335$ keV, are shown in table B.1, and B.2 of Appendix B, with each table summarizing the extracted protons from each run. As a check on the consistency of the two methods, those runs in which the RF background subtraction method was used were also analyzed with the exponential fitting method to compare the consistency between the two methods. The results of table B.1 show that, at the level of a few percent, the agreement between the two methods is excellent.
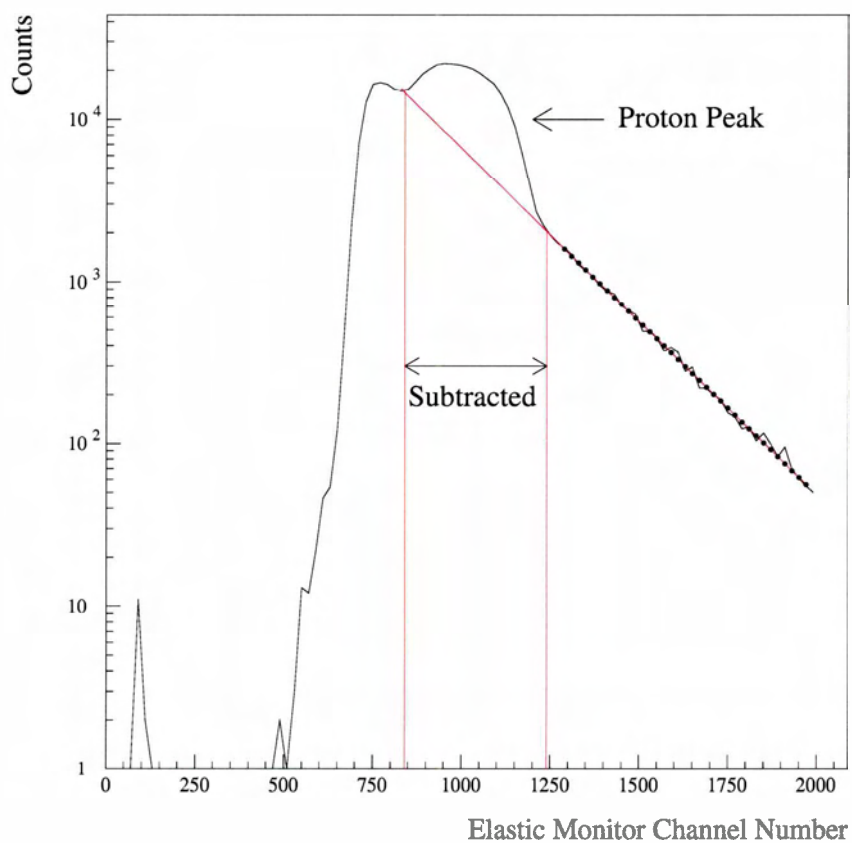
Figure 4.6: Elastic proton pulseheight spectrum showing the method of positron background subtraction.

4.5.2 Beam Normalization

Having obtained the total number of elastically scatted protons for each experimental run, a relationship must be derived to relate that lump sum value to how many ^{21}Na ions actually passed through the hydrogen gas target. If the beam current is constant for a particular time window, and the number of elastically scattered protons for this same time window are determined, then the absolute normalization factor, R, that relates incident beam particles

to number of scattered protons is given by,

$$R = \frac{I/q}{e} \frac{\Delta t}{N_{\mathrm{p}} E_{\mathrm{beam}}^2 / P} \, , \qquad (4.3)$$

where Δt is the time window of constant beam, N_{p} is the number of elastically scattered protons within the Δt time window, I is the incident beam current, q is the charge state of the beam ions, E_{beam} is the incident beam energy, P is the hydrogen gas pressure, and $e = 1.602 \times 10^{-19}$ C is the fundamental unit of charge. The energy-squared and pressure factors enter this expression because the elastic Rutherford scattering cross section varies in direct proportion to pressure and inversely squared as as the incident beam energy. This scaling makes the normalization factors invariant with respect to chosen target pressure and beam energy. The beam current defined by expression 4.3 was measured immediately prior to the start of each experimental run using a Faraday cup located ≈ 2 m upstream of the gas target on the ISAC beamline.

Figure 4.7 shows an elastic monitor rate spectrum, with the time axis being in units of seconds of actual run time, with $t = 0$ the beginning of the experimental run as logged by the data acquisition computer clock. The top panel of the figure shows that the rate of events in the monitor appears constant out to 5000 s; the lower panel is a plot of the same data out to ≈ 500 s to reveal some of the finer details of the spectrum. The figure suggests that a time window exists in which the beam rate is constant. However, it is important to realize that the counts contained within each bin of the spectrum are a sum of elastically scattered proton events and positron events. Verification that the *beam rate* within the time window was actually constant was done by employing the following method. Firstly, a time window, Δt, was chosen, with $t = 0$ at the beginning of the run, such that the elastic monitor rate appeared constant, as shown already in figure 4.7. Next the time window, Δt, was then subdivided into three equal time intervals, $\Delta t/3$, and the number of protons within each of these three subintervals was extracted by way of the RF background subtraction method previously discussed. If the number of protons within each subinterval agreed with each other, within $\pm 1.5\sqrt{N}$, the total Δt time window was regarded as having constant beam and a normalization value based on equation 4.3 was derived for that run. If the number of protons within the three subintervals did not agree, then another attempt was made using a new Δt time window of shorter duration until statistical agreement of the number of protons in each time subinterval ($\Delta t/3$) was found. Not all runs yielded to this method; some had
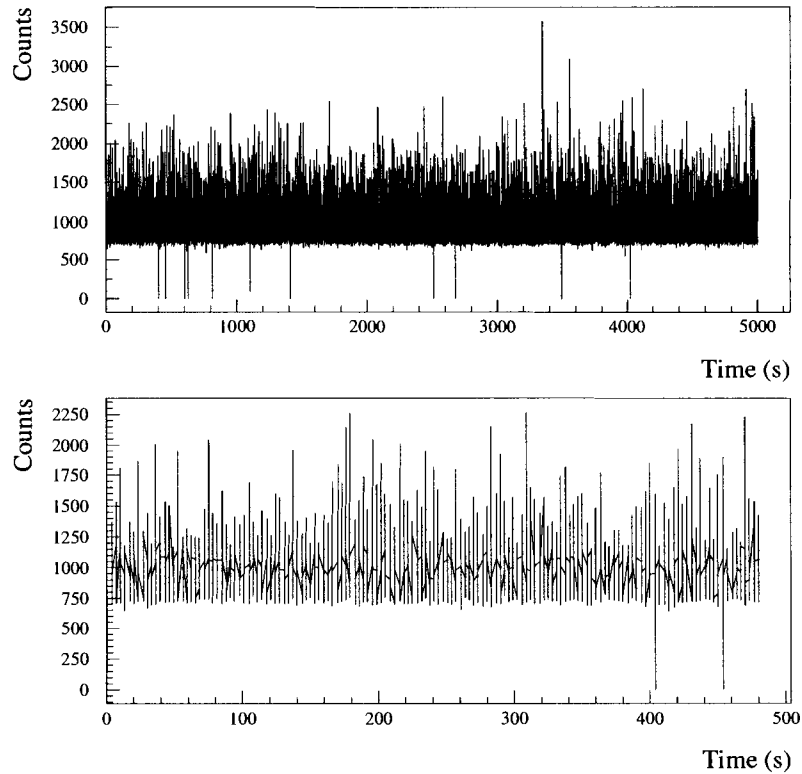
Figure 4.7: Typical rate spectrum from the elastic monitor from an experimental run. Top panel: constant elastic monitor rate out to $t = 5000$ s. Bottom panel: same as top, out to $t \approx 500$ s showing finer detail.

very unstable beam initially, preventing a normalization to the initial beam current, I.

Once this method verified that a constant appearing elastic rate spectrum does imply a constant beam, some of the runs that had poor elastic monitor timing were also used to generate R normalization values with. A time window was found in which the elastic rate spectrum appeared constant, and a pulseheight spectrum, analogous to that of figure 4.6 was produced from just those elastic monitor events within the time window of constant beam. This spectrum was fit with the exponential method to extract the number of protons for use in equation 4.3. Table B.3 summarizes the normalization values thus obtained and figure 4.8
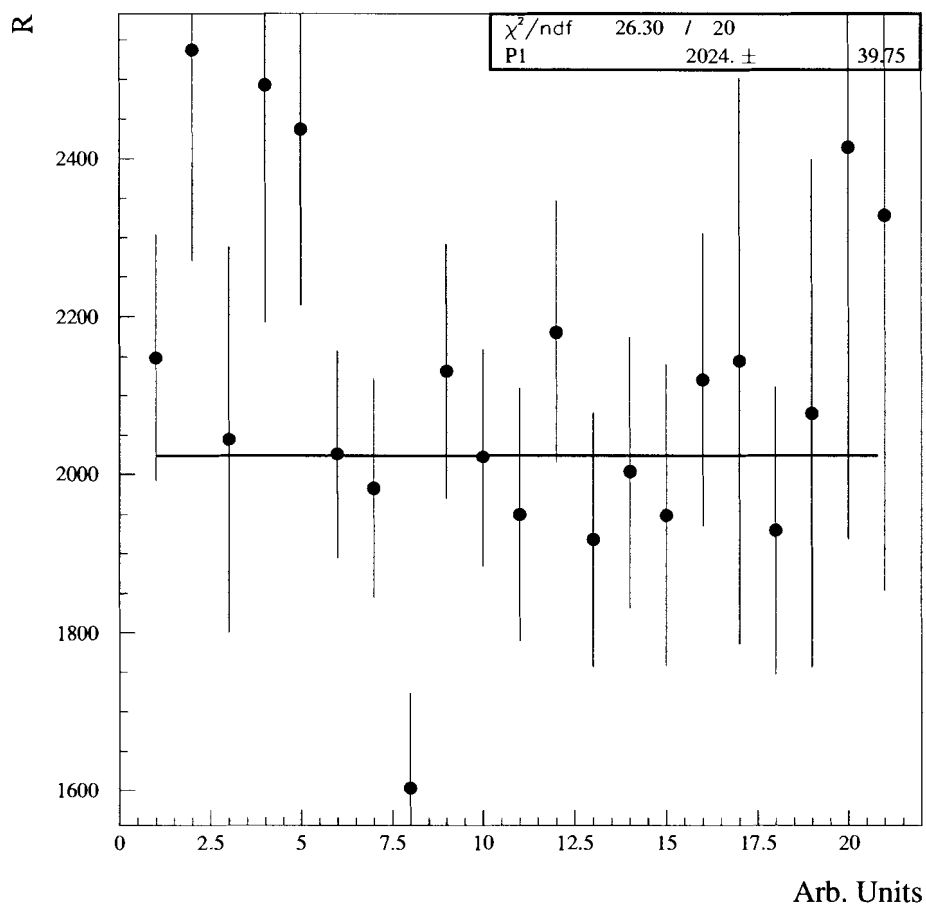
Figure 4.8: Plot of the beam normalization factors with result of the fit shown.

shows a plot of the dead-time corrected normalizations with a horizontal fit through them.

The five high datum points were obtained by the exponential fit method to a time window in which the elastic monitor rate appeared constant and span the range of beam energy from ≈ 212 keV/u, for the points in the top left, up to 360 keV/u for the two points in the top right corner. On the other hand, three other normalization factors obtained using the exponential fit method agree well with the mean result, so the exponential fit method cannot

Table 4.2: Summary of the integrated ^{21}Na beam on target for each beam energy used in this work.

Integrated ^{21}Na Beam on Target	
Energy (keV/u)	Integrated Beam ($\times 10^{12}$)
210.8	11.30(34)
211.9	7.35(18)
213.5	3.51(11)
214.3	9.37(22)
214.9	12.24(29)
215.0	15.59(38)
220.0	35.67(79)
225.1	25.55(61)
230.8	2.072(26)
360.0	9.14(10)

be the sole reason for why those points are outliers. The beam normalization factor thus obtained is,

$$R = (2.024 \pm 0.040) \times 10^3 \; ^{21}\text{Na} \cdot \text{Torr}/\{\text{proton} \cdot (\text{keV/u})^2\}.$$

The dominant contributer to the individual error bars in figure 4.8 is the uncertainty of the Faraday cup reading of the initial beam current: fluctuations of ± 10 electrical particle picoamperes on current readings ≈ 200 electrical particle picoamperes were common for the low beam currents of this study. Table 4.2 summarizes the integrated beam on target obtained for all beam energies associated with this work.

The results of table 4.2 and the previous discussions on the various efficiencies of the DRAGON system have finally put us in the situation of being able to determine thick target yield. All that remains is to determine the number of fusion recoil events produced at each beam energy.

4.6 ^{21}Na(p,γ)^{22}Mg Reaction at $E_{cm} = 212$ keV

The yield experiment for the ^{21}Na(p,γ)^{22}Mg reaction at $E_{cm} = 212$ keV began with taking beam from the ISAC accelerators at an energy[5] of 230.8 keV/u, with the gas target pressure nominally set to 4.6 Torr. After taking $\approx 9 \times 10^{12}$ ^{21}Na ions on target, there were no coincidence events observed between the γ-array and the DSSSD. A ≈ 5 keV/u change in beam energy, downward, was made to $E_{beam} = 225.1$ keV/u and, after running for several hours, γ-recoil coincidence events for this reaction were conclusively observed for the first time – ever.

In total, data were taken at beam energies ranging from 230.8 keV/u down to 210.8 keV/u. The experimental procedure involved starting at the high beam energy of 230.8 keV/u and moving down in approximately 5 keV/u decrements after obtaining sufficient recoil co-incidence data for a given beam energy. In the first round of the experiment, five data points were determined: three of which were on-resonance and two that were off-resonance, and a rudimentary yield curve was obtained. One of these initial data points conclusively showed yield for a beam energy of 215 keV/u, implying a resonance energy no higher than ≈ 206 keV – in disagreement with the literature resonance energy value of 212 keV [57, 59]. Based on the literature resonance energy value, a beam energy of 215 keV/u should pro-vide zero yield as its energy already below the resonance energy when it enters the target. This result raised concerns about the accuracy of the MD1 energy calibration. After a shut-down period of almost one month, a follow-up experimental run was done to acquire more data at beam energies in the vicinity of 215 keV/u to verify reproducibility of the previous yield result and to determine the resonance energy. At a beam energy of 214.9 keV/u and 214.3 keV/u, once again, yield was conclusively observed; whereas, at $E_{beam} = 213.5$ keV/u zero yield was observed. Subsequent stable beam reaction studies [52] with resonances of known strength and energies were carried out to verify the original MD1 calibration and, indeed, the original calibration result was confirmed, supporting the conclusion that the lit-erature result on the energy of this state must be in error. In total, five on-resonance data points were obtained along with three off-resonance data points defining the low energy side

---

[5]I use beam energy values in this section when discussing the experimental procedure. The conversion of beam energy to centre of mass energy is given by equation 2.6. Table 4.3 provides a convenient listing of beam energies discussed here with their corresponding centre of mass energies.

of the thick target yield curve, and one off-resonance datum point defining the high energy side of the yield curve. The measurements were only possible to obtain by investigating the TOF coincidence data between the γ-array and the DSSSD.

The γ-recoil coincidence data are shown in figures 4.9 through 4.13. All of these figures are structured in the same manner and are comprised of events from the coincidence bank of the raw experimental data. The top left panel shows the coincident γ-ray energy versus associated heavy ion (be it fusion recoil or leaky beam) time of flight. Prominent in these panels are the events clustered about a narrow TOF window, and spanning the range of γ-ray energies expected from the decay of this state: 5.7 MeV and 4.5 MeV. These events are highlighted by the red rectangle, 300 ns wide, showing the cuts imposed on these data. The top right panel shows a histogram of the z-coordinate, relative to the gas target centre, of the BGO crystal which detected the reaction γ-ray. Apart from the data at 214.3 keV/u, which is too dispersed to see any peak in this plot, if one leafs through the pages looking at this panel, one observes the centroid of the histogram moving along from negative to positive values in z; showing that the coordinate along the beam axis where the resonance reaction occurs "marches" through the target as the beam energy increases. In the bottom left panel is shown a projection of the heavy ion TOF values for those events with γ-ray energies $3 \text{ MeV} \le E_\gamma \le 6.5\text{MeV}$; the sharp TOF peak is prominent. Lastly, the bottom right panel shows a histogram of the heavy ion "energy", as an ADC channel number, as detected by the DSSSD. Do note that the data at $E_{\text{beam}} = 214.3$ keV/u was acquired with a nominal gas target pressure of 2.5 Torr, whereas the data at $E_{\text{beam}} = 214.9$ keV/u was taken with a nominal gas target pressure of 4.6 Torr. As a result, recoils exiting the target in the case of the former will experience less ionization energy loss than those in the case of the latter. This explains why the recoil energy histogram at 214.3 keV/u, of figure 4.9, is centered around a higher channel number than that of the 214.9 keV/u data of figure 4.10. It can also be seen in figures 4.10 and 4.11 that the energy centroid channel number between the data at 214.9 and 215.0 keV/u are also disparate. The data taken at 215.0 keV/u were taken in Nov. of 2001; the data taken at 214.9 keV/u were taken in Jan. 2002. At the conclusion of the Nov. 2001 data run, the original DSSSD detector was damaged from an accidental exposure to full-intensity beam. The disparity, therefore, in the DSSSD channel number is, therefore, the result of the installation of a new DSSSD detector for the Jan. 2002 data: the new DSSSD detector was not calibrated to match the original.
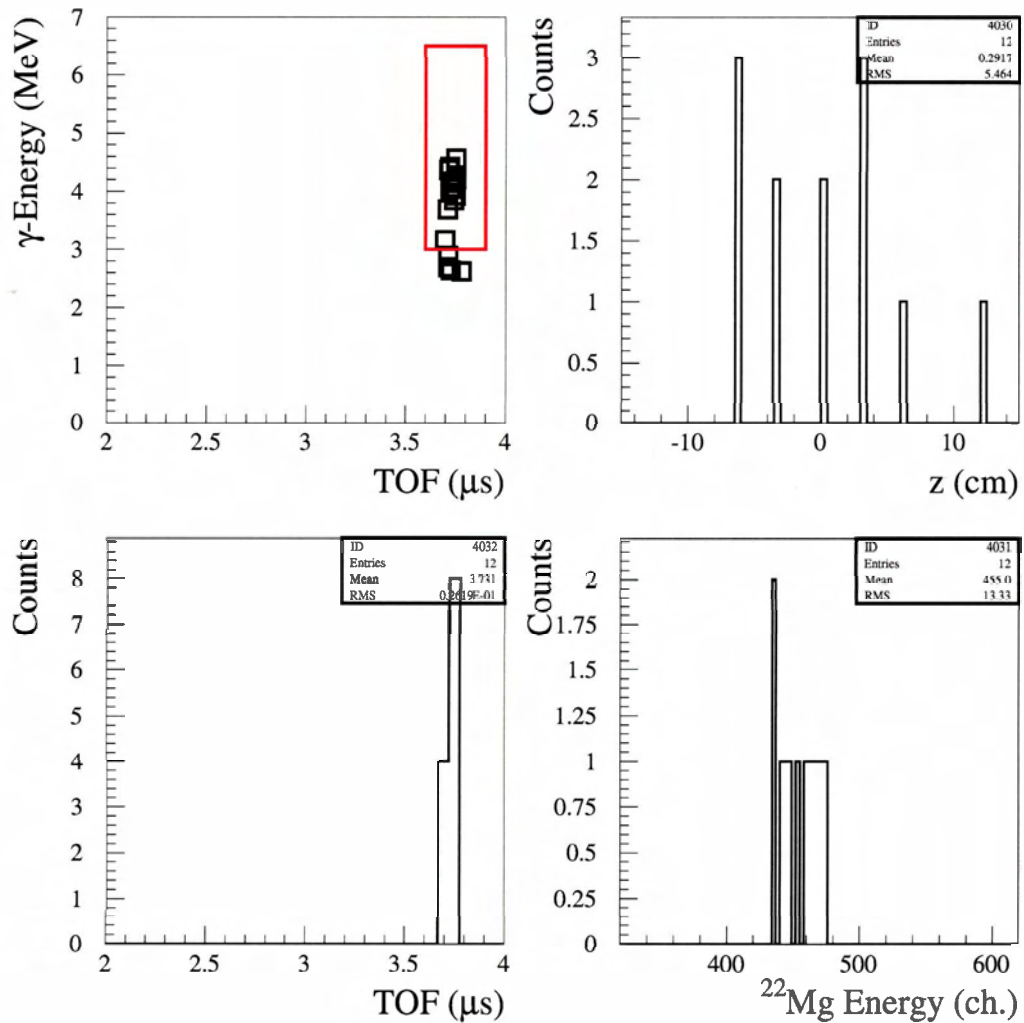
Figure 4.9: Coincidence data for the ^{21}Na(p,γ)^{22}Mg at $E_{\text{beam}} = 214.3$ keV/u. Top left: detected γ-ray energy versus the associated heavy ion time of flight. Top right: z-coordinate, relative to gas target centre, of triggered BGO crystal. Bottom right: projection of all time of flight events with γ-ray energies ≥ 3 MeV. Bottom right: DSSSD heavy ion energy (channel number).
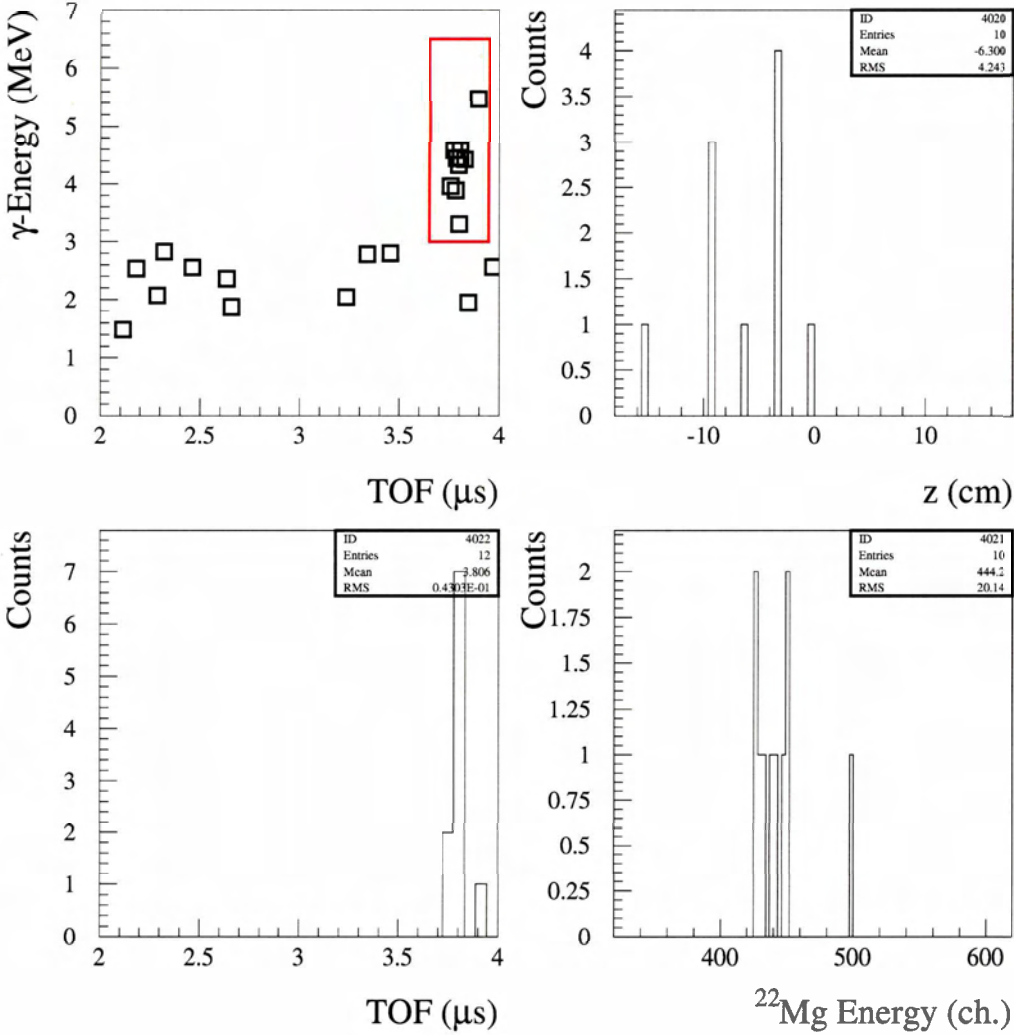
Figure 4.10: Coincidence data for the ^{21}Na(p,γ)^{22}Mg at $E_{beam} = 214.9$ keV/u. Top left: detected γ-ray energy versus the associated heavy ion time of flight. Top right: z-coordinate, relative to gas target centre, of triggered BGO crystal. Bottom right: projection of all time of flight events with γ-ray energies ≥ 3 MeV. Bottom right: DSSSD heavy ion energy (channel number).
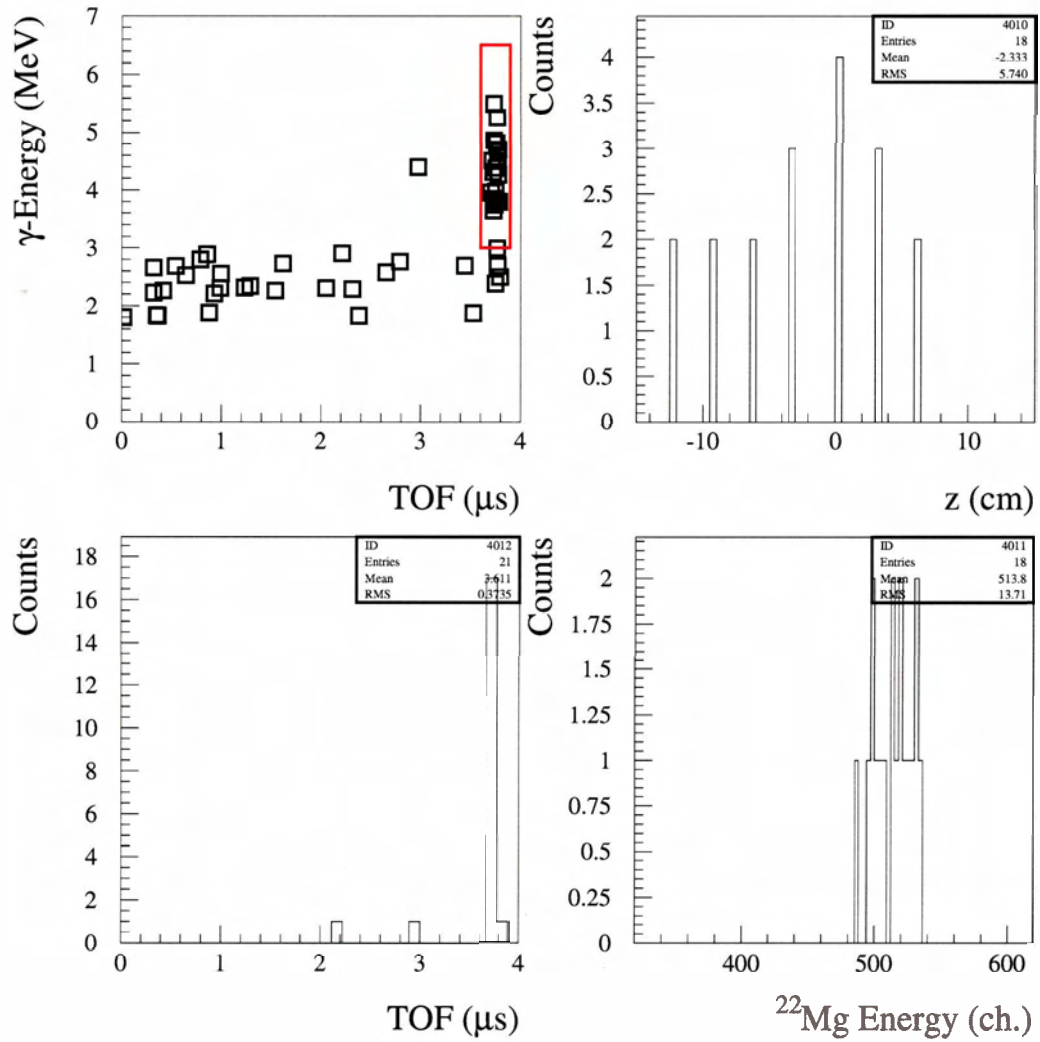
Figure 4.11: Coincidence data for the ^{21}Na(p,γ)^{22}Mg at $E_{beam} = 215.0$ keV/u. Top left: detected γ-ray energy versus the associated heavy ion time of flight. Top right: z-coordinate, relative to gas target centre, of triggered BGO crystal. Bottom right: projection of all time of flight events with γ-ray energies ≥ 3 MeV. Bottom right: DSSSD heavy ion energy (channel number).
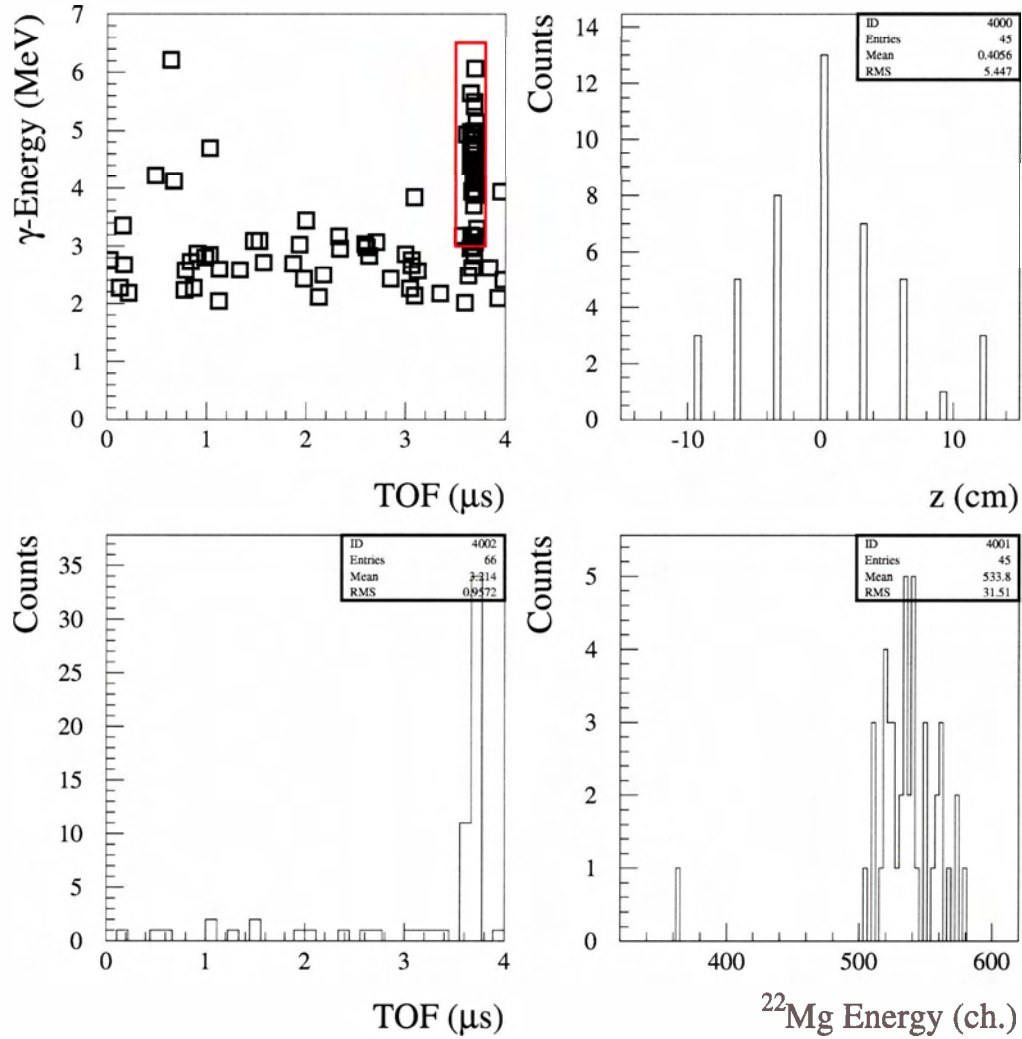
Figure 4.12: Coincidence data for the ^{21}Na(p,γ)^{22}Mg at $E_{\text{beam}} = 220.0$ keV/u. Top left: detected γ-ray energy versus the associated heavy ion time of flight. Top right: z-coordinate, relative to gas target centre, of triggered BGO crystal. Bottom right: projection of all time of flight events with γ-ray energies ≥ 3 MeV. Bottom right: DSSSD heavy ion energy (channel number).
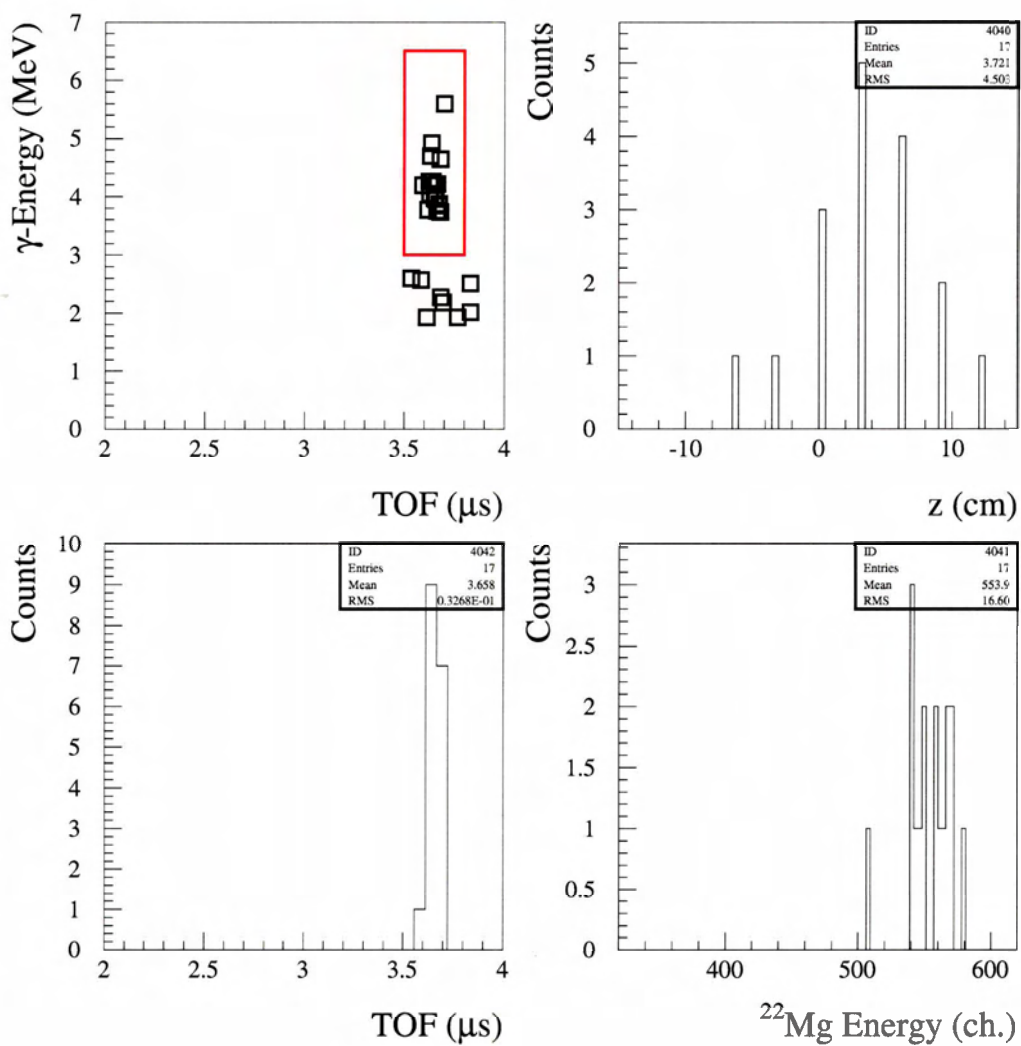
Figure 4.13: Coincidence data for the ^{21}Na(p,γ)^{22}Mg at $E_{\text{beam}} = 225.1$ keV/u. Top left: detected γ-ray energy versus the associated heavy ion time of flight. Top right: z-coordinate, relative to gas target centre, of triggered BGO crystal. Bottom right: projection of all time of flight events with γ-ray energies $\geq$ 3 MeV. Bottom right: DSSSD heavy ion energy (channel number).

Events within the red rectangle of figures 4.9 to 4.13 were all accepted as is, with the exception of one event in the 220 keV/u data set, figure 4.12. In the bottom right panel of this figure can be seen an anomalous heavy ion event lying at an energy approximately 30% lower than the main cluster of events. The TOF region between 0 to 3.2 μs, in the top left panel of figure 4.12, contains 13 background events with γ-energies greater than 3 MeV. These events provide a simple estimate on what the probability is for a random event to occur in the time window of real coincidence events. Scaling the background events by the ratio of the time window they occupy to the TOF time window, the estimate is found to be,

$$\frac{13}{3.2}0.3 \approx 1 \text{ event.}$$

This estimate, combined with the suspiciously low energy of the anomalous heavy ion event, warrants the rejection of this event as background i.e., a leaky beam particle from a previous beam pulse arriving in the real TOF window. Thus, the data at 220 keV/u is quoted to have 44 valid recoil events. The runs at 210.8, 211.9, 213.5 and 230.8 keV/u all had zero γ-recoil coincidence events.

Table 4.3 summarizes the results of the recoil counts for each beam energy, the total beam on target for each beam energy, the γ-array efficiency at each beam energy, and the approximate position along z, from the target entrance aperture, of the resonance reaction, z_{res}. Since figure 4.3 shows the γ-array efficiency as a function of z – and not of beam energy – these z_{res} positions formed the basis of choosing the γ-array efficiencies for each beam energy. They were calculated by a simple ratio and proportion relating the energy loss through the gas target and its known effective length (12.3 cm), to the difference in energy between the beam energy and resonance energy, i.e.,

$$z_{\text{res}} = \frac{12.3}{\Delta E_{\text{target}}} \left(E_{\text{beam}} - E_{\text{r}}^{\text{lab}} \right),$$

where $\Delta E_{\text{target}} = 14.36 \pm 0.40$ keV/u and $E_{\text{r}}^{\text{lab}}$ is the resonance energy converted from the centre of mass frame into the laboratory frame. The resonance energy used in this expression was not the literature value of 212 keV/u, but instead the result determined from this work: 205.7 keV, which will be shown in the next section. A universal systematic uncertainty of 10% has been adopted for all γ-array efficiencies in this work, as the calibration of the γ-array and direct comparison of such calibration with the GEANT simulation is still ongoing [56].

4.6.1 Thick Target Yield Curve and Resonance Strength

Equation A.14 in Appendix A gives the maximum likelihood estimator for the experimental yield, Y, as a sum over single experimental runs, at a particular beam energy, involving the number coincidence recoils, integrated beam on target and the various DRAGON efficiencies, for each experimental run. The result is,

$$Y = \frac{\sum_i r_i}{\sum_i \varepsilon_i \eta_i \theta_i \delta_i f_i} , \tag{4.4}$$

where r_i is the total number of recoils in the i'th run, f_i is the total beam on target for the i'th run, and ε_i, θ_i, and δ_i are the γ-array, transmission and DSSSD efficiencies, respectively, and η_i is the charge state fraction, all for the i'th run. The reader is referred to Appendix A for the full derivation of this formula. From stable beam reaction studies, a transmission efficiency of at least $\theta_i = 0.98 \pm 0.2$ [52] is adopted for these data. Similarly, α-particle studies revealed that the DSSSD efficiency is at least $\delta_i = 0.99 \pm 0.1$ [60]. These values are universally adopted for all data in this work.

Table 4.3: Summary of the values used to determine the $\omega\gamma$ for $^{21}\mathrm{Na}(p,\gamma)^{22}\mathrm{Mg}$ at $E_{\mathrm{cm}} = 212$ keV, with $\varepsilon = \gamma$-array efficiency, $z_{\mathrm{res}} = z$ coordinate of the resonance relative to entrance aperture.

Parameters for Thick Target Yield Curve					
Beam Energy (keV/u)	E_{cm} (keV)	z_{res} (cm)	ε	Beam $(\times 10^{12})$	Recoils
210.8	202.7	0	0.45(4)	11.30(34)	0
211.9	203.8	0	0.45(4)	7.35(18)	0
213.5	205.3	≤ 1	0.45(4)	3.51(11)	0
214.3	206.1	≤ 1	0.45(4)	9.37(22)	12
214.9	206.7	≤ 1	0.45(4)	12.24(29)	10
215.0	206.8	≤ 1	0.45(4)	15.59(38)	18
220.0	211.0	4	0.48(5)	35.67(79)	44
225.1	216.4	8	0.47(5)	25.55(61)	17
230.8	222.0	12	0.43(4)	8.69(26)	0

The magnesium charge state fraction for these data was measured during a stable beam reaction study [52] of the $^{24}Mg(p,\gamma)^{25}Al$ reaction at $E_{cm} = 214$ keV. From equation 4.1, the predicted recoil charge state of highest probability is 4^+, and it was this recoil charge state that was selected on for all these data. The predicted 4^+ charge state fraction for ^{24}Mg is 0.413. From the aforementioned stable beam study, it was measured as 0.443 ± 0.014 – a relative difference of 8% with the theory – and suggestive of the error to use for recoil charge state fractions not directly measured, such as those for the $E_{cm} = 335$ keV reaction study. Finally, the ionization energy loss through the gas target was measured to be $(8.16 \pm 0.40) \times 10^{-17}$ keV/(atom/cm^2).

When substituted in equation 4.4, the aforementioned efficiencies combined with the γ-array efficiencies and integrated beam on target values, tabulated in table 4.3, produce a thick target yield curve for these data as shown in figure 4.14. The vertical error bars are 1σ confidence intervals as discussed in § A.3 of Appendix A. For the purposes of determining the resonance strength of this reaction, only the central datum point at $E_{cm} = 211.0$ keV ($E_{beam} = 220.0$ keV/u) has been used. The argument for this choice is as follows. We do not know the precise position of where the resonance reaction is taking place within the gas target. What we do know is that the $E_{cm} = 211.0$ keV, or $E_{beam} = 220.0$ keV/u, yield point is certainly within 1 cm of the gas target centre, based on its estimated z_{res} value and based on the histogram of z-coordinate of those BGO crystals that detected coincident γ-rays from the reaction (top right panel of figure 4.12). The efficiency response of the γ-array in the region ± 1 cm of the gas target centre is flat, as seen in figure 4.3, eliminating additional uncertainties in its value as a result of uncertainty in the resonance position in the target. On the other hand, the data points clustered around $E_{cm} = 206.0$ keV do not have a well-defined position in the gas target to allow for a choice of γ-array efficiency that is better than about 7%. The reason for this is that the gas profile of the target extends beyond the entrance aperture. How much it is extended beyond the aperture is not well-known. The data points around $E_{cm} = 211.0$ keV are extremely close to the actual resonance energy, and as a result, it might well be that the reaction was actually taking place outside the gas target cell for these events. The efficiency curve of the γ-array is dropping steeply at the location of the entrance aperture (-5.5 cm). The range in efficiencies between -6 to -5 cm, a reasonable best guess on the resonance position, is 43 to 46%, or a relative variation of 7%. This uncertainty would have to be included with the 10% uncertainty already assigned

Table 4.4: Summary of efficiencies and systematic errors for thick target yield at $E_{cm} =$ 211.0 keV.

Factor	Value	Syst. Error (%)
γ-array efficiency	0.48	10
Separator transmission	0.98	2
DSSSD efficiency	0.99	1
Charge state fraction	0.44	3
Integrated beam	3.57×10^{13}	2.2
dE/dx [keV/(atom/cm^2)]$_{lab}$	8.16×10^{-17}	5

to the GEANT simulation results. In the interest of keeping the systematic uncertainties minimal, and because the central datum point also has the greatest amount of statistics, only the central datum point is chosen to determine $\omega\gamma$. From the central yield datum point of figure 4.14, the thick target yield is found to be,

$$Y_{max}(\infty) = (5.98 \pm 0.90_{stat} \pm 0.65_{syst}) \times 10^{-12} .$$

The statistical error is obtained from expression A.15 of § A.2 in Appendix A. When this result is used in equation 2.40, the resonance strength for this reaction is determined to be,

$$\omega\gamma = (1.07 \pm 0.16_{stat} \pm 0.13_{syst}) \text{ meV} .$$

Table 4.4 summarizes the efficiency values, laboratory ^{21}Na stopping cross section, with their corresponding systematic errors, used to obtain these results.

The data of figure 4.14 tightly constrain the value of the resonance energy to lie somewhere between 205.3 $\pm$ 0.5 keV and 206.1 $\pm$ 0.5 keV. A value of $E_r = (205.7 \pm 0.5)$ keV is adopted by splitting the energy interval between these two data points in half. The error is systematic and based on the RMS spread of MD1 energy measurements from a large sample of beam energy experiments [61].

The curve shown in figure 4.14 is a template curve as a guide for the eye. It is comprised of a convolution of the Breit-Wigner cross section of equation 2.28 with a Gaussian energy profile, of rms energy width 0.5%, to respresent the beam energy spread. The curve has
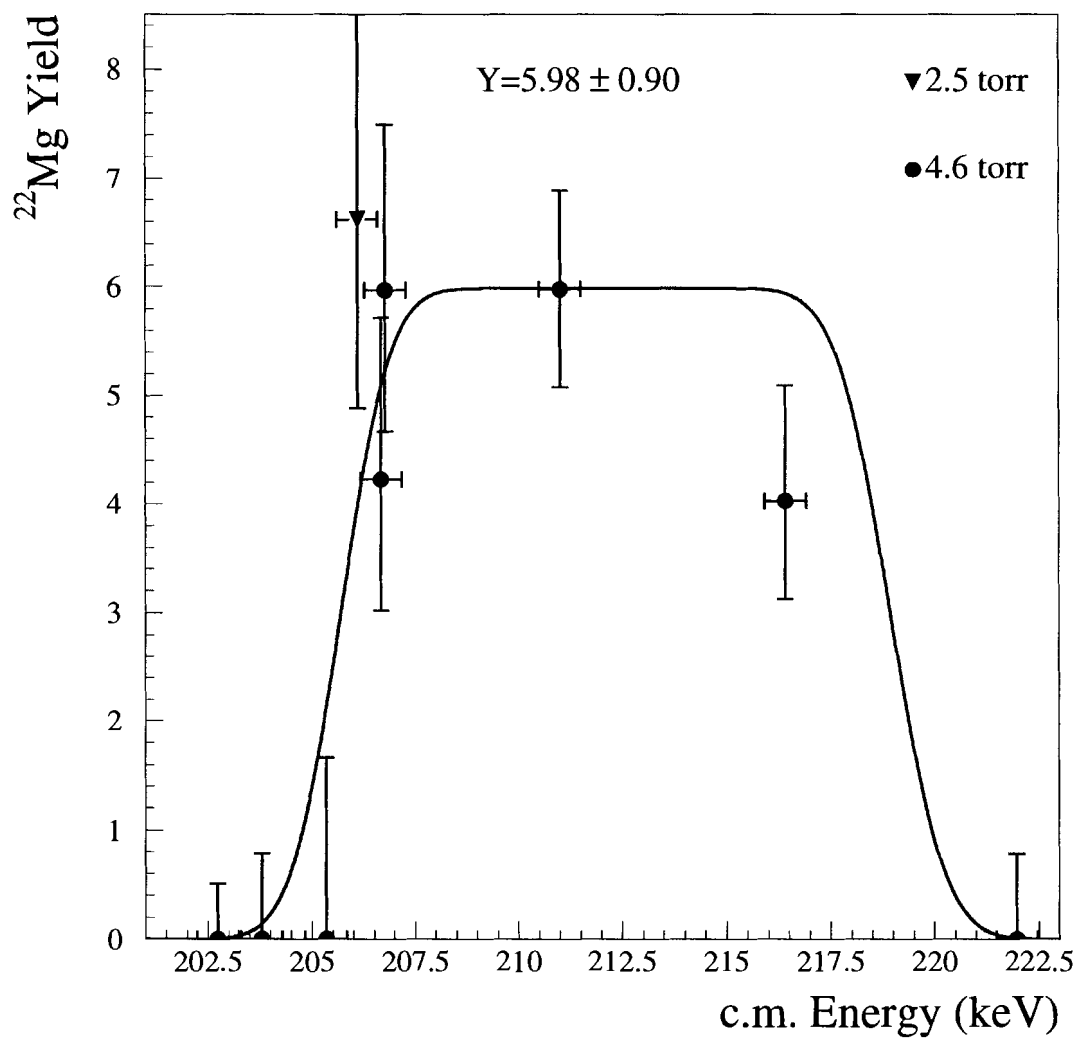
Figure 4.14: Thick target yield curve, scaled by 10^{12}, for the 212 keV resonance of the $^{21}Na(p,\gamma)^{22}Mg$ reaction. Note that the resonance energy is not found to be at 212 keV. Horizontal error bars denote energy uncertainty of 0.5 keV.

been normalized to the determined values for $\omega\gamma$ and E_r, and has used the literature value for the total width, $\Gamma = 16.5$ meV [29, 62], along with the experimentally determined target thickness. The breadth of the low energy shoulder of the curve reasonably matches the data when the beam energy spread is included.

4.6.2 ^{22}Mg Mass Excess

That the result of this work finds the energy of the literature-adopted 212 keV state to be at 205.7 keV, raises the issue of how well known is the ^{22}Mg mass. The threshold Q value for the ^{21}Na(p, γ)^{22}Mg reaction is,

$$Q = m_p + M_{21} - M_{22} ,$$

(4.5)

with m_p, M_{21}, and M_{22} the masses of the proton, sodium and magnesium, respectively. The Q value can also be written as,

$$Q = E_x - E_r ,$$

(4.6)

where E_x is the excitation energy of the resonance state above the ground state of the nucleus. The excitation energy of this state was originally determined by a direct measurement [57] of the γ-ray emission from the deexcitation of this state using a high resolution Germanium detector and is given by (5714.4 $\pm$ 1.5) keV. The Q value, however, being directly dependent on the ^{22}Mg mass, is probably where discrepancy lies between this work and the literature. The mass excess, Δ_A, for atomic number A is defined as,

$$\Delta_A = M_A - A ,$$

(4.7)

with M_A the atomic mass of A. By this definition, we can write the expression for the Q value for the ^{21}Na(p, γ)^{22}Mg reaction in the alternative form,

$$Q = \Delta_p + \Delta_{21} - \Delta_{22} .$$

(4.8)

The adopted value for the excitation energy of this state is $E_x = 5713.9(1.2)$ keV [59]. In addition, the presently adopted values for the reaction Q value and ^{22}Mg mass excess are $Q_{lit} = 5501.5(1.5)$ keV [44] and $\Delta_{22} = -396.8$ keV [63], respectively. Assuming that E_x is correct and that the discrepancy between this work and the literature lies strictly in the ^{22}Mg mass we can write, using expression 4.6 with 4.8,

$$Q_{lit} - Q_{new} = 212.4(1.9) - 205.7(5) = -396.8(1.4) - \Delta_{22}^{new} ,$$

yielding: $\Delta_{22}^{new} = (-403.5 \pm 2.4)$ keV.

4.7 ^{21}Na$(p,\gamma)^{22}$Mg Reaction at $E_{cm} = 335$ keV

No γ-recoil coincidence events were observed in the search for reaction yield of the resonance at $E_{cm} = 335$ keV. A lab beam energy of 360 keV/u was used in this search. Figure 4.15 shows a plot of all coincident events that were recorded by the DRAGON data acquisition. Above 3 MeV there are zero events and, moreover, there are no events in the vicinity of the expected recoil time of flight, as indicated by the lack of events nearby the box. The energy loss through the gas target at 8 Torr was 28.2 keV/u over the effective target length of 12.3 cm. A resonance energy of 335 keV corresponds to a lab beam energy of 351 keV/u. This implies that the beam ions had to lose $\Delta E_{lose} = 9$ keV/u in the target to reach the resonance energy. Thus, the approximate position from the entrance aperture of where the resonance should have occurred at in the target is given by a simple ratio and proportion:

$$z_{res} = \left(\frac{\Delta z}{\Delta E}\right) \Delta E_{lose} = \frac{12.3}{28.2} \cdot 9 \text{ cm} \approx 4 \text{ cm},$$

or about 1 cm away from the gas target centre. Inspection of figure 4.3 (lower panel) shows the γ-array efficiency to be 0.38 at that location in z, and it is this value that has been used in the calculations, with an assigned systematic error of 10% of the value, or 0.04 absolute. For these data, one run in the experiment was set to accept ^{22}Mg recoils in a charge state of 6^+ while all other runs were set to accept 5^+ recoils. Charge state fractions of $\eta_5 = 0.48 \pm 0.04$ and $\eta_6 = 0.27 \pm 0.02$ are adopted for the ^{22}Mg recoils of charge states 5^+ and 6^+, respectively, on the basis of calculations from the model and data of Liu [54, 55]. The assigned error is taken as 8% of the value predicted by the model of Liu [54, 55], as suggested in § 4.6.1.

Inequality A.24 of Appendix A gives the result for determining the 1σ upper limit on a Poisson variable when zero counts are observed. The reader is referred to Appendix A for its derivation. Using that inequality and the values in table 4.5 results in a statistical upper limit for the reaction yield of this resonance of:

$$Y \leq -\frac{1}{(1.51 + 0.044) \times 10^{12}} \ln(0.32) = 7.32 \times 10^{-13}, \tag{4.9}$$
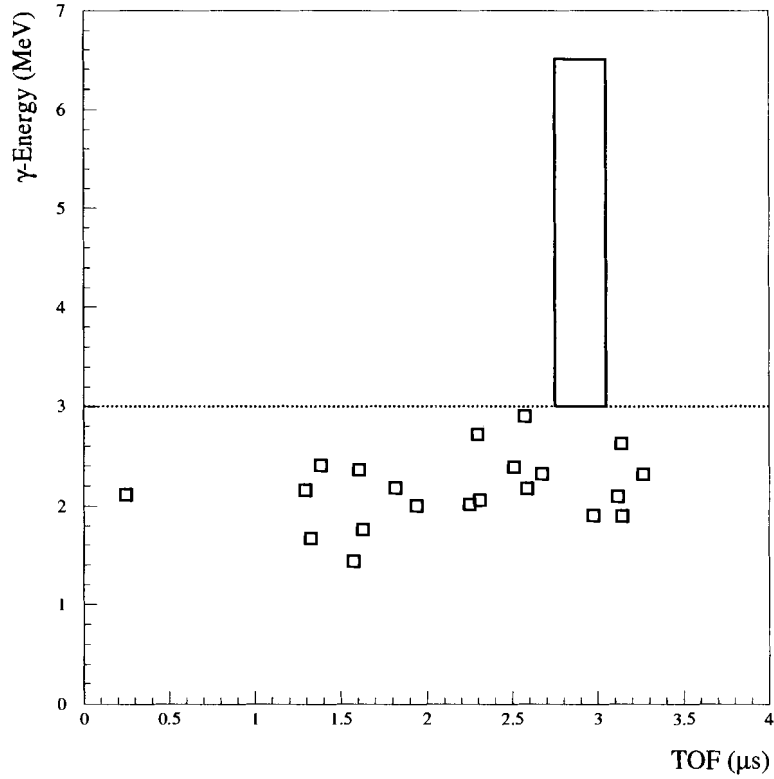
Figure 4.15: Detected coincident γ-ray energy versus heavy ion time of flight for all runs at $E_{\text{cm}} = 335$ keV. No valid recoil candidates are observed.

with a systematic error of approximately 1.00×10^{-13}. Adding these two results linearly gives a conservative upper limit on the reaction yield of 8.32×10^{-13}. From these, the upper limit on the strength of this resonance is,

$$\omega\gamma \leq 0.28 \text{ meV}. \tag{4.10}$$

This state was originally identified on the basis of a γ-ray energy spectrum derived from a $(^3\text{He}, n\gamma)$ transfer reaction measurement [57] but has never been confirmed in any other experiments, including an independent $(^3\text{He}, n\gamma)$ measurement [62], four (p, t) transfer reaction studies [41, 42, 64, 65], an $(^{16}\text{O},^6\text{He})$ measurement [43], a $(^3\text{He},^6\text{He})$ measure-

Table 4.5: Summary of the values used to determine the limit on $\omega\gamma$ for ^{21}Na$(p,\gamma)^{22}$Mg at $E_{cm} = 335$ keV. $\eta = \gamma$-array efficiency, $\eta =$ charge state fraction, $\theta =$ transmission efficiency, $\delta =$ DSSSD efficiency, $\chi = \varepsilon\eta\theta\delta \times$ Beam.

Parameters for $\omega\gamma$ Limit							
Charge State	$dE/\rho dx(\times 10^{-17})$ (keV/atom/cm^2)	ε	η	θ	δ	Beam ($\times 10^{12}$)	χ ($\times 10^{12}$)
5^+	9.35(38)	0.38(4)	0.48(4)	0.98(2)	0.99(1)	8.69(10)	1.51(21)
6^+	9.35(38)	0.38(4)	0.27(2)	0.98(2)	0.99(1)	0.453(15)	0.044(6)

ment [66], and a (^{4}He,^{6}He) measurement [67]; we have not observed it through this direct reaction study. The derived limit and the preponderance of experimental evidence strongly suggests that the inclusion of this state in the ^{21}Na$(p,\gamma)^{22}$Mg thermonuclear reaction rate should be reconsidered.

4.8 Resonant ^{21}Na$(p,\gamma)^{22}$Mg Reaction Rate

From equations 2.31, 2.34 and the preceding results, the resonant ^{21}Na$(p,\gamma)^{22}$Mg reaction rate is derived. Figure 4.16 shows, for the temperature range of ONe novae, the resonant reaction rate of the 205.7 keV state based on the the present work (solid black curve) along with rates based on two previous works, using indirect methods, by Bateman et al. [41] (solid red curve) and José et al. [29] (solid green curve). Using the same colour scheme, the rate curves of the 335 keV state are shown dashed. The work of Bateman et al. [41] adopted values for $\omega\gamma$ of 2.4 and 32 meV for the 205.7 keV and 335 keV states, respectively, on the basis of shell model calculations. José et al. [29] adopted $\omega\gamma$ values of 0.25 and 11 meV for the 205.7 keV and 335 keV states, respectively. Both of these previously adopted strengths for the 335 keV state overestimate its rate by factors ranging from ≈ 40 to ≈ 1000 over the present limit is on its maximum rate. In the case of the 205.7 keV rate, Bateman et al.'[41] overestimate it by a factor of 2.5, and José et al. [29] underestimate it by a factor of 4. Figure 4.16 makes it evident that any contribution of the 335 keV state to the resonant nova

reaction rate is wholly negligible across *all* nova temperatures, being at least ≈ 3 orders of magnitude reduced over the 205.7 keV rate. Lastly, figure 4.17 shows the total resonant reaction rate derived from the 205.7 and 335 keV resonance strengths of the present along with those of Bateman et al. [41] and José et al. [29], using the same colour scheme as in figure 4.16. The upper limit on the rate of the 335 keV resonance has been added directly to that of the 205.7 keV rate viz equation 2.34, and comparison of this summed result to the 205.7 keV rate curve in figure 4.16 shows negligible change in the total rate as a result of the 335 keV rate contribution. The blue hatched region shows the total error (statistical plus systematic in quadrature) region of the 205.7 keV rate.

The results of the present work have reduced the range of uncertainty of the contribution of the 205.7 and 335 keV ^{22}Mg states to the resonant ^{21}Na(p, γ)^{22}Mg reaction rate by ≈ 10-fold over most of the nova temperature range, with an uncertainty on the rate now being just 21%, and have shown that the state at 335 keV, if it does exist, does not play an important role in the ^{21}Na(p, γ)^{22}Mg reaction rate nor in the production of ^{22}Na.
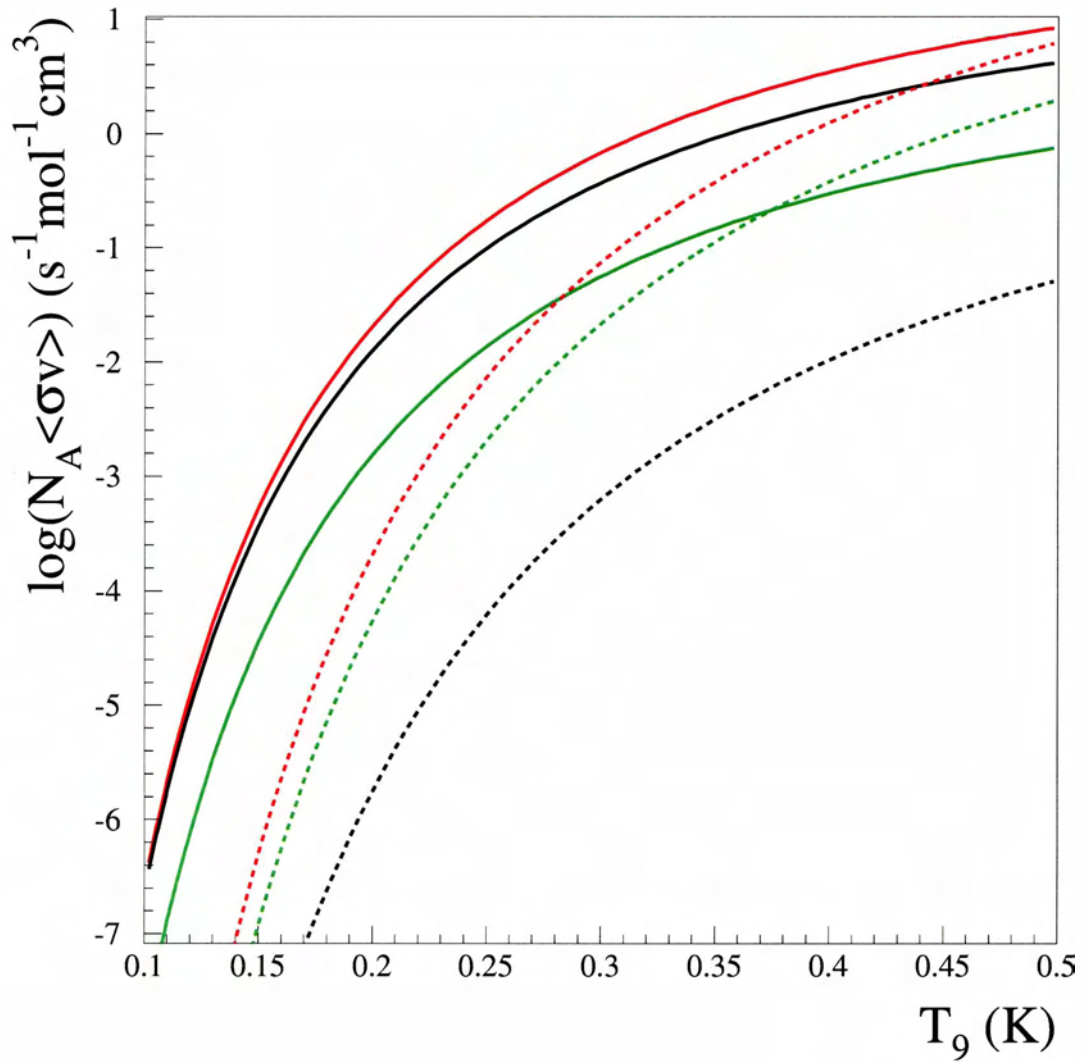
Figure 4.16: Resonant ^{21}Na(p,γ)^{22}Mg reaction rates for the $E_{cm} = 205.7$ keV state (formally 212 keV), solid curves, and the $E_{cm} = 335$ keV state, dashed curves. The black curves are the rates derived from the present work, the green curves are from José et al. [29] and the red curves are from Bateman et al [41].
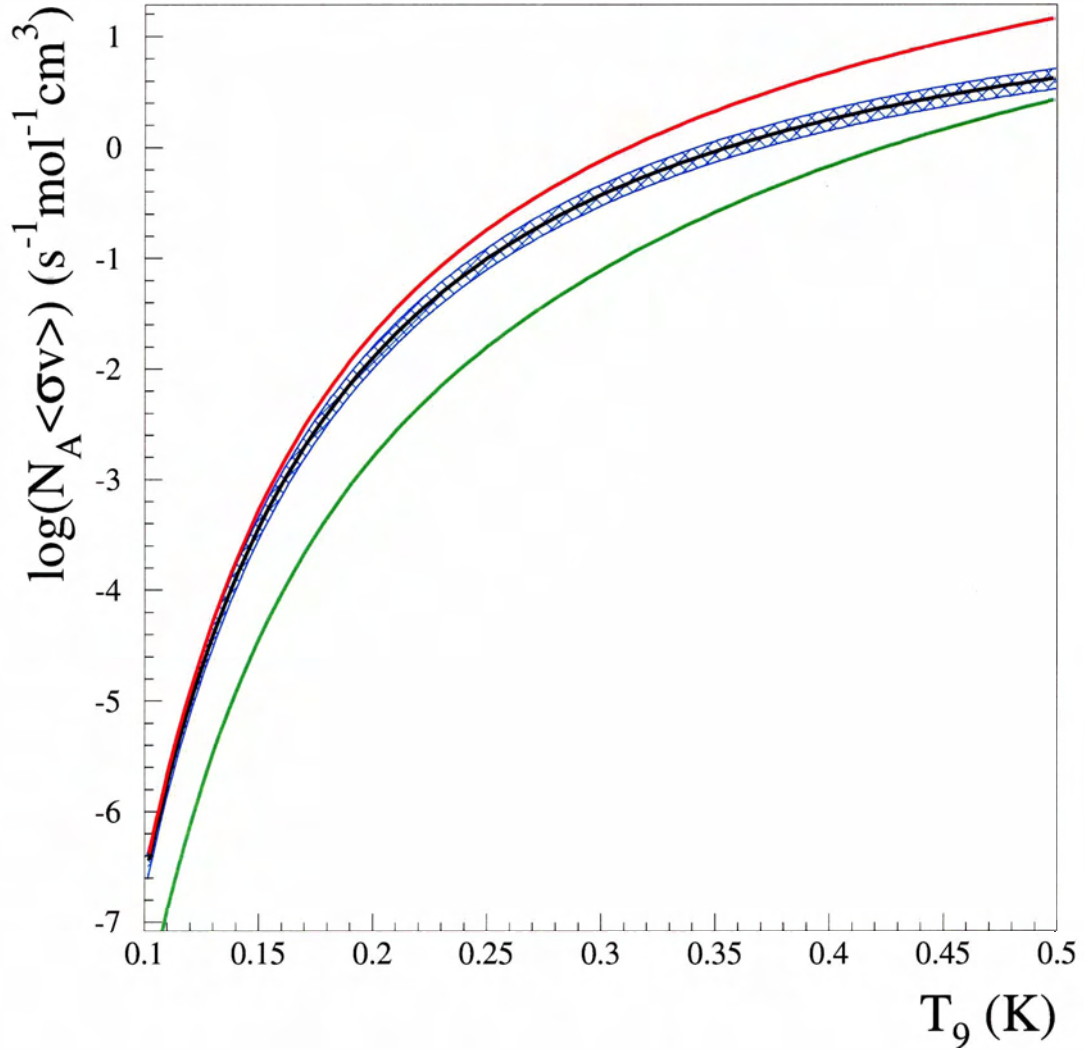
Figure 4.17: Total resonant ^{21}Na(p,γ)^{22}Mg reaction rate of the 205.7 and 335 keV ^{22}Mg states based on the results from the present work. The black curve is the rate derived from the present work, with the error (statistical plus systematic in quadrature) on the rate denoted by the hatched region. The green curve is from José et al. [29] and the red curve is from Bateman et al [41].

Chapter 5

Conclusions & Discussion

A direct measurement of the resonant ^{21}Na$(p, \gamma)^{22}$Mg reaction rate, relevant for production of the important astrophysical observable ^{22}Na, has been completed. This rate has been determined by directly measuring, in inverse kinematics, the resonance strengths of two states in the ^{22}Mg nucleus. The first of these two states, with assigned literature energy of 212.9 keV [44, 57], has been found to lie at an energy of 205.7 ± 0.5 keV; some 6.7 keV lower in energy than previously known. This result is based on the inflection point of the low energy flank of a thick target yield curve, mapped out for the first time ever using a radioactive beam of ^{21}Na. A mass excess of $\Delta_{22} = -403.5 \pm 2.4$ keV is derived for the ^{22}Mg nucleus.

From this work, the derived value for the resonance strength of the 205.7 keV state in ^{22}Mg is $\omega\gamma^{205} = 1.07 \pm 0.16_{\text{stat}} \pm 0.13_{\text{syst}}$ meV. An upper limit of $\omega\gamma^{335} \leq 0.27$ meV has been derived for the state at 335 keV. The present work has also shown that the resonant ^{21}Na$(p, \gamma)^{22}$Mg reaction rate is dominated by the resonance state at 205.7 keV in the ^{21}Na + p system; while the the established limit on the strength of the resonance state at 335 keV implies it cannot contribute anything more than negligible amounts to the total reaction rate in ONe novae. Uncertainties on the resonant component of the ^{21}Na$(p, \gamma)^{22}$Mg reaction rate have been reduced from a factor of $\approx 1000\%$ down to an uncertainty of just 21%.

Recently, and independently of the results of this work, the mass excess of ^{22}Mg has undergone a reevaluation [68]. The ^{22}Mg mass excess was originally determined, in part, by a ^{24}Mg$(p,t)^{22}$Mg transfer reaction [69]. The magnetic spectrometer used to determine the energy of the emitted tritons was calibrated based on the Q value of the ^{16}O$(p,t)^{14}$O

reaction [68, 69]. In the intervening 29 years, this Q value has been updated [44]. Incorporating the modern Q value for this reaction, the original author now determines a ^{22}Mg mass excess of -402 ± 3 keV [68], in agreement with the result of this work.

Further support of this result comes from another experiment performed very recently at the Wright Nuclear Structure laboratory, Yale University. A transfer reaction employing ^{24}Mg(p, t)^{22}Mg shows a preliminary result [70] indicating a smaller mass excess for ^{22}Mg, by a few keV, over what is presently adopted in the literature [44].

In another recently completed ^{24}Mg(p, t)^{22}Mg transfer reaction experiment [65], excited states in ^{22}Mg were populated by the bombardment of a 55 MeV/u ^{24}Mg beam on a 1 mg cm^{-2} (CH)$_2$ target. Triton ejectiles and ^{22}Mg recoils from this (p,t) reaction both entered a magnetic spectrometer downstream of the target. The excited ^{22}Mg recoils deexcited by way of γ-emission or proton decay within the spectrometer. In this approach, proton decays of the excited ^{22}Mg are identified through ^{21}Na-triton coincidences. Reconstruction of the triton momenta spectrum, from this coincidence measurement, determines what state of ^{22}Mg proton decayed. In this way, the branching ratio for proton decay can be determined, permitting a measure of the resonance strength when combined with the known total width of the state. This experiment detected no statistically significant signal for proton decay of the 205.7 keV state in ^{22}Mg i.e., background was the only detectable signal, and an upper limit on the proton decay branching ratio was obtained as 0.020. The lifetime of this state is known to be (40 $\pm$ 15) fs [62], corresponding to a total width[1] of (16 $\pm$ 7) meV. This lifetime and proton decay branching ratio do not produce a resonance strength for this state that is consistent with the result of this work. In fact, to obtain consistency with the result of this work, the author had to use a 95.5% confidence interval result of 65.8 meV – or seven times the quoted error of the derived total width from the lifetime measurement – on the total width of this state, in combination with his measured proton decay branching ratio, in order to obtain an upper limit of 0.80 meV for the strength of this resonance. A discrepancy of $\approx 7\sigma$ between this transfer reaction study and the result of this work exists. The results of this thesis for the resonance strength of the 205.7 keV state stand on a firm foundation of stable beam reaction studies [52], across a broad range of energies and kinematics, that have excellent agreement with the literature results for resonance strengths and energies; these results are summarized in Appendix C in tables C.1 and C.2. Moreover, the

---

[1]The total width is obtained viz $\Gamma = \hbar/\tau$, where τ is the lifetime of the state.

resonance strength result of this thesis, for the 205.7 keV state, has been determined from direct observation of γ-recoil coincidence events. These considerations, therefore, give a high degree of confidence for the results of this thesis in regard to the resonance strength of the 205.7 keV state in ^{22}Mg.

Recently, a model ONe nova model calculation has been performed [71] using the resonance strength of the 205.7 keV resonance, as derived from this work, along with the strengths of the 335 keV state (green curve of figure 4.16) and 460 keV state (figure 2.6) as used in José et al [29]. The model employed was a spherically symmetric hydrodynamical model nova outburst, incorporating a ONe white dwarf of mass $1.25M_\odot$, from the onset of accretion up to the explosion and ejection stages, and it was the same model as that used in José et al [29]; the only difference being the new strength and energy for the 205.7 keV state in ^{22}Mg. Abundance results for ^{22}Na for the new calculation were compared to that of the the original results of José et al [29]. It was found that the yield of ^{22}Na mass-fraction was reduced from 3.5×10^{-4} to 2.8×10^{-4}, using the derived $\omega\gamma^{205}$ of this work [71]. Because the $\omega\gamma^{205}$ of this work is higher than that used the original model calculation [29], the ^{21}Na(p,γ)^{22}Mg($\beta^+\nu_e$)^{22}Na synthesis path to ^{22}Na is favoured at earlier times in the outburst, reducing the role of the ^{21}Na($\beta^+\nu_e$)^{21}Ne(p,γ)^{22}Na path. As a result, ^{22}Na production occurs earlier in the outburst at a time when the expanding envelope is still sufficiently dense and hot to allow ^{22}Na destruction from proton capture, reducing its final yield as compared with the old rate. One may now ask how these results will change now that it is known that the rate contribution of the 335 keV state is negligible (compare 335 keV state rate curves in figure 4.16). The Gamow window of figure 2.2 indicates that a state at 335 keV will only contribute at nova temperatures in excess of ≈ 300 MK. Temperatures such as this are typical of the peak temperatures of the models [29]. After this peak in temperature, the burning shell begins to drop in density and cool down as a result of its expansion from ejection. Thus, hydrodynamically, it is expected that the states at 335 keV and 460 keV will not have a chance to significantly contribute to the total ^{21}Na(p,γ)^{22}Mg reaction rate because, in the temperature regime where they could contribute, the burning shell is expanding, becoming less dense, and cooling. We therefore expect that any new ONe nova calculations of the sort performed by José et al. [29] omitting the rate contribution of the 335 keV state, as suggested by the results of this work, will continue to yield underproduction of ^{22}Na abundances. The results of the present work are consistent, therefore, with the present state of

null 1.28 MeV γ-signature from ONe novae. In fact, the results seem to indicate that the ^{21}Na(p,γ)^{22}Mg reaction rate is fast enough to be detrimental to the survivability of ^{22}Na in the ejecta of ONe novae, provided the models are reliable.

The nova ^{21}Na(p,γ)^{22}Mg reaction rate could be enhanced if there are any additional, undiscovered, states in ^{22}Mg within ≈ 500 keV above the proton threshold (figure 2.6). The spin-parity assignments of these states have been made on the basis of angular distribution measurements [42] (and references in [41, 43]). Presently, the spin-parity assignments for the states at excitation energies of 5.714 and 6.046 MeV are firm[2], with the 5.714 MeV state traditionally assigned as the mirror state to the ^{22}Ne state at excitation energy 6.115 MeV. The ^{22}Mg state at excitation energy 5.962 MeV presently has an ambiguous spin-parity assignment of either $J^{\pi} = 1^{-}$ [42] or $J^{\pi} = 0^{+}$ [41, 43]. None of the present experimental evidence thus far indicates this state could be $J^{\pi} = 3^{-}$. Yet, there is a state in the mirror nucleus of ^{22}Ne of $J^{\pi} = 3^{-}$ with an excitation energy of 5.910 MeV which has been speculatively assigned as the mirror state to the unconfirmed 5.837 MeV state in ^{22}Mg. If, as the experimental evidence of this work and previous transfer reaction studies indicate, the 5.837 MeV state in ^{22}Mg does not exist, then there likely remains an hitherto undiscovered state in ^{22}Mg somewhere within the nova Gamow window of energy above the ^{21}Na + p proton threshold. This state, requiring an angular momentum transfer of $\ell = 1$, while probably suppressed over the 5.714 MeV state, could help enhance the nova reaction rate of ^{21}Na(p,γ)^{22}Mg . Finding it will likely require future γ-ray spectroscopy studies.

While no characteristic 1.28 MeV γ-ray line has ever been observed from the decay of ^{22}Na from an ONe candidate event, the future looks bright for detection with the European Space Agency's INTEGRAL satellite observatory, launched in October of 2002. Sensitivity studies [72] of the detection limit of the INTEGRAL γ-ray spectrometer [73] have been performed. The study employed a hydrodynamical model of a 1.15 and 1.25 $M_{\odot}$ ONe white dwarfs located at a distance of 1 kpc, coupled with a Monte Carlo simulation of photon transport through the ejecta shell modeling Compton scattering, photoelectric absorption and $e^{+}e^{-}$ pair production to mimic the degradation of line signatures, such as the 1.28 MeV line, due to these processes. It also included a Monte Carlo simulation of the INTEGRAL detector response function. From this study, the maximum flux of 1.28 MeV

---

[2]I am using the "old" values of these energies, i.e. excluding the energy shift implied by the new resonance energy of 205.7 keV for the 5.714 MeV state, for purposes of clarity with figure 2.6.

photons for each model nova were derived along with the detectability distance for INTE-GRAL's γ-spectrometer corresponding to this flux. The results indicate that INTEGRAL's detectability distance is just 0.5 kpc, or only half the distance to the model novae. However, it is typical of most novae models to have ejecta masses which are ≈ 2 orders of magnitude smaller than observation [72]. It has been found when the models are forced to eject 10 times more mass, the flux of photons increase by the same amount, as expected. This increases the INTEGRAL detectability distance by a factor of ≈ 3 to 1.5 kpc. By comparison, Nova Cygni 1992 is pegged at a distance somewhere between ≈ 2 to 3.2 kpc from Earth, and so any future nova event similar to Cygni might well have a detectable 1.28 MeV line, that is, if it is present to begin with.

While the contribution to ONe nova production of ^{22}Na from the 460 keV resonance in ^{22}Mg is probably marginal, except in the cases of the more massive ONe white dwarfs, attempts to measure its strength were also made along with the reported measurements herein. Unfortunately, none of the data taken were acceptable for analysis owing to experimental errors; such as, Faraday cups left in during the run, and incorrect beam energies, to mention a few. As of the final week of June 2003, DRAGON accepted ^{21}Na beam one final time in an effort to make a measurement of the strength of this resonance. Yield, in both coincidence and singles mode, was conclusively observed. Analysis of these data will proceed and will be subsequently reported in a journal article.

In the meantime, the quest for the 1.28 MeV γ-line will continue. For now, with feet planted firmly on this "mote of dust" [74], we shall continue to look skyward for our inspiration, our wonder and for an obscure signal of light at 1.28 MeV that, should it arrive, will help us to understand in some incrementally small way an answer to that timeless of all questions: "From whence did we come?"

Bibliography

[1] STScI. Space Telescope Science Institute, http://www.stsci.edu/.

[2] Edwin Hubble. *Proc. Nat. Acad. Sci. USA*, **15**:168, (1929).

[3] Robert P. Kirshner. *Science*, **300**:1914, (2003).

[4] David Branch. *Ann. Rev. Astron. Astrophys.*, **36**:17, (1998).

[5] B. Leibundgut and G. A. Tammann. *Astron. & Astrophys.*, **230**:81, (1990).

[6] S. Perlmutter et al. *Astrophys. J.*, **517**:565, (1999).

[7] M. Sullivan et al. *Mon. Not. R. Astron. Soc.*, **340**:1057, (2003).

[8] C. Bennet et al., (2003), http://xxx.lanl.gov/abs/astro-ph/0302208. Submitted to Astrophys. J., e-print available.

[9] D. N. Spergel et al., (2003), http://xxx.lanl.gov/abs/astro-ph/0302208. e-print available.

[10] Jordi Miralda-Escudé. *Science*, **300**:1904, (2003).

[11] Robert Irion. *Science*, **300**:1894, (2003).

[12] Hans C. Ohanian and Remo Ruffini. *Gravitation and Spacetime*. W. W. Norton and Company, (1994).

[13] Richard N. Boyd. *Nucl. Phys. A*, **693**:249, (2001).

[14] Kenneth M. Nollett and Scott Burles. *Phys. Rev. D*, **61**:123505, (2000).

[15] Scott Burles et al. *Phys. Rev. Lett.*, **82**:4176, (1999).

[16] A. E. Champagne and M. Wiescher. *Annu. Rev. Nucl. Part. Sci.*, **42**:39, (1992).

[17] Bradley W. Carroll and Dale A. Ostlie. *An Introduction to Modern Astrophysics*. W. W. Norton and Company, (1994).

[18] H. A. Bethe and C. L. Critchfield. *Phys. Rev.*, **54**:248, (1938).

[19] Claus E. Rolfs and William S. Rodney. *Cauldrons in the Cosmos*. University of Chicago Press, (1988).

[20] David Arnett. *Supernovae and Nucleosynthesis*. Princeton University Press, (1996).

[21] Donald C. Clayton. *Principles of Stellar Evolution and Nucleosynthesis*. The University of Chicago Press, (1983).

[22] H. Reeves and E. E. Salpeter. *Phys. Rev.*, **116**:1505, (1959).

[23] Mark A. Garlick, http://www.space-art.co.uk. Image copyright and courtesy Mark A. Garlick. All rights reserved.

[24] S. Ami Glasner and E. Livne. *Astrophys. J.*, **475**:754, (1997).

[25] Robert D. Gehrz et al. *PASP*, **110**:3, (1998).

[26] T. L. Hayward et al. *Astrophys. J.*, **401**:L101, (1992).

[27] Mario Livio and James W. Truran. *Astrophys. J.*, **425**:797, (1994).

[28] Jerry B. Marion and William A. Fowler. *Astrophys. J.*, **125**:221, (1957).

[29] J. José, A. Coc, and M. Hernanz. *Astrophys. J.*, **520**:347, (1999).

[30] M. Wiescher et al. *Nucl. Phys. A*, **484**:90, (1998).

[31] M. Wiescher, H. Schatz, and A. E. Champagne. *Philos. Trans. Roy. Soc. London*, **356**:2105, (1998).

[32] Christian Iliadis, Art Champagne, Jordi José, Sumner Starrfield, and Paul Tupper. *Astrophys. J. Suppl. Ser.*, **142**:105, (2002).

[33] A. F. Iyudin et al. *Astron. & Astrophys.*, **300**:422, (1995).

[34] Sachiko Amari et al. *Astrophys. J.*, **551**:1065, (2001).

[35] David J. Griffiths. *Introduction to Quantum Mechanics*. Prentice Hall, (1995).

[36] John M. Blatt and Victor F. Weisskopf. *Theoretical Nuclear Physics*. Dover Publications, (1979).

[37] C. Caso et al. *Eur. J. Phys. C*, **C3**:1, (1998).

[38] W. A. Fowler, C. C. Lauritsen, and T. Lauritsen. *Rev. Mod. Phys.*, **20**:236, (1948).

[39] Emilio Segrè. *Nuclei and Particles*. W. A. Benjamin, Inc., (1964).

[40] H. E. Gove. Resonance Reactions, Experimental. In P. M. Endt and M. Demeur, editors, *Nuclear Reactions*, volume 1, chapter VI, page 259. North Holland Publishing Company, (1959).

[41] N. Bateman et al. *Phys. Rev. C*, **63**:035803, (2001).

[42] S. Michimasa et al. *Eur. Phys. J. A*, **14**:275, (2002).

[43] A. A. Chen et al. *Phys. Rev. C*, **63**:065807, (2001).

[44] G. Audi and A. H. Wapstra. *Nucl. Phys. A*, **565**:66, (1993).

[45] K. Oxorn et al. *Nucl. Inst. & Meth. in Phys. Res. B*, **26**:143, (1987).

[46] Marik Dombsky. Private communication.

[47] John W. Staples. AIP Conference Proceedings No. 249. In *The Physics of Particle Accelerators*, page 1485, Upton, NY, (1992).

[48] R. E. Laxdal. ISAC at TRIUMF: Status of the Post-Accelerator. In *International Workshop on the Production of Radioactive Ion Beams (PRORIB2001)*, Puri, India, (2001). http://www.triumf.ca/download/lax/prorib2000/ prorib2001_paper. Also, private communication.

[49] D. A. Hutcheon et al. *Nucl. Inst. & Meth. in Phys. Res. A*, **498**:190, (2003).

[50] Dario G. Gigliotti, Joel Rogers, and Ahmed H. Hussein. *Nucl. Inst. & Meth. in Phys. Res. B*, **204**:671, (2003).

[51] Ahmed Hussein. Detectors Lecture Notes. SFU Graduate course Physics 881, (2001).

[52] Sabine Engel. *Awakening of the DRAGON: Commissioning of the DRAGON Recoil Separator Facility & First Studies on the $^{21}Na(p,\gamma)^{22}Mg$ Reaction.* PhD thesis, Ruhr-Universität Bochum, Germany, (2003), http://www.triumf.ca/ dragon/docs/sabine_thesis.pdf.

[53] R. Keitel et al. Design and Commissioning of the ISAC Control System at TRIUMF. In *International Conference on Accelerator and Large Experimental Physics Controls Systems*, Trieste, (1999). http://isacwserv.triumf.ca/isac/pubdoc/ icalepcs99_isac.pdf.

[54] Wenjie Liu. *Charge State Studies of Heavy Ions Passing Through Gas.* Master's thesis, Simon Fraser University, Burnaby, B.C., Canada, (2001), http://www.triumf. ca/dragon/docs/wenjiethesis.pdf.

[55] W. Liu et al. *Nucl. Inst. & Meth. in Phys. Res. A*, **496**:198, (2003).

[56] Dario Gigliotti. *Calibration and Simulation of a Gamma Array for DRAGON at ISAC.* Master's thesis, University of Northern British Columbia, Prince George, B.C., Canada, (2003). To be submitted.

[57] C. E. Rolfs et al. *Nucl. Phys. A*, **191**:209, (1972).

[58] Application Software Group, Computing and Networks Division, CERN Geneva, Switzerland. *PAW: Physics Analysis Workstation*, (1993).

[59] P. Endt. *Nucl. Phys. A*, **521**:1, (1990).

[60] Christopher Lars Henrik Wrede. *A Double Sided Silicon Strip Detector as an End Detector for the DRAGON Recoil Mass Separator.* Master's thesis, Simon Fraser University, Burnaby, B.C., Canada, (2003), http://www.triumf.ca/dragon/docs/Wredethesis.pdf.

[61] D. A. Hutcheon. ISAC Beam Energy Measurement Using DRAGON MD1. Internal DRAGON report, available on request, December (2002).

[62] H. Grawe et al. *Nucl. Phys. A*, **237**:18, (1975).

[63] G. Audi and A. H. Wapstra. *Nucl. Phys. A*, **595**:409, (1995).

[64] R. A. Paddock. *Phys. Rev. C*, **5**:485, (1972).

[65] B. Davids et al. *Proton-Decaying States in ^{22}Mg and the Nucleosynthesis of ^{22}Mg in Novae*, (2003). Private communication and submitted to Phys. Rev. C.

[66] J. A. Caggiano et al. *Phys. Rev. C*, **66**:15804, (2002).

[67] G. P. A. Berg et al. *Nucl. Phys. A*, **718**:608c, (2003).

[68] J. C. Hardy et al. *Phys. Rev. Lett.*, **91**:082501, (2003).

[69] J. C. Hardy et al. *Phys. Rev. C*, **9**:252, (1974).

[70] J. A. Caggiano. Private communication. Analysis still proceeding.

[71] S. Bishop et al. *Phys. Rev. Lett.*, **90**:162501, (2003).

[72] Jordi Gómez-Gomar, Margarita Hernanz, Jordi José, and Jordi Isern. *Mon. Not. R. Astron. Soc.*, **296**:913, (1998).

[73] G. Vedrenne. *Astro. Lett. and Communications*, **39**:325, (1999).

[74] Carl Sagan. *Pale Blue Dot: A Vision of the Human Future in Space.* Random House, (1994).

[75] Phillip R. Bevington and D. Keith Robinson. *Data Reduction and Error Analysis for the Physical Sciences*. McGraw-Hill, (1992).

[76] W. T. Eadie, D. Drijard, F. E. James, M. Roos, and B. Sadoulet. *Statistical Methods in Experimental Physics*. North Holland Publishing Company, (1972).

[77] Louis Lyons. *Statistics for Nuclear and Particle Physicists*. Cambridge University Press, (1992).

[78] George Arfken. *Mathematical Methods for Physicists*. Academic Press, Inc., (1985).

[79] CERNLIB: Short Writeups. CERN, Geneva, Switzerland, (1996).

Appendix A

Statistics and Errors

The DRAGON mass separator can be modeled in terms of a sequence of selection filters. Once a fusion recoil has been formed, prompt γ emission takes place. The detection of that γ-ray by the γ-array is a binomial selection process. Similarly, the selection of said recoil by MD1 and then by the DSSSD are both binomial selection processes. It is the purpose in what follows to derive the statistical likelihood function of the number of observed recoils in a given experimental run, from which a maximum likelihood estimate of the fusion yield can be determined. The notation to be used for expressing a probability distribution function (pdf) will be of the form, $P(a|b)$, to be read as, "the probability of a subject to the parameter, or group of parameters, b".

A.1   The Selection Probability Distribution Functions

The true number of fusion recoil events is Poisson distributed with respect to beam on target (this contrasts with the more familiar example of, say, radioactive decays being Poisson distributed with respect to time). More precisely, if Y is the mean true fusion reaction rate, in units of "recoils per 10^{12} incident beam particles", and n is the true number of fusion events that occur during the course of a run, then the probability of n events occurring, $P(n|f,Y)$, is given by the Poisson distribution as,

$$P(n|f,Y) = \frac{(fY)^n}{n!} \exp(-fY) , \tag{A.1}$$

where f is a constant to ensure the mean is normalized appropriately to the number of incident beam particles on target; that is, if we acquire $f \times 10^{12}$ beam particles on target, then our expected mean yield for this run will just be fY.

Ultimately, the goal of this analysis to obtain the best estimate of Y. We also, of course, can never directly observe the value of n, owing to:

- the γ-array efficiency $< 100\%$

- charge state distribution selection

- particle transport efficiency $< 100\%$

- DSSSD efficiency $< 100\%$

(if we could directly observe n, Y would be immediately determined, given beam on target, and our lives would be so much simpler).

Prompt γ emission follows the production of a fusion recoil. When n true fusion events take place, the γ-array is presented with n emission gammas. Suppose the γ-array has an overall detection efficiency of ε. We then ask: *"What is the probability $P(g|n,\varepsilon)$ that, of n gammas presented, the γ-array detects g $(g \leq n)$ of them?"* The answer to this question is provided by the Binomial probability distribution [75][1]

$$P(g|n,\varepsilon) = \frac{n!}{g!(n-g)!}\varepsilon^g(1-\varepsilon)^{n-g} . \tag{A.2}$$

Of g gammas detected by the γ-array, g fusion recoils make their way to the downstream exit of the target to MD1. Only those recoils of the selected charge state will be "accepted" by the recoil separator; the rest being rejected by MD1. If we know the probability, η, for our selected charge state, then we can ask the following: *"Of g recoils presented to MD1, what is the probability, $P(m|g,\eta)$, that m $(m \leq g)$ recoils are accepted by MD1?"* Again, the answer is the Binomial distribution,

$$P(m|g,\eta) = \frac{g!}{m!(g-m)!}\eta^m(1-\eta)^{g-m} . \tag{A.3}$$

---

[1]In the event where γ-rays of different energies may be emitted, i.e., a cascade decay, then ε is just the weighted average detection efficiency. That is, $\varepsilon = \sum_i \beta_i\varepsilon_i$, with β_i the decay branching for γ_i and ε_i the efficiency of detection for γ_i.

These recoils are subject to the particle transport (optics) of DRAGON, with efficiency θ. That a particle arrives, or not, at the location of the DRAGON final focus is determined again by a Binomial distribution. Of m recoils exiting from MD1, the probability that $t \leq m$ of them arrive at the final focus is just,

$$P(t|m,\theta) = \frac{m!}{t!(m-t)!}\theta^t(1-\theta)^{m-t} \; . \tag{A.4}$$

These recoil particles finally arrive at the DSSSD which has a detection efficiency of δ. With this we can ask: *"Of t transported recoils, what is the probability, $P(r|t,\delta)$, that r ($r \leq t$) recoils are detected by the DSSSD?"* The answer, of course, is again provided by the Binomial distribution,

$$P(r|t,\delta) = \frac{t!}{r!(t-r)!}\delta^r(1-\delta)^{t-r} \; . \tag{A.5}$$

With these selection probability distribution functions, a likelihood function can be constructed from which the probability of observing r coincident fusion recoils subject to the mean yield, Y, can be derived.

A.1.1 Deriving P(r|Y)

Before proceeding further, it is necessary to derive a general result: the folding of a Poisson pdf, $P(k|f,Y)$, with a Binomial pdf, $P(j|k,\xi)$, results in a pdf that is Poisson of argument $f\xi Y$; namely,

$$
\begin{aligned}
\sum_{k=j}^{\infty} P(k|f,Y)P(j|k,\xi) &= \sum_{k=j}^{\infty}\left(\frac{(fY)^k}{k!}e^{-fY}\right)\left(\frac{k!\,\xi^j(1-\xi)^{k-j}}{j!(k-j)!}\right) \tag{A.6}\\
\overset{(l=k-j)}{=} \; &\frac{(f\xi Y)^j}{j!}e^{-fY}\sum_{l=0}^{\infty}\frac{(fY)^l}{l!}(1-\xi)^l\\
&= \frac{(f\xi Y)^j}{j!}e^{-fY}e^{fY(1-\xi)}\\
&= \frac{(f\xi Y)^j}{j!}e^{-f\xi Y} \; .
\end{aligned}
$$

From this result, it naturally follows that if we now fold another Binomial pdf, $P(n|j,\chi)$, with that of equation A.6 we will be left with another Poisson pdf of argument $f\xi\chi Y$, and so on. This result is central in what follows.

Because we can never directly observe the true number of fusion events, n, the probability of observing g γ-events, given a mean fusion reaction rate Y, is given by the folding of equation A.1 with equation A.2 summed over all possible numbers of fusion events. By the result of equation A.6, we have,

$$P(g|Y) = \frac{(\varepsilon f Y)^g}{g!} \, e^{-\varepsilon f Y} \, . \tag{A.7}$$

The γ-events that we observe in this experiment are those which are in coincidence with fusion recoils detected by the DSSSD. We therefore do not directly observe g in the coincidence data. For there to be any chance of a recoil detection the fusion recoil must pass the MD1 charge state selection. Thus, the probability of m fusion recoils being successfully selected by MD1, given that the mean fusion yield rate is Y, is the folding of equation A.7 with equation A.3, summed over all unknown gamma events; namely,

$$P(m|Y) = \frac{(\varepsilon \eta f Y)^m}{m!} \, e^{-\varepsilon \eta f Y} \, ; \tag{A.8}$$

having once again invoked the result of equation A.6.

These m recoils are transported by the DRAGON optics with efficiency, $\theta < 1$. As with the above, m is not an observable quantity. The probability, $P(t|Y)$, that $t < m$ fusion recoils make it to the DRAGON final focus is the folding of equation A.4 with equation A.8 summed over the unobserved m: the result being,

$$P(t|Y) = \frac{(\varepsilon \eta \theta f Y)^t}{t!} \, e^{-\varepsilon \eta \theta f Y} \, ; \tag{A.9}$$

These t recoils are detected by the DSSSD with efficiency, $\delta < 1$, and thus, t is not a complete observable. As such, the probability of detection in the DSSSD of r recoils, given that the mean fusion yield rate is Y, is once again obtained by folding equation A.9 with the binomial probability of equation A.5 over all possible t; whence,

$$P(r|Y) = \frac{(\varepsilon \eta \theta \delta f Y)^r}{r!} \, e^{-\varepsilon \eta \theta \delta f Y} \, . \tag{A.10}$$

We see that the probability distribution for recoil detection in the DRAGON mass separator is Poisson in nature and is parametrically dependent on the combined efficiencies of the separator; namely, the efficiencies of detection for: γ-rays, particle transport, recoil ion detection; and on the charge state selection.

A.2 The Likelihood Function: What is It?

Consider the following: We have a physical quantity we want to measure; Y in the case of this experiment. Prior to making any measurement of Y, our knowledge of what the value of Y is is one of complete ignorance[2]. A distribution that would represent this state of knowledge (or lack thereof) would be something like that in frame a) of figure A.1; all we can say about Y is that it is some real number greater than zero.

We make our first measurement of Y, call it Y_1, and form a more refined distribution function for the true value of Y as a result. After one measurement on Y our state of knowledge has improved from complete ignorance to something like that shown in the distribution represented by the solid curve of frame b) of figure A.1; a broad distribution whose maximum, Y^*, is what we now consider our current best estimate of the true value of Y.

Now we make a second measurement of Y, call it Y_2, and we obtain another distribution for the true value of Y, similar to that for Y_1, but slightly different in that $Y_1 \neq Y_2$ in general. The distribution for Y_2 is shown in frame b) of figure A.1 by the dash-dot line. The joint probability distribution of these two measurements will be the product of these two distributions. We can imagine that if we take the product of the two curves in frame b) of figure A.1 we will obtain a distribution like that shown in frame c) of figure A.1. As we acquire more measurements of Y, forming the set $S = \{Y_1, Y_2, \ldots, Y_N\}$, we continue to combine the individual probability distributions for each Y_i by taking their products. This will lead to a joint probability distribution function that will be sharply peaked and it is the value of Y at the maximum of this distribution that we take as our best estimator of the true value of Y.

More formally, if $P_i(r_i|Y)$ is the probability distribution of the i'th measurement of r, then the likelihood $\mathcal{L}$ function of Y will be [75–77]:

$$\mathcal{L}(Y) = \prod_{i=1}^{N} P_i(r_i|Y) , \qquad (A.11)$$

with proviso,

$$\sum_{r_i=0}^{\infty} P_i(r_i|Y) = 1$$

---

[2]For the purposes of this discussion, I am intentionally neglecting "knowledge" proffered up by theoretical estimates.

P(r|Y)

a)

R

Y

1/R

P(r|Y)

b)

$P_1(r|Y)$

$P_2(r|Y)$
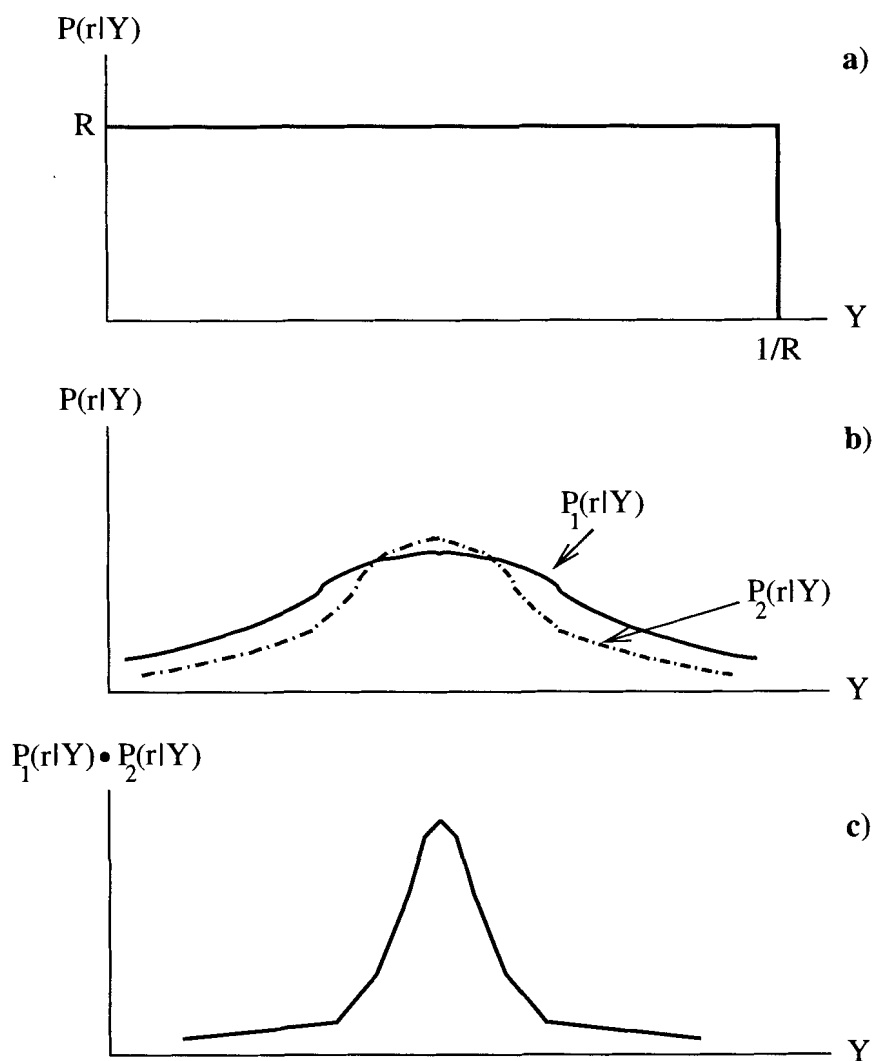
Y

$P_1(r|Y) \cdot P_2(r|Y)$

c)

Y

Figure A.1: Sequence of improving knowledge: Frame a) shows a representation of complete ignorance on the value of Y; all values of Y are equally probable. Frame b) shows two separate measurements of Y that are, individually, broad. Frame c) shows what the joint probability distribution formed by the product $P_1(r_1|Y_1) \cdot P_2(r_2|Y_2)$.

that is, probability distribution associated with each separate measurement of r_i is normalized with respect to the *measured* parameter r_i; a condition clearly satisfied with P_i a Poisson distribution.

We want to maximize equation A.11. An equivalent problem to maximizing equation A.11 is to instead maximize[3]:

$$\ln(\mathcal{L}) = \sum_{i=1}^{N} \ln[P_i(r_i|Y)] .$$
(A.12)

Substituting the expression for $P_i(r_i|Y)$ from equation A.10 into equation A.12 and taking the partial derivative with respect to Y results in,

$$\frac{\partial}{\partial Y} \sum_i [r_i \ln(\varepsilon_i \eta_i \theta_i \delta_i f_i Y) - \varepsilon_i \eta_i \theta_i \delta_i f_i Y - \ln(r_i!)] = 0$$
(A.13)

which yields the analytic solution,

$$Y^* = \frac{\sum_i r_i}{\sum_i \varepsilon_i \eta_i \theta_i \delta_i f_i} .$$
(A.14)

Note that $\mathcal{L}$ need not be normalized to unity for this method to work, as the inclusion of a normalization constant would merely add a constant term to the left hand side of equation A.13 which would vanish on differentiating with respect to Y.

A few useful points about the asymptotic (large N) behaviour of likelihood estimators:

1. They are unbiased.

2. They are minimum variance.

3. Their likelihood functions tend to normal distributions; that is,

$$\mathcal{L} \sim \exp\left\{ -\frac{1}{2} \frac{(Y - Y^*)^2}{\sigma^2} \right\} .$$

Because of point 3, the 1σ variance of the likelihood parameter can be estimated by either:

- Finding the values of Y where $\ln \mathcal{L}$ changes by $-1/2$ from its maximum value, $\ln \mathcal{L}_{\max} - 1/2$, or

---

[3]Recall, $\frac{d}{dx}[\ln f(ax)] = a\frac{f'(ax)}{f(ax)} = 0$ implies the derivative is equal to zero – which is just the condition for maximization.

- Taking the square root of the reciprocal of the negative second partial derivative of the ln-likelihood function, evaluated at Y^*:

$$\sigma = \left(-\frac{\partial^2 \ln(\mathcal{L})}{\partial Y^2} \right)^{-1/2} \Bigg|_{Y^*} .$$

Thus, for large N, taking the second partial derivative of equation A.11 with respect to Y and using the result of equation A.14 we arrive at, for σ:

$$\sigma = \frac{Y}{\sqrt{\sum_i r_i}} . \tag{A.15}$$

A.3 Confidence Intervals

For measurements with small recoil counts, equation A.15 will not be correct as the Poisson distribution is asymmetric for small counts. Nonetheless, the Maximum Likelihood method readily provides for determining the 1σ confidence interval on the likelihood estimate of yield, Y^*. The 1σ confidence interval is defined by the limits on the values of Y above and below Y^*, such that, the area under the curve of the likelihood function between these limits is 68.3% of the total area under the entire liklihood function. Mathematically, the limits of Y which satisfy this requirement are found by solving the integral equation,

$$\sigma = \int_{Y^*-a}^{Y^*+b} \mathcal{L}(Y)\,dY , \tag{A.16}$$

for a and b, subject to the proviso,

$$\mathcal{L}(Y^* - a) = \mathcal{L}(Y^* + b) , \tag{A.17}$$

and the normalization condition:

$$\int_0^\infty \mathcal{L}(Y)\,dY = 1 .$$

Substitution of equation A.10 into equation A.11, after performing some algebraic manipulation, results in an explicit form for the likelihood function:

$$\mathcal{L} = \frac{\Pi_i^N (\alpha_i Y)^{r_i}}{\Pi_i^N (r_i!)} \exp\left(Y \sum_i^N \alpha_i \right) = \frac{\Pi_i^N (\alpha_i)^{r_i}}{\Pi_i^N (r_i!)} Y^{\sum_i^N r_i} \exp\left(Y \sum_i^N \alpha_i \right) , \tag{A.18}$$

with $\alpha_i = \varepsilon_i \eta_i \theta_i \delta_i f_i$. The normalization condition requires the result of the integration:

$$\frac{\Pi_i^N (\alpha_i)^{r_i}}{\Pi_i^N (r_i!)} \int_0^\infty Y^{\Sigma_i^N r_i} \exp \left(Y \sum_i^N \alpha_i \right) dY \,. \qquad (A.19)$$

The above integral can be made more transparent with the substitutions: $\chi = \sum_i \alpha_i$, $\zeta = \sum_i r_i$ and $t = Y\chi$ to give:

$$\frac{1}{\chi^{\zeta+1}} \int_0^\infty t^\zeta \exp(-t) dt = \frac{1}{\chi^{\zeta+1}} \Gamma(\zeta+1) = \frac{\zeta!}{\chi^{\zeta+1}} \,, \qquad (A.20)$$

with $\Gamma(x)$ the Gamma Function [78]. Thus, from these, it follows that the normalized likelihood function is:

$$\mathcal{L} = \frac{\chi^{\zeta+1}}{\zeta!} Y^\zeta \exp(-\chi Y) \,. \qquad (A.21)$$

A.3.1 Explicit Confidence Interval Formula

The integral of equation A.16 can be written as,

$$\sigma = \int_{Y^*-a}^{Y^*+b} \mathcal{L}(Y) dY = \int_0^{Y^*+b} \mathcal{L}(Y) dY - \int_0^{Y^*-a} \mathcal{L}(Y) dY \,. \qquad (A.22)$$

Substituting the result of equation A.21 into equation A.22 and using the change of variables, $t = \chi Y$, results in,

$$\sigma = \frac{1}{\zeta!} \left(\int_0^c t^\zeta \exp(-t) dt - \int_0^d t^\zeta \exp(-t) dt \right) = \gamma(\zeta+1, c) - \gamma(\zeta+1, d) \,, \qquad (A.23)$$

with $c = \chi(Y^* + b)$, $d = \chi(Y^* - a)$ and $\gamma(x, y)$ the Incomplete Gamma function [78] defined by,

$$\gamma(x, y) = \frac{1}{\Gamma(x)} \int_0^y t^{x-1} \exp(-t) dt.$$

The result of equation A.23 is readily convenient for numerical computation as the CERN Fortran subroutine library, CERNLIB [79], contains a subroutine that evaluates the Incomplete Gamma Function from user input. Values of c are looped over. For a particular loop value of c a numerically determined value for d, satisfying equation A.17 is found. With these values of c and d, the right hand side of equation A.23 is evaluated until such time that its value is within some tolerance (10^{-3} difference) of the choice for σ. Using

$c = \chi(Y^* + b)$ and $d = \chi(Y^* - a)$, the values of a and b for the confidence interval limits can then be determined. Figure A.2 shows a plot of equation A.23 for data taken at a beam energy of 214.9 keV/u (lab) with the hatched region showing the resulting 1σ confidence interval obtained in this way.

Finally, in the case when there are no recoil events observed, so that $\zeta = 0$, equation A.21 reduces to a simple exponential function. Integration of equation A.21 under
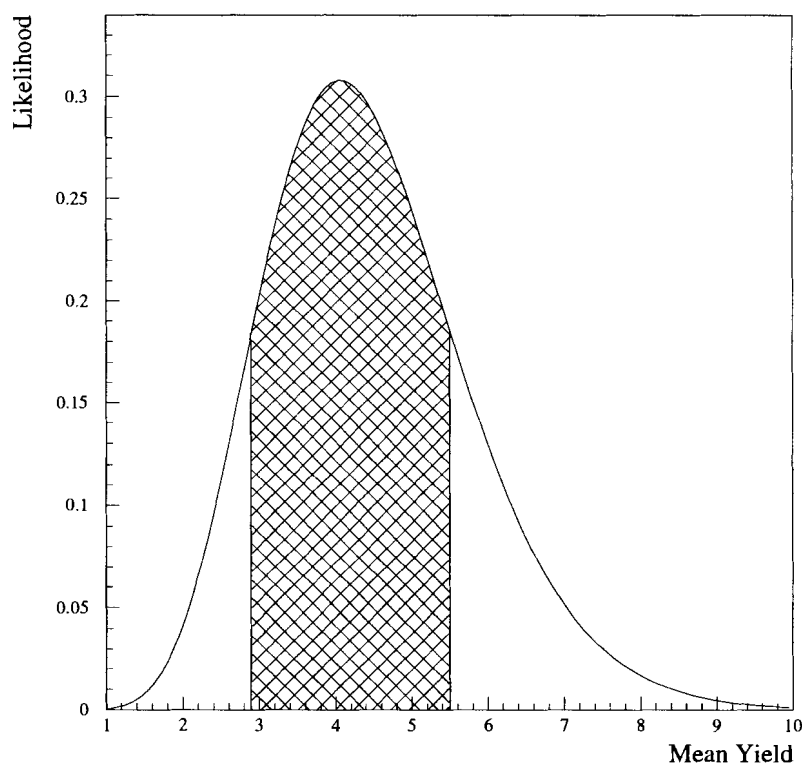

Figure A.2: A plot of the likelihood function for the data taken at a beam energy of 214.9 keV/u. The hatched region shows the 1σ confidence interval where the area under the curve is 68.3% of the total area.

these conditions results in an expression for the upper limit for the yield, Y, given by,

$$Y \leq -\frac{1}{\chi} \ln(1 - \sigma) \,. \qquad \text{(A.24)}$$

Appendix B

Data Summary

Table B.1: Summary of measured elastically scattered protons, for the reaction study at $E_{cm} =$ 212 keV, as determined by the RF background subtraction method and exponential fit method as discussed in § 4.5.1. RF protons = total number of protons obtained from the RF background subtraction method. Fit Protons = total number of protons obtained from the exponential fit method.

$E_{cm} = 212$ keV				
Run #	Energy (keV/u)	RF Protons ($\times 10^5$)	Fit Protons ($\times 10^5$)	Live Time (%)
4882	230.0	3.691(14)	3.595	98.7
4868	225.0	3.333(33)	3.187	96.4
4869	225.0	1.512(21)	1.484	96.5
4872	225.0	4.041(33)	3.901	93.9
4873	220.0	5.006(19)	4.932	98.0
4883	220.0	2.520(12)	2.613	98.9
4884	220.0	1.791(18)	1.743	94.6
4885	220.0	3.443(15)	3.458	99.1
4886	220.0	2.649(13)	2.760	97.2
4887	220.0	1.237(9)	1.244	98.9
4878	215.0	1.414(12)	1.508	98.6
4879	215.0	3.278(17)	3.304	98.5
4880	215.0	2.973(16)	3.153	98.6

...continued from previous page

Run #	Energy (keV/u)	RF Protons ($\times 10^5$)	Fit Protons ($\times 10^5$)	Live Time (%)
6171	214.9	–	0.0351(23)	68.6
6176	214.9	–	1.385(14)	86.9
6178	214.9	–	1.984(16)	93.1
6181	214.9	–	2.241(20)	96.8
6188	214.3	–	0.1837(28)	99.1
6189	214.3	–	0.5994(49)	99.1
6190	214.3	–	0.5291(46)	99.0
6191	214.3	–	1.235(7)	99.0
6184	211.9	–	1.347(7)	98.6
6185	211.9	–	1.329(7)	98.9
6186	211.9	–	0.8757(6)	99.0
6187	213.5	–	1.733(1)	98.6
4881	210.0	5.847(23)	5.830	98.7

Table B.2: Summary of measured elastically scattered protons, for the reaction study at $E_{cm} = 335$ keV, as determined by the RF background subtraction method and exponential fit method as discussed in § 4.5.1.

$E_{cm} = 335$ keV			
Run #	Energy (keV/u)	Fit Protons ($\times 10^4$)	Live Time (%)
6222	360.0	1.305(31)	79.9
6235	360.0	6.239(33)	95.8
6237	360.0	10.037(15)	97.0
6238	360.0	1.943(19)	97.3
6239	360.0	1.492(18)	90.0
6246	360.0	1.242(16)	92.4
6247	360.0	2.896(25)	94.0
6248	360.0	2.072(21)	94.1

Table B.3: Summary of beam normalizations.

Beam Normalization Data						
Run #	Energy (keV/u)	P (torr)	I (pA)	Δt (s)	N_p $(\times 10^3)$	R
4882	230.0	4.61	44.0	800	9.790(219)	1.930(182)
4868	225.0	4.55	64.0	480	7.836(475)	2.120(186)
4869	225.0	4.55	57.0	150	2.160(326)	2.144(358)
4873	220.0	4.56	60.0	3000	51.82(59)	2.022(138)
4883	220.0	4.73	50.0	1500	23.32(38)	1.950(160)
4884	220.0	4.72	54.4	4000	57.48(1.00)	2.181(166)
4885	220.0	4.72	49.0	1500	23.14(38)	1.918(161)
4887	220.0	4.73	48.0	1500	21.67(37)	2.003(172)
4893	220.0	4.70	48.0	600	8.746(438)	1.949(191)
4878	215.0	4.68	58.0	7000	125.0(1)	1.983(139)
4879	215.0	4.67	58.0	600	11.66(33)	1.603(121)
4880	215.0	4.67	60.0	400	6.982(236)	2.131(161)
6181	214.9	4.64	70.0	1920	16.77(48)	2.026(131)
6189	214.3	2.55	34.0	2000	9.371(193)	2.493(299)
6190	214.3	2.56	45.0	2000	12.73(22)	2.437(222)
6187	213.5	4.62	34.0	1700	17.63(30)	2.045(244)
6185	211.9	4.72	40.0	400	4.095(126)	2.537(267)
4181	210.0	4.72	57.0	1920	33.59(53)	2.148(156)
6235	360.0	8.00	26.4	450	2.203(63)	2.078(321)
6238	360.0	7.98	20.0	360	1.146(52)	2.414(496)
6239	360.0	7.89	20.0	630	2.056(83)	2.329(476)

Appendix C

Stable Beam Commissioning Data Summary

Table C.1: Summary of measured resonance strengths from the DRAGON stable beam commissioning study. Refer to Sabine Engle's thesis [52] for the detailed analysis of these results.

Measured Resonance Strengths				
Reaction	E_{cm} (keV)	$\omega\gamma_{lit}$	$\omega\gamma_{meas}$	$\omega\gamma_{meas}/\omega\gamma_{lit}$
^{20}Ne(p,γ)^{21}Na	1112.6	1.13(7) eV	0.92(17) eV	0.81
^{21}Ne(p,γ)^{22}Na	258.6	82.5(12.5) meV	209(35) meV	2.27
^{21}Ne(p,γ)^{22}Na	731.5	3.95(79) eV	3.85(53) eV	0.97
^{24}Mg(p,γ)^{25}Al	214.0	12.7(9) meV	11.7(1.6) meV	0.92
^{24}Mg(p,γ)^{25}Al	402.2	41.6(2.6) meV	56.4(8.7) meV	1.36
^{24}Mg(p,γ)^{25}Al	790.4	532(41) meV	576(39) meV	1.08

Table C.2: Summary of measured resonance energies from the DRAGON stable beam commissioning study. Refer to Sabine Engle's thesis [52] for the detailed analysis of these results.

Measured Resonance Energies			
Reaction	E_{lit} (keV)	E_{meas} (keV)	E_{meas}/E_{lit}
$^{20}Ne(p,\gamma)^{21}Na$	1112.6(6)	1110.9(8)	0.998
$^{21}Ne(p,\gamma)^{22}Na$	731.5(1.6)	732.1(5)	1.001
$^{21}Ne(p,\gamma)^{22}Na$	214.0(8)	214.5(4)	1.002